Integration of Silicon Nanowires with 3D Devices: Fabrication and Modeling

by

Mohammad Nasr Esfahani

A Dissertation Submitted to the
Graduate School of Sciences and Engineering
in Partial Fulfillment of the Requirements for
the Degree of

Doctor of Philosophy

in

Mechanical Engineering



June, 2017

Integration of Silicon Nanowires with 3D Devices: Fabrication and Modeling

Koç University

Graduate School of Sciences and Engineering

This is to certify that I have examined this copy of a doctoral dissertation by

Mohammad Nasr Esfahani

and have found that it is complete and satisfactory in all respects,
and that any and all revisions required by the final
examining committee have been made.

Committee Members:

_____

B. Erdem Alaca, Ph.D. (Advisor)

_____

Murat Sözer, Ph.D.

_____

Şükrü Ekin Kocabaş, Ph.D.

_____

Arda D. Yalçınkaya, Ph.D.

_____

Selim Hanay, Ph.D.

Date: _____

To My Beloved Parents

ABSTRACT

Silicon nanowires as fundamental building blocks in many nanoelectromechanical systems find applications in sensors and electronic devices. Extensive use of silicon nanowires in modern electronic devices faces integration challenges with the high-order architectures such as three-dimensional integrated circuits and microelectromechanical systems. A monolithic integration of silicon nanowires with microstructures can address the shortcoming of available techniques marred by the lack of batch techniques compatible with semiconductor manufacturing. In this study, a monolithic incorporation of silicon nanowires in bulk silicon with an etch depth of 40-μm is demonstrated through a combination of high-resolution lithography and deep etching technology. This technique opens up new possibilities for modern sensors by replacing capacitance-based motional detection by high-sensitivity piezoresistive system via silicon nanowire use. Such monolithic approach to downscaling silicon piezoresistive sensors is presented in this study by spanning an electrostatic comb-drive actuator and a micromechanical amplifier by a single nanowire. Similar contribution of piezoresistive silicon nanowire electromechanical resonators to 3D devices is depicted based on frequency down-mixing approach as well. As this multi-scale integration is accomplished in a batch-compatible fashion, the presented technique carries significant implications for physical and biological miniaturized piezoresistive sensor technologies.

In addition to integration challenges, the full potential of the miniaturized silicon nanowires in the field of physical sensors is yet to be realized. Mechanical modeling is one of the main challenges in design of nanowires with scale dependence of transport properties. Surface stress is considered as the major effect of size dependence in mechanical properties of nanowire. A sound guideline in mechanical modeling can

address the successful engineering design of such unique architecture. In this work, a guideline for selecting the optimum engineering tool for the frequency response modeling of flexural nanowire resonators is introduced through a benchmarking study among analytical and numerical techniques. The limited applicability due to the associated computational cost in available approaches to analyze thermomechanical behavior of nanowires with surface stress contribution are addressed in this study by using a temperature-dependent interatomic potential in the standard Cauchy-Born theory. In this respect a comprehensive study on crystal orientation and geometrical parameters can shed light on the role played by the surface stress in determining silicon nanowire mechanical behavior. This is accomplished by linking the local surface stress at the atomic scale to the overall behavior of the continuum system. Addressing the existing controversy regarding the contribution of surface stress in the mechanical behavior of silicon nanowires, results in this work can provide a guideline for the interpretation of existing and the design of future experimental investigations.

ÖZETÇE

Bir çok nanoelektromekanik sistemin temel yapıtaşlarından birisi olan silisyum nanoteller, algılayıcı ve elektronik cihazlarda kullanım alanı bulmaktadır. Silisyum nanotellerin modern elektronik cihazlarda daha kapsamlı kullanımının önündeki engellerden birisi, üç boyutlu tümleşik devreler ve mikroelektromekanik sistemler gibi yüksek mertebeli mimariler ile birleştirilme meselesidir. Bu kapsamda silisyum nanotellerin mikron boyutlu yapılarla yekpare şekilde tümleştirilmesi, yarı iletken üretimi ilişkili olarak önerilen halihazırdaki tekniklerin seri imalat eksikliğini gidermeyi amaçlamaktadır. Bu çalışmada, yüksek çözünürlüklü litografi ve derin aşındırma teknolojileri yoluyla silisyum nanotellerin 40 μm derinliğine kadar silisyum alttaşı ile yekpare birleştirilebildiği gösterilmiştir. Bu teknik sayesinde sığa değişimine bağlı yer değiştirme algılayıcılarının yerinin silisyum nanotel tabanlı, yüksek çözünürlüklü piezorezistif sistemler tarafından alınması ihtimal dahilindedir. Piezorezistif algılayıcıların boyutlarının bu şekilde küçültülebilmesi, elektrostatik bir eyleyici ile mikromekanik bir yükselticinin arasına tek bir silisyum nanotel köprü kurulması yoluyla gösterilmiştir. Piezoresistif silisyum nanotel tabanlı elektromekanik çınlaçların üç boyutlu cihazlara benzer bir katkısı frekans indirgeme yöntemi ile başarılmıştır. Bahsedilen çok ölçekli tümleştirme yöntemi seri üretime uygun bir şekilde gerçekleştirildiğinden, küçültülülmüş piezorezistif yapı tabanlı fiziksel ve biyolojik algılayıcı teknolojileri için önemli olası sonuçlar taşımaktadır.

Bu tür tümleştime zorluklarına ilaveten silisyum nanotellerin algılayıcılarda kullanımının önündeki bir başka engel ise tasarımın dayandırılacağı mekanik modellerin ölçeğe dayalı bir şekilde oluşturulmasındaki zorluklardır. Yüzey gerilmesi, nanotelin ölçeğe bağlı mekanik özellikleri için ana bir etki olarak değerlendirilmektedir. Bu çalışmada eğilmeye dayalı çalışan nanotel çınlaçlarda frekans davranışının

modellenmesi amacıyla mevcut analitik ve sayısal yöntemlerle karşılaştırmalı bir tetkik yapılmıştır. Yüzey gerilmesi katkısını içeren termomekanik nanotel davranışının analizinde halihazırdaki tekniklerin hesaplama maliyetleri sebebiyle kısıtlı kullanımları Standart Cauchy-Born teorisinde sıcaklığa bağlı atomlar arası potansiyellerin kullanımı ile giderilmiştir. Bu kapsamda kristal yönelimi ve geometriye dayalı değişkenlerin kapsamlı incelenmesi, yüzey gerilmesinin silisyum nanotel mekanik davranışı konusunda oynadığı role ışık tutabilir. Bu tür bir inceleme, atomik seviyedeki yerel yüzey gerilmelerinin sürekli ortamın genel davranış ile bağdaştırılması sayesinde mümkün olmuştur. Geliştirilen bu yöntem, literatürde tartışma yaratan mevcut deneysel gözlemlerin sağlıklı yorumlanması ile gelecekteki deneysel çalışmaların tasarımı konularında yol gösterici olacaktır.

ACKNOWLEDGMENTS

First and foremost, I would like to express my deepest gratitude to my advisor, Professor Erdem Alaca, for providing valuable guidance, strong support and excellent resources throughout my Ph.D. program. I was honored to be part of his research team at Mechanical Characterization Laboratory at Koç University. He has been a great hardworking mentor and aspiration for me in becoming a successful research scholar. Without his strong support and endless patience, I would have never been able to complete this research work; for all of them, I am forever grateful.

I wish to acknowledge Professor Yusuf Leblebici for the valuable support in experimental study in nanofabrication during my stay at his research group, Microelectronic Systems Laboratory, at École Polytechnique Fédérale de Lausanne. I also would like to thank Professor Jesper H. Hattel for helping me gaining insight into numerical modeling during my stay at his research group, Process Modeling Group, at Technical University of Denmark. I want to thank Professor Selim Hanay for helping in resonance frequency measurements.

I would also like to thank my dissertation committee members Professor Arda D. Yalçınkaya, Professor Murat Sözer and Professor Şükrü Ekin Kocabaş for their valuable time and support in successfully completing this dissertation. I would like to acknowledge the support of my colleagues at Mechanical Characterization Lab whose timely cooperation has been instrumental to the progress of this work during the past 4 years.

My special thanks go to Dr. Masoud Jabbari for his great support over past decade friendship.

Last but not the least, I thank my lovely parents for providing strong emotional support from thousands of miles away.

This study is supported by TÜBİTAK under Grant No. 112E058 and Swiss Government Excellence Grant.

TABLE OF CONTENTS

List of Tables **xiv**

List of Figures **xv**

Chapter 1: Introduction **1**

Chapter 2: 3D Scale-up Device Integration of Silicon Nanowires **3**

2.1 Overview 3

2.2 Introduction 3

2.3 Fabrication Approach 6

2.4 Results and Discussion 8

2.5 Conclusion 16

Chapter 3: Downscaling of Silicon Piezoresistive Sensors **18**

3.1 Overview 18

3.2 Introduction 19

3.3 Device Design and Analysis 21

3.4 Fabrication Process 25

3.5 Results 28

3.6 Conclusion 34

Chapter 4: Electromechanical Resonator Applications **36**

4.1 Overview 36

4.2 Introduction 36

4.3 Device Architecture and Measurement 37

4.4 Conclusion 41

Chapter 5: Frequency Response Modeling of Nanowire Resonators 42

5.1 Overview 42

5.2 Introduction 43

5.3 Formulation 47

5.3.1 Analytical Models 47

5.3.2 Numerical Models 48

5.4 Case Studies for Nanowire Resonators 50

5.5 Results and Discussion 52

5.6 Conclusion 63

Chapter 6: Thermo-coupled Surface Cauchy-Born 65

6.1 Overview 65

6.2 Introduction 65

6.3 Methodology 69

6.4 Numerical Model 73

6.5 Results and Discussion 75

6.6 Conclusion 79

Chapter 7: Silicon Nanowire Mechanical Modeling: Size and Orientation Dependence 82

7.1 Overview 82

7.2 Introduction 83

7.3 Theory 87

7.3.1 Atomic-level description 87

7.3.2 SCB formulation 89

7.3.3 Surface energy in {100} surface 91

7.3.4 Surface energy in {110} surface 93

7.4 Surface stress benchmark 94
7.5 Numerical study 98
7.6 Results and Discussion 99
7.6.1 Crystal Orientation *I* 99
7.6.2 Crystal Orientaion *II* 101
7.6.3 Surface Stress Effect on the Operation of an Electromechanical Switch 104
7.7 Conclusion 108

Chapter 8: Remarks **111**

Bibliography **114**

Appendix **137**

LIST OF TABLES

3.1 Device geometry and following lumped parameters. An actuator is designed for NWs with two different lengths. 25

5.1 Summary of geometries considered (All dimensions are $L \times b \times a$ in (nm)). 52

7.1 Constant parameters for Tersoff-T3 potential [Tersoff, 1989]. 89

7.2 Summary of NW dimensions and crystal orientations. 100

LIST OF FIGURES

2.1 Process flow for the fabrication of suspended Si NWs, (a) e-beam lithography, (b) reactive ion etching (shallow etch), (c) low-temperature oxide coating, (d) directional oxide etching, (e) deep reactive ion etching, (f) removal of all protective layers. The sketch is not drawn to scale. Si NW has a CD of 80 nm, whereas the maximum trench depth achieved is 40 μm. 7

2.2 (a) An array of suspended Si NWs with a 40-μm etch depth in bulk Si. Numbers 80 and 120 refer to the width of the NW, while numbers from 50 to 100 printed parallel to NWs represent ARs. (b) A close-up of an array of NWs with ARs of 50 and 100. (c) A Si NW with a width of 80 nm and a length of 5 μm spanning a 40-μm-deep trench. (d) A close-up of the Si NW of panel (c) near its support. 9

2.3 Side views of Si NWs of a width of 80 nm between two fixed supports spanning a 40-μm-deep trench. (a) 5 μm and (b) 8 μm Si NW length with close-ups. 10

2.4 Evolution of the Si NW profile as a function of the etch depth. (a) Si NW profile after shallow etch (figure 1.b). Si NW profile after DRIE (figure 1.e) with an etch depth of (b) 15 μm and (c) 30 μm with the associated high-resolution TEM image and diffraction pattern. The standard deviation of the TEM length scale measurement is 3%. All scale bars indicate 20 nm. (d) A list of cross-sectional feature dimensions. 12

2.5 Si NW-electrode fabrication on SOI with TAR = d/w. (a) e-beam lithography, (b) metallization by lift-off, (c) reactive ion etching (shallow etch), (d) low-temperature oxide coating, (e) directional oxide etching, (f) electrode protection, (g) deep reactive ion etching, (h) removal of all protective layers. The sketch is not drawn to scale. Si NW has a CD of 100 nm, whereas the SOI device layer thickness is 10 μm. Si NW in the scanning electron micrograph with false coloring has a 5-μm length, 100-nm width and 180-nm±20-nm thickness integrated with two electrodes with TAR = 50 (blue: suspended Si NW and anchors, green: electrodes and red: metal pads). 14

2.6 Current-voltage characteristics of the Si NWs with 100-nm width and 180-nm±20-nm thickness integrated with two electrodes with TAR = 50, and w = 200 nm. 15

3.1 (a) Schematic of the device consists of actuator, Si NW and mechanical amplifier, (b) lumped mechanical model with electrical connections. The axis of loading, x, is aligned along $< 100 >$ crystal orientation. . 23

3.2 Si NW integration with MEMS on SOI. (a) e-beam lithography, (b) metal deposition by lift-off, (c) shallow Si etch, (d) low-temperature oxide coating, (e) directional oxide etching, (f) MEMS patterning, (g) deep reactive ion etching of Si, (h) resist removal and (i) release in HF vapor. Sections A-A' and B-B' depict Si NW protrusion after shallow etch and Si NW cross-section after deep etch, respectively. The sketches are not drawn to scale. Si NW has a CD of 100 nm, whereas the SOI device layer thickness is 10 μm. 26

3.3 Fabricated device with false coloring, (a) the device consists of a comb-drive actuator, a mechanical amplifier and a Si NW spanning aforementioned components, (b) a close-up of the suspended Si NW between the actuator and the amplifier surrounded by two electrodes with a 400-nm gap, (c) a close-up of the comb-drive actuator, (d) cross section of comb-drive actuator highlighting anchored and released regions. Red and blue colors represent metal and BOX, respectively. 29

3.4 The evolution I_{NW} and Si NW resistance as a function of V_{MEMS} for Si NW lengths of (a) 5 μm and (b) 8 μm. 30

3.5 Uniaxial strain applied on Si NWs as a function of V_{MEMS}. 31

3.6 Relative change of Si NW resistance as a function of the applied uniaxial strain. 32

3.7 Quasistatic cyclic measurement of the current through the 8-μm-long Si NW at a constant V_{NW} = 5 mV subjected to a stepwise-varying actuator voltage. 33

4.1 (a) Si NW resonator with a 5-μm length, 100-nm width and 200-nm thickness surrounded by two electrostatic gates with a gap of 400-nm (false color with yellow representing metal pads), (b) Schematic diagram of the measurement circuit. LIA: lock-in amplifier, BT: bias tee, LPF: low pass filter, (c) First-mode frequency response of the device at drive NW voltage V_{NW}^{AC}=0.4 V and driving bias voltage V_{gate}^{AC}=6 V at a DC level of V_{gate}^{DC}=6 V at the atmospheric pressure and a pressure of 4×10^{-3} bar , (d) Second-mode frequency response of the device at drive NW voltage V_{NW}^{AC}=0.4 V and driving bias voltage V_{gate}^{AC}=10 V at a DC level of V_{gate}^{DC}=15 V at atmospheric and a pressure of 4×10^{-3} bar(All AC voltages are peak-to-peak magnitude). 39

4.2 (a) First-mode, and (b) Second-mode electromechanical resonance for various bias voltages, V_{gate}^{DC}, at a drive voltage of V_{NW}^{AC}=0.4 V and a driving bias voltage of V_{gate}^{AC}=6 V measured at a pressure of 4×10^{-3} bar and room temperature (c) The linear variation of the signal amplitude with DC bias voltage, V_{gate}^{DC}, (d) linear to nonlinear transition in the first mode of frequency response for various bias voltage, V_{gate}^{DC}, at a drive voltage of V_{NW}^{AC}=0.4 V and a driving bias voltage of V_{gate}^{AC}=10 V measured at a pressure of 2×10^{-12} bar and temperature of 100K (All AC voltages are peak-to-peak magnitude). 40

4.3 (Allan deviation as a function of the integration measurement time (measurement is carried out at a pressure of 2×10^{-12} bar and temperature of 100K). 41

5.1 NW geometry considered for the flexural resonator with displacements *u, v* and *w* in *x, y* and *z* directions, respectively. 48

5.2 Fundamental resonance frequency as a function of AR in EB, TM and FEM methods for (a) fixed-fixed and (b) fixed-free BCs for SCSA. . 53

5.3 Fundamental resonance frequency as a function of AR in EB, TM and FEM methods for (a) fixed-fixed and (b) fixed-free BCs for RCSA. . . 54

5.4 Fundamental resonance frequency as a function of width-to-thickness ratio in EB and TM methods for fixed-fixed BC for CL. 56

5.5 Fundamental resonance frequency as a function of aspect ratio in EB, TM and FEM methods for (a) fixed-fixed and (b) fixed-free boundary conditions for CSAV. 58

5.6 Fundamental resonance frequency as a function of surface area-to-volume ratio with FEM for (a) SCSA and (b) RCSA. 59

5.7 Quasistatic stiffness as a function of aspect ratio in EB and TM methods for fixed-fixed and fixed-free boundary conditions for SCSA geometries. 60

5.8 Fundamental resonance frequency of Ag NWs as a function of aspect ratio in EB, TM and FEM methods for (a) fixed-fixed and (b) fixed-free boundary conditions for SCSA. 62

6.1 NW geometry considered for surface stress relaxation (Left) and Bulk and Non-bulk layers in crystal orientation (Right). 74

6.2 x-displacement for copper and nickel NWs with $100 \times 30 \times 30$ unit cells at 0K for TSCB (left) and MD (right). 76

6.3 x-displacement for $31.6nm \times 10.8nm \times 10.8nm$ copper nanowire for TSCB (left) and the MD method (right) at 300K, 400K and 500K. . . 77

6.4 y-displacement field for $31.6nm \times 10.8nm \times 10.8nm$ copper nanowire for TSCB (left) and the MD (right) at 500K. 78

6.5 Uniaxial strain due to the interaction between surface and thermal stresses for $100 \times 30 \times 30$ unit cells copper and nickel NWs at different temperatures for TSCB and MD calculations. 79

6.6 Youngs modulus at different temperatures predicted by TSCB and MD calculations. 80

6.7 Youngs modulus at different temperatures predicted by the proposed method and experimentally. 81

7.1 Diamond cubic lattice structure of Si as two interpenetrating FCC lattices. 88

7.2 Illustration of the atomic arrangement on the {100} surface (grey-shaded). Black and grey atoms represent FCC lattice groups A and B, respectively. Dashed lines depict dangling bonds of the surface atom 1. 92

7.3 Schematic of atomic bonding on the {110} surface (grey shaded). Black and gray atoms represent FCC lattice groups A and B, respectively. Dashed lines depict dangling bonds of the surface atoms 1 and 2. . . 94
7.4 Thin film consists of two periodic boundary conditions in y- and z-directions and two free surfaces in x-direction. 95
7.5 (a) Atomic stress based on the virial theorem (Eq. (16)) along the thin film thickness, x, in $< 100 >$ direction with {100} free surface, (b) A close-up (within the dashed box of (a)) showing details of the atomic stress components in the immediate vicinity of the top surface (+ x). 97
7.6 (a) Atomic stress based on the virial theorem (Eq. (16)) along the thin film thickness, x, in $< 110 >$ direction with {110} free surface, (b) A close-up showing details of the atomic stress components in the immediate vicinity of the top surface (+ x). 98
7.7 x-displacement of Si NWs with crystal orientation I obtained through numerical (left) and atomistic (right) methods (in $\mathring{A}$). 101
7.8 z-displacement of Si NWs with crystal orientation I obtained through numerical (left) and atomistic (right) methods (in $\mathring{A}$). 102
7.9 y-displacement of Si NWs with crystal orientation I obtained through numerical (left) and atomistic (right) methods (in $\mathring{A}$). 103
7.10 x-displacement of Si NWs with crystal orientation II obtained through numerical (left) and atomistic (right) methods (in $\mathring{A}$). 104
7.11 z-displacement of Si NWs with crystal orientation II obtained through numerical (left) and atomistic (right) methods (in $\mathring{A}$). 105
7.12 y-displacement of Si NWs with crystal orientation II obtained through numerical (left) and atomistic (right) methods (in $\mathring{A}$). 106
7.13 Si NW near an electrostatic gate and associated dimensions. 107
7.14 Normalized electrostatic force on Si NW xy surface with crystal orientation I. 108

NOMENCLATURE

3D	Three-dimensional
AFM	Atomic force microscopy
AR	Aspect ratio
BC	Boundary condition
CD	Critical dimension
CL	Constant length
CMOS	Complementary metal-oxide-semiconductor
CNT	Carbon nanotube
CSAV	Constant surface area-to-volume
DRIE	Deep reactive ion etching
EAM	Embedded Atom Method
EMM	Engineering Molecular Mechanics
EU	Euler-Bernoulli
FCC	Face-centered cubic
FEM	Finite element method
GF	Gauge factor
HSQ	Hydrogen silsesquioxane
IC	Integrated circuit
IoT	Internet of Things
LAMMPS	Large-scale Atomic/Molecular Massively Parallel Simulator
LIRIE	Lithography and reactive ion etching
LJ	Lennard-Jones
LTO	Low-temperature oxide
MEMS	Microelectromechanical system
MD	Molecular Dynamics
NEMS	Nanoelectromechanical system
PZR	Piezoresistive
RCSA	Rectangular constant cross-sectional area
RIE	Reactive ion etching
SCB	Surface Cauchy-Born
SCREAM	Single-crystal-silicon reactive etching and metallization
SCSA	Square constant cross-sectional area
Si NW	Silicon nanowire
SOI	Silicon-on-insulator
TAR	Trench aspect ratio
TSCB	Thermo-coupled surface Cauchy-Born
TM	Timoshenko
TMAH	Tetramethylammonium hydroxide
VLSI	Very large scale integration

Chapter 1

INTRODUCTION

Silicon nanowires (Si NWs) have extreme structural configuration with nanoscale cross-sectional dimensions along with a few micrometers of length, exhibiting an inherent three-order-of-magnitude scale difference. These one-dimensional structures introduce unique mechanical, optical and electrical properties. However, contribution of these miniaturized architectures with three-dimensional (3D) structures poses integration challenges in modern electronic devices. Furthermore, surface stress incorporation in electromechanical behavior of Si NWs introduces challenges in engineering design and implementation. In this work, we address a new technology for monolithic integration of Si NWs with microscale structures following the direct implications in physical piezoresistive sensors in chapter2-4. Surface stress contribution in mechanical behavior of NWs is discussed through benchmarking studies in chapter5-7. The major outcomes of this study is summarized in the last chapter.

In the second chapter, a new technology to integrate silicon nanowire with three-dimensional devices is presented based on semiconductor manufacturing processes. The approach is based on high-resolution lithography and deep etch technology resembling the single-crystal-silicon reactive etching and metallization (SCREAM) process. A nanoscale protrusion created on the substrate surface through a shallow reactive ion etching (RIE) step is encapsulated against the detrimental effects of the subsequent deep reactive ion etching (DRIE). The isotropic component of DRIE creates a sufficiently deep undercut and thereby releases the nanoscale protrusion in the form of a Si NW. Although the fragile, encapsulated Si NW remains unprotected along its newly formed bottom surface, it survives the deep etch. As a result, the process

successfully spans a two order-of-magnitude scale gap.

In the third chapter, application of this approach to downscaling silicon piezoresistive sensors is addressed by spanning an electrostatic comb-drive actuator and a micromechanical amplifier by a single nanowire. With the associated lack of high-temperature processes and its CMOS-compatibility, the technique is a promising enabler for future miniaturized piezoresistive sensors. Further application of this approach is presented through incorporation of silicon nanowire resonator on thick silicon-on-insulator (SOI) substrates in chapter4. Results promise a new technique to scale-up integration of silicon nanowire electromechanical resonators with implementation of large arrays and process repeatability for the very-large scale integration (VLSI) processes.

In addition to the development of fabrication technology, sound computational approaches are the key to success for engineering design and implementation. A pathway of selecting the optimum engineering approach for frequency response of nanowire resonators is presented through a benchmarking study among analytical and numerical techniques at chapter 5. While analytical techniques necessitate the minimum amount of computational requirements, their applicability in extreme resonator geometries remains rather limited. Surface Cauchy-Born (SCB) approach can serve an optimum engineering tool for frequency response modeling of nanowire resonators with extreme surface stress effects. Utilizing this method to capture surface stress for mechanical modeling of nanowires is limited to 0 K. Hence, in chapter 6, an engineering finite-temperature model is presented to account surface energy for the prediction of the thermomechanical response of NWs. Furthermore, the size dependence of mechanical properties of silicon nanowires has proved to be specifically challenging with contrasting conclusions drawn from experimental and computational studies regarding the surface stress effect. A guideline for the future experimental investigations and previous controversy in the contribution of surface stress in mechanical behavior of silicon nanowires is addressed by linking the local surface stress at the atomic scale to the overall behavior of the continuum system in chapter 7.

Chapter 2

3D SCALE-UP DEVICE INTEGRATION OF SILICON NANOWIRES

2.1 Overview

Integration of Si NWs in 3D devices including integrated circuits (ICs) and micro-electromechanical systems (MEMS) leads to enhanced functionality and performance in diverse applications. The immediate challenge to the extensive use of Si NWs in modern electronic devices is their integration with the higher-order architecture. Topography-related limits of integrating Si NWs in the third dimension are addressed in this chapter. Utilizing a well-tuned combination of etching and protection processes, Si NWs are batch-produced in bulk Si with an extreme trench depth of 40 μm, the highest trench depth obtained in a monolithic fashion within the same Si crystal so far. The implications of the technique for the thick SOI technology are investigated for the first time. The process is transferred to SOI wafers resulting Si NWs with a critical dimension of 100 nm along with a trench aspect ratio of 50. Electrical measurements verify the prospect of utilizing such suspended Si NWs spanning deep trenches as versatile active components in ICs and MEMS. Introducing a new monolithic approach to obtaining Si NWs and the surrounding higher-order architecture within the same SOI wafer, this aproach opens up new possibilities for modern sensors and power efficient ICs.

2.2 Introduction

The IC is the primary example of the integration of multiple length scales, where features of the critical dimension (CD) of about 10 nm are ultimately linked to others

of characteristic dimensions as large as 100 μm, thereby spanning a four-order-of-magnitude scale difference. The most remarkable aspect of this integration is its batch-compatibility, *i.e.* the achievement of integration using top-down semiconductor manufacturing techniques based on lithography with ultimate registration capabilities [Singh, 2015]. This resulted in the historic downscaling defining the increased IC performance at a reduced cost, which was dubbed "Moore′s Law" [Waldrop, 2016].

Although a similar downscaling took place in MEMS, the incorporation of multiple length scales has proved to be much more challenging. As in IC, such multiscale systems make the best use of the respective advantages of nano and microscale components as highlighted in new-generation physical sensors [Robert et al., 2009, Dao et al., 2010]. For instance, the capability of detecting minute displacements in MEMS thanks to the introduction of highly sensitive nanoscale components lead to ultra-sensitive mechanical biosensors [Arlett et al., 2011] and inertial instruments [Lou et al., 2012]. Operational enhancement can be obtained through a functional multiscale integration approach [Dao et al., 2010, Allain et al., 2013]. Furthermore, with the advent of Internet of Things (IoT) there is a strong motivation for on-chip integration of electromechanical sensors on a massive scale [Bandyopadhyay and Sen, 2011]. However, the challenge — similar to IC — is primarily due to the three-dimensional architecture, where involved topographies can be considered extreme. For instance, embedded interconnections and electrical isolation in three-dimensional devices necessitate narrow and deep trench isolation with high-resolution micromachining [Fedder et al., 2008]. Hence, high-resolution lithography alone is not sufficient to secure the success of multiscale integration, where a new approach to processing is needed.

To answer this need for multiscale integration, a wealth of bottom-up approaches was developed over the years [Erdem Alaca, 2009]. In the majority of integration studies, bottom-up synthesis is followed by field-assisted self-assembly [Lu and Lieber, 2007]. While self-assembly is a valid tool in applications with less stringent requirements on spatial resolution of integration, it falls short of meeting the

demands of the deterministic integration as laid out by semiconductor manufacturing [Singh, 2015]. As an alternative, synthesis sites can be defined via high-resolution lithography, a hybrid approach linking self-assembly with top-down fabrication, where integration is generally limited to out-of-plane growth [Erdem Alaca, 2009]. Pick-and-place assembly is yet another top-down approach for manipulating and placing synthesis products. Due to the high level of control it provides, pick-and-place assembly is a highly preferred tool in pilot studies, while the assembly time is the major drawback. For example, compared to printed wiring board assembly in terms of the number of assembled parts, pick-and-place assembly via scanning probe microscopy is three orders of magnitude slower [Morris et al., 2005]. In this context there is a certain lack of sound technologies with the capability of bridging significant scale gaps in a batch-compatible fashion. Hence, innovative approaches based on semiconductor manufacturing are in high demand [Singh, 2015].

One such technique was recently demonstrated for the monolithic incorporation of Si NWs in bulk Si in the presence of an etch depth of 10 μm [Tasdemir et al., 2016]. The approach is based on high-resolution lithography and deep etching technology and resembles the SCREAM process [Shaw et al., 1994]. A nanoscale protrusion created on the substrate surface through a shallow RIE step is encapsulated against the detrimental effects of the subsequent DRIE. The isotropic component of DRIE creates a sufficiently deep undercut and thereby releases the nanoscale protrusion in the form of a Si NW. Although the fragile, encapsulated Si NW remains unprotected along its newly formed bottom surface, it survives the deep etch. As a result, the process successfully spans a two-order-of-magnitude scale gap.

The present chapter inquires further into the deep etch limit provided by this technology. For this purpose, a single suspended Si NW is integrated into a double-gated architecture. Fabrication approach is explained in detail. Challenges associated with the structural evolution of the Si NW as a function of the etch depth are highlighted through a transmission electron microscope (TEM) study. An extreme etch depth of 40 μm is achieved for a Si NW of a CD of 80 nm in bulk Si. The successful combi-

nation of high-resolution lithography and deep trench isolation is then repeated on a thick SOI. This time the maximum trench aspect ratio (TAR) of 50 with a 200-nm trench gap is demonstrated. In addition to the etch depth of 40 μm achieved in bulk Si, this figure of TAR also sets an upper limit to match for future integration studies. Associated challenges of transferring the technology to SOI are discussed. The chapter is concluded with a discussion on the maximum achievable TAR.

2.3 Fabrication Approach

The incorporation of a NW within a higher-order architecture such MEMS or CMOS with a three-order-of-magnitude scale difference constitutes an active field of study, as NWs are shown to impart significant improvements in the operation of electronic and electromechanical systems [He et al., 2005, Appell, 2002, Jamaa et al., 2011, De Marchi et al., 2014]. Although such a quest for a monolithic approach is critical for the technological relevance and the transition from pilot systems to applications, associated efforts are marred by compatibility challenges. The foremost challenge is concerned with the protection of this miniature component against free Fluorine radicals during the deep etch stage. In the present work, the limits of such a nanoscale protection technology are investigated using NW bridges spanning thick Si islands. The initial demonstration of the technology was presented with an etch depth of 10 μm in bulk Si [Tasdemir et al., 2016]. The question of how deep one can etch the surrounding architecture while NWs retaining their structural integrity remains yet to be addressed.

The associated process flow is depicted in figure 2.1. Patterning of the NW is carried out by e-beam lithography using a 600-nm-thick HSQ 21% (Hydrogen silsesquioxane) resist on a p-type, $< 100 >$ Si wafer of 100-mm diameter, 525-μm thickness and a resistivity of 5 Ωcm (figure 2.1.a). HSQ is spin-coated at 4000 rpm after a wafer surface activation in Tepla Gigabatch oxygen plasma system with a power of 600 W and O_2 flow rate of 400 sccm for 5 minutes. e-beam lithography is executed in Vistec EBPG5000 system with a beam energy of 100 keV. e-beam dose calibration is carried

out to define the proper dose for the optimum e-beam size. NW pattern is defined along $< 110 >$ crystal orientation with a 2 nA beam spot and a dose of 2500 μC cm^{-2}. Exposure is followed by development in tetramethylammonium hydroxide (TMAH) 25% for 2 minutes.

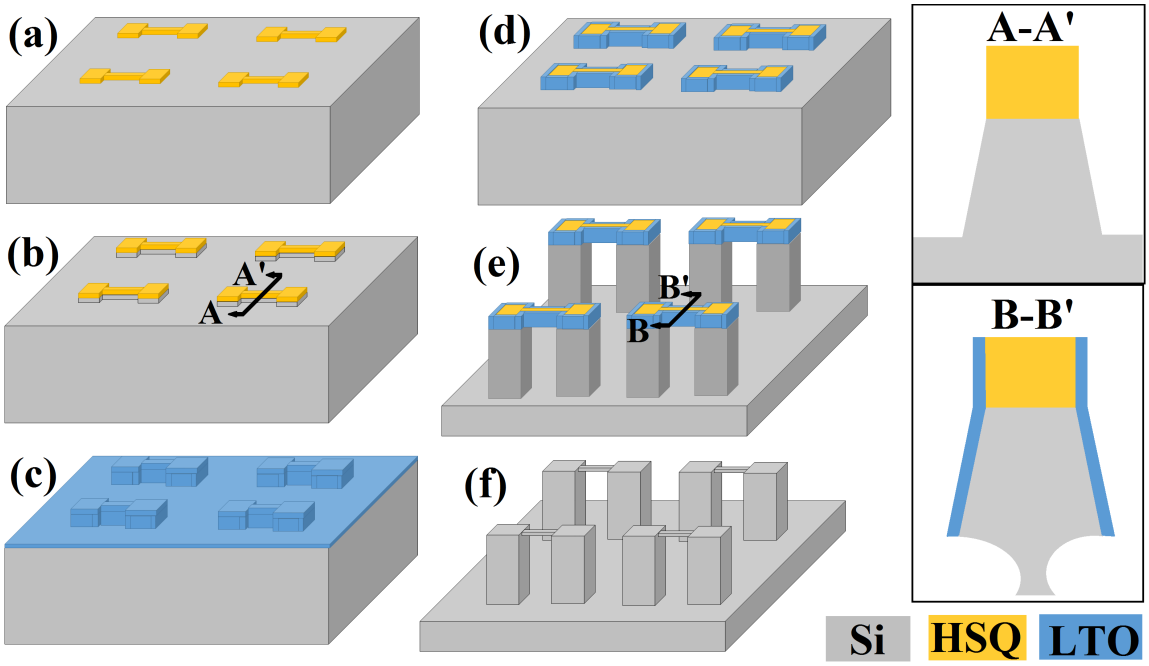


Figure 2.1: Process flow for the fabrication of suspended Si NWs, (a) e-beam lithography, (b) reactive ion etching (shallow etch), (c) low-temperature oxide coating, (d) directional oxide etching, (e) deep reactive ion etching, (f) removal of all protective layers. The sketch is not drawn to scale. Si NW has a CD of 80 nm, whereas the maximum trench depth achieved is 40 μm.

Chlorine RIE in a STS multiplex inductively coupled plasma (ICP) etcher is utilized for the anisotropic silicon thin film etching. RIE is carried out for 45 s for the definition of the NW thickness in the order of 200 nm (figure 2.1.b). Cross-section A-A′ in the inset depicts the nanoscale surface protrusion at this stage with slightly slanted sidewalls. Sidewall protection is then achieved by a conformal, 100-nm-thick low-temperature oxide (LTO) coating (figure 2.1.c) deposited in a Centrotherm furnace at 425 °C. LTO on horizontal surfaces is removed with fluorine plasma etch (figure 2.1.d). At this stage, the wafer surface is ready for the patterning of any

additional structures such as MEMS and CMOS to be integrated with the Si NW.

The generation of the surrounding microscale architecture requires DRIE. In fact, an optimized DRIE recipe consisting of plasma etching and passivation steps is to be developed to achieve multiple goals on the same substrate: i) Micromachining, for example, for the surrounding MEMS, ii) electrical isolation on SOI and iii) NW release by the scalloping effect. A proper combination of the isotropic plasma etching along with sidewall passivation is sought after for the DRIE optimization. Such a combination ensures a released NW spanning a deep trench with vertical sidewalls. In this work, plasma etching is carried out in pulses of SF_6 and C_4F_8 gases with a duration of 6.5 s and 2 s, respectively, (figure 2.1.e) in Alcatel AMS 200 DSE using Fluorine based chemistries. Cross-section B-B′ in the inset depicts the released Si NW with a non-flat bottom surface due to the scallping effect. All protection layers around the NW, including LTO and e-beam resist, are subsequently removed in hydrofluoric acid (HF) vapor (figure 2.1.f) in Idonus HF VPE-100 at 60°C.

2.4 Results and Discussion

Suspended Si NWs with different geometries are shown in the scanning electron micrograph of figure 2.2.a. NWs with two different widths (in-plane dimension) of 80 nm and 120 nm are patterned between two anchors in bulk Si. Three different aspect ratios (ARs), defined as the ratio of length to width, of 50, 75 and 100 are achieved. A close-up provided in figure 2.2.b shows an array of such NWs with extreme ARs. It is to be emphasized that in this micrographs, all features including NWs, anchors and the bottom surface are etched from the same Si crystal. Scallops stemming from the DRIE process are visible on sidewalls of anchors as depicted in figure 2.2.c, while the structural integrity of the Si NW is preserved as the close-up in figure 2.2.d suggests. Sidewall and line edge roughness are visible along the length of the Si NW as a direct result of the resist exposure in e-beam lithography. More uniformity can be achieved through proximity effect correction method [Bolten et al., 2011].

A significant improvement over prior art is achieved in this work regarding the

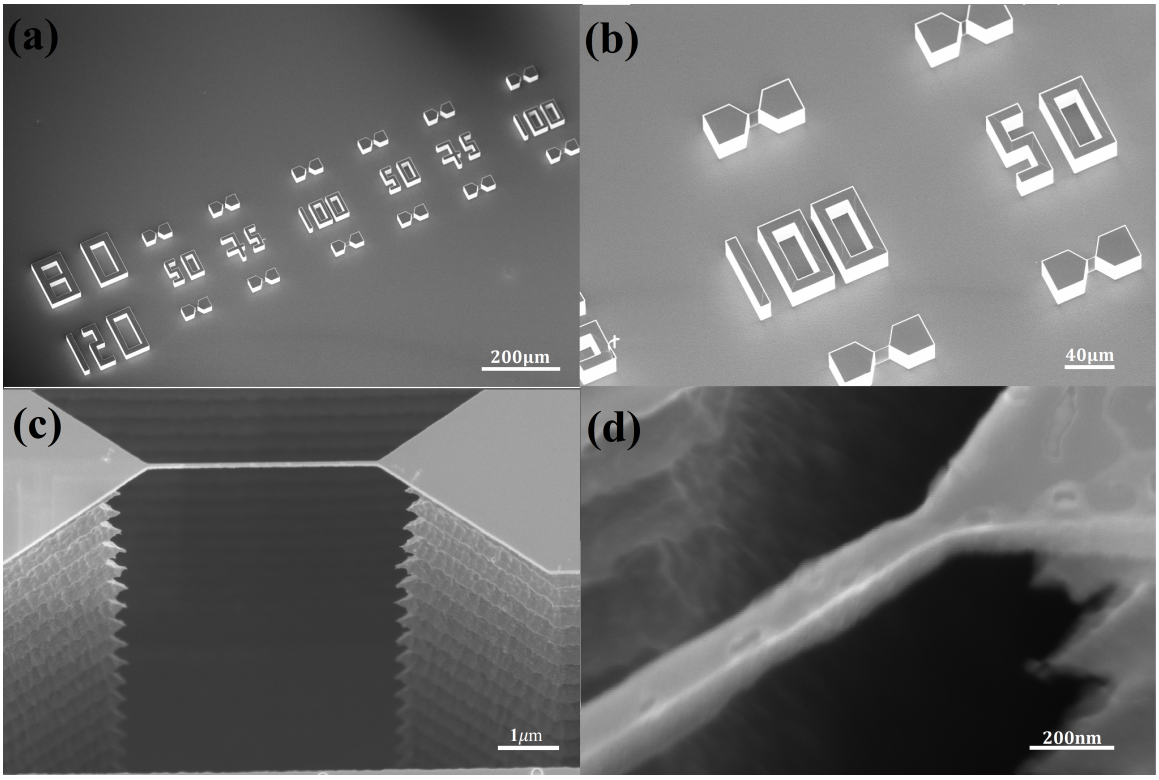


Figure 2.2: (a) An array of suspended Si NWs with a 40-μm etch depth in bulk Si. Numbers 80 and 120 refer to the width of the NW, while numbers from 50 to 100 printed parallel to NWs represent ARs. (b) A close-up of an array of NWs with ARs of 50 and 100. (c) A Si NW with a width of 80 nm and a length of 5 μm spanning a 40-μm-deep trench. (d) A close-up of the Si NW of panel (c) near its support.

etch depth. Compared to the maximum etch depth of 10 μm demonstrated so far [Tasdemir et al., 2016], the micrographs of figure 2.2 represent a four-fold increase. The extent of the scale difference between the Si NW and the trench depth is exemplified by the side views of figure 2.3. Here a uniform undercut induced by the isotropic component of the etch recipe separates Si NW from the substrate with an ultimate trench depth of 40 μm. This improvement is due to a number of factors: First, the use of a thick e-beam resist (HSQ 21%) leads to a more effective protection against plasma etching from the top-surface, thereby allowing a much deeper Si etch. Equally important is the development of a suitable DRIE recipe. DRIE step not only generates the deep trench with vertical sidewalls, it also attacks the Si NW bridge along

its unprotected bottom surface (cross-section B-B′ in figure 2.1). Similar problems resulting in the loss of the NW over much shallower trenches were reported previously [Cleland and Roukes, 1996]. While a less aggressive etching recipe is required for this purpose, it should be attacking all Si underneath the NW for a complete removal of any Si whiskers between supports. Such structures, either in the form of a vertical stack of broken Si whiskers or a complete array of intact NWs, were reported previously [Tasdemir et al., 2016]. On the MEMS front, further considerations — as related to keeping tight tolerances and achieving maximum possible TAR — are also taken into account, as DRIE process parameters have intense influence on MEMS mechanical [Chen et al., 2002] and electrical [Chen and Miao, 2007] performance.

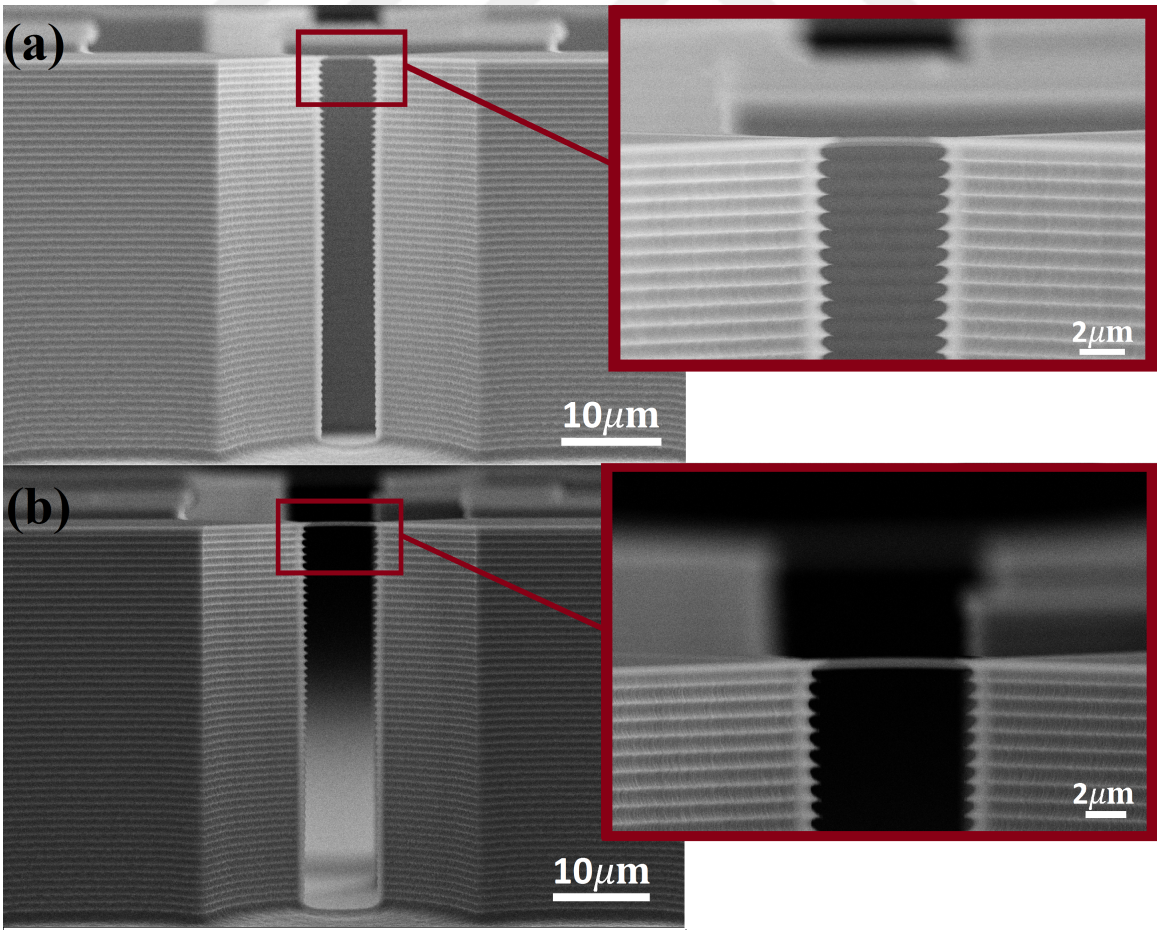
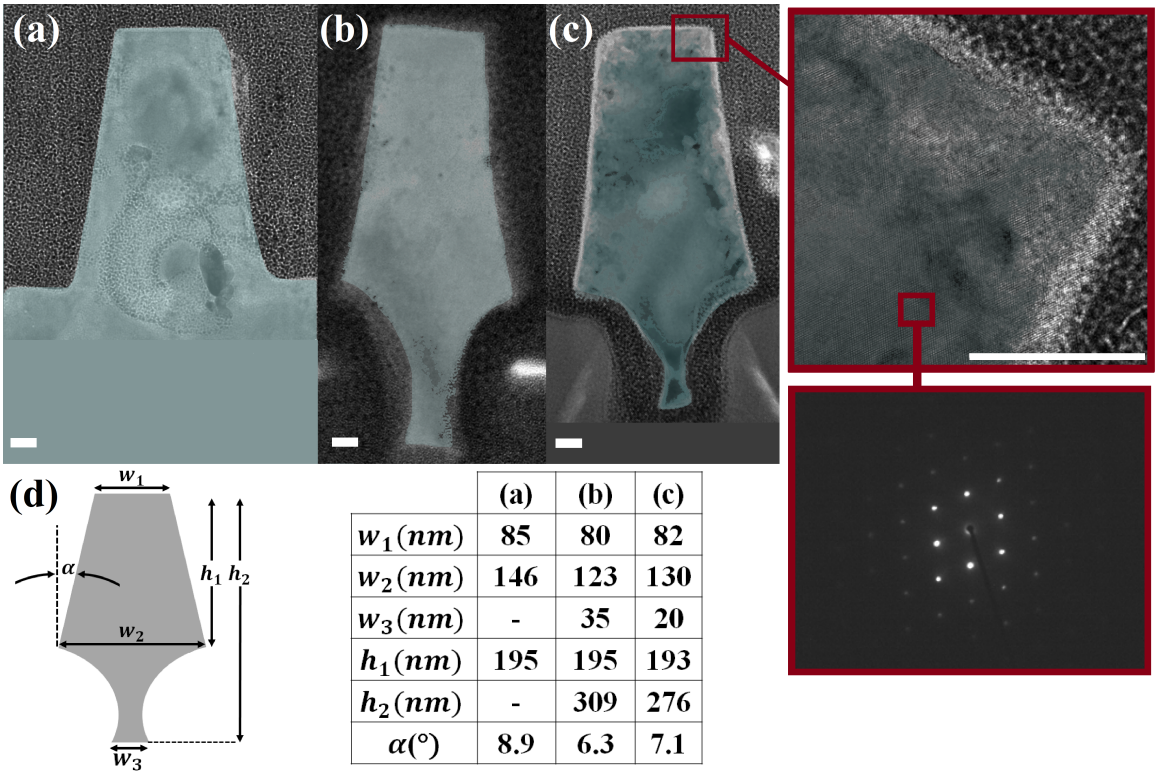


Figure 2.3: Side views of Si NWs of a width of 80 nm between two fixed supports spanning a 40-μm-deep trench. (a) 5 μm and (b) 8 μm Si NW length with close-ups.

Etching steps of figure 2.1.b representing shallow etch and figure 2.1.e representing deep etch define Si NW sidewalls and bottom surface, respectively. As the Si NW bottom surface remains unprotected throughout the deep etch process, its effect on the Si NW cross-sectional geometry needs to be studied in detail. For this purpose, the evolution of the Si NW cross-section from protrusion formation (figure 2.1.b) to the end of the release step (figure 2.1.e) with a series of different etch depths is studied via a cross-sectional TEM analysis. For this purpose, Si islands are patterned on both sides of the Si NW separated by a distance of 400 nm. TEM sample preparation starts with the deposition of platinum through a CVD process installed in the DualBeam FIB Quanta 3D FEG from FEI. This is followed by cutting a thin slice at the mid-span of the Si NW with the focused gallium ion beam at 30 kV. Omniprobe needle system is employed for *in-situ* lifting and transferring of the small slide to a half-copper ring. Thinning down the slide to electron transparency is carried out using decreasing ion beam voltage from 30 kV to 2 kV with a final polishing. The resulting thin lamella is then investigated with a TEM JEM 2200FS from JEOL.

Transmission electron micrographs highlighting the evolution of the Si NW cross-section as a function of the etch depth are shown in figure 2.4.a-c with the dimensions listed in the table provided in figure 2.4.d. The initial width of 100 nm is defined by e-beam lithography, while RIE process (figure 2.1.b) forms a trapezoidal cross-section with the NW width increasing from $w_1 = 85$ nm to $w_2 = 146$ nm at a depth of 195 nm (figure 2.4.a). The cross-section of a released Si NW after a 15-μm-deep etch is shown in figure 2.4.b. An excessive tail is formed at the bottom surface of the predefined protrusion, while the LTO mask successfully retains the trapezoidal shape. Continued DRIE process with increasing the etch depth to 30 μm reduces the extent of this bottom surface tail (figure 2.4.c). Further removal of Si sharpens the tail thereby reducing the total height, h_2, to 276 nm, while the initial trapezoidal protrusion after shallow etch remains consistent . A native oxide of 5 nm is identified at higher magnification (close-up in figure 2.4.c). Diffraction pattern indicates the crystal orientation along the NW direction. The tail at the bottom surface of the released Si NW is

the direct result of the undercut in DRIE [Rangelow, 2001]. Changes of the bottom tail with further etching can be traced back to the insufficient level of passivation. Deviation of the sidewalls from the normal to the wafer surface is related to the RIE process, while more vertical sidewalls can be achieved through changing the plasma chemistry from chlorine to hydrogen bromide [Vyvoda et al., 1998, Rangelow, 2003].



	(a)	(b)	(c)
$w_1(nm)$	85	80	82
$w_2(nm)$	146	123	130
$w_3(nm)$	-	35	20
$h_1(nm)$	195	195	193
$h_2(nm)$	-	309	276
$\alpha(°)$	8.9	6.3	7.1

Figure 2.4: Evolution of the Si NW profile as a function of the etch depth. (a) Si NW profile after shallow etch (figure 1.b). Si NW profile after DRIE (figure 1.e) with an etch depth of (b) 15 μm and (c) 30 μm with the associated high-resolution TEM image and diffraction pattern. The standard deviation of the TEM length scale measurement is 3%. All scale bars indicate 20 nm. (d) A list of cross-sectional feature dimensions.

An incorporation of lithography and reactive ion etching (LIRIE) was utilized for suspending micromechanical structures [Rangelow and Hudek, 1995]. The presented combination of lithography and etching technologies is shown to yield Si NWs successfully spanning 40-μm-deep gaps. A major challenge in the optimization of the deep etch step is related to TAR. The integration of the Si NW with the microscale

architecture, *e.g.* gate electrodes, necessitates achieving deep trenches, while trench widths are kept as narrow as possible. The substrate of interest has been bulk Si so far. However, a direct outcome of the fabrication technology is its applicability to SOI devices. The integration of the nanomechanical component with nearby electrodes over a submicron gap is frequently utilized in NEMS and FET [Jamaa et al., 2011, De Marchi et al., 2014, Husain et al., 2003, Oh et al., 2014, Wang et al., 2013]. Figure 2.5 depicts the proposed fabrication process for Si NW fabrication with narrow trench gaps on SOI. Two electrodes are placed on both sides of Si NWs keeping a submicron gap. The present technique is utilized to achieve the ultimate TAR (defined as d/w of cross-section A-A$'$ in figure 2.5) in a thick SOI device layer. This task is carried out without a significant alteration of the original process flow as depicted in figure 2.5.a-h. The ultimate achievable TAR is realized for Si NWs with lengths of 5 μm and 8 μm.

The associated fabrication flow starts again with the definition of the e-beam resist HSQ21% on a 4$''$-diameter, $< 100 >$, n-type SOI wafer with a 10-μm-thick device layer and a resistivity of $5 \times 10^{-4}\Omega$cm, a 1-μm-thick BOX layer and a 380-μm-thick handle layer (figure 2.5.a). Metal paths are defined via lift-off process of 50-nm-thick platinum by employing a 5-nm-thick chromium layer as an adhesion layer (figure 2.5.b). Si thin film etching (figure 2.5.c), LTO deposition (figure 2.5.d) and removal of LTO from horizontal surfaces via plasma etching (figure 2.5.e) are carried out in the same fashion as laid out previously in figure 2.1.b-d. Metal electrodes are then protected during the DRIE against ion-bombardment and reactive species with the e-beam resist ZEP 100% before the DRIE process (figure 2.5.f). DRIE process releases the NW, while it also forms the surrounding electrodes (figure 2.5.g). All protective layers and masks are finally removed in HF vapor (figure 2.5.h).

The process yields Si NWs with a CD of 100 nm, a maximum TAR of 50 and a minimum trench opening, w, of 200 nm. After the implementation of the process flow of figure 2.5, an electrical characterization study is conducted to measure Si NW resistance and evaluate trench isolation using Semiconductor Parameter Analyzer,

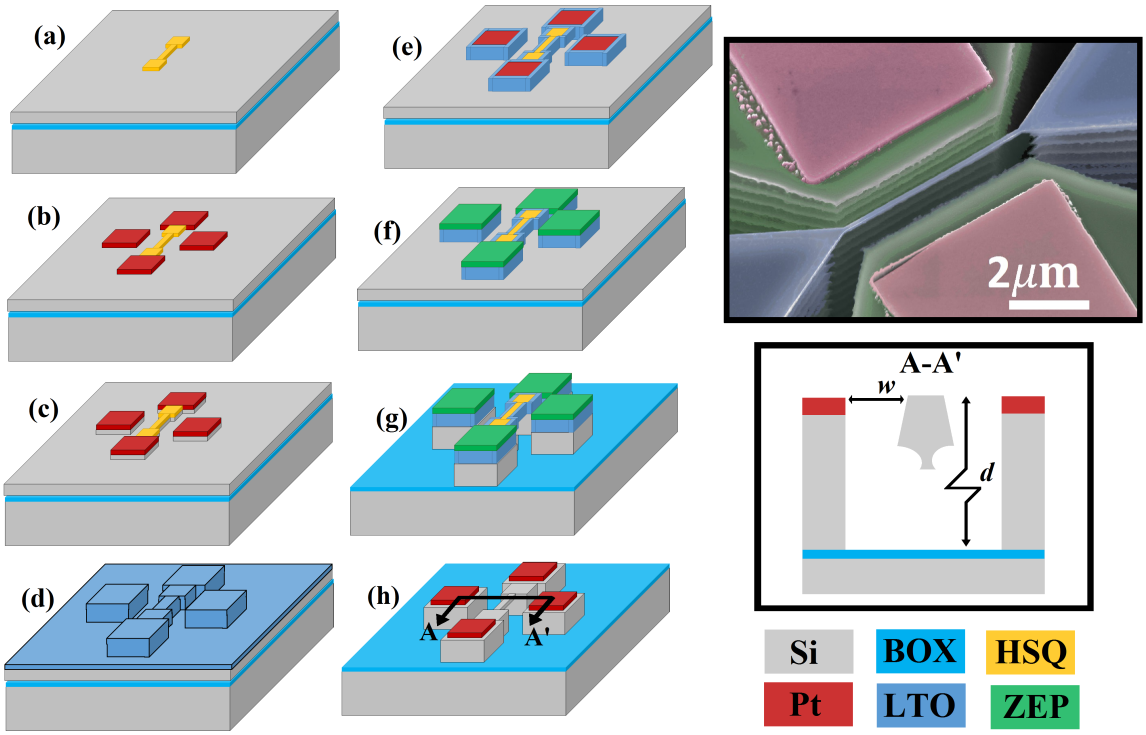


Figure 2.5: Si NW-electrode fabrication on SOI with TAR = d/w. (a) e-beam lithography, (b) metallization by lift-off, (c) reactive ion etching (shallow etch), (d) low-temperature oxide coating, (e) directional oxide etching, (f) electrode protection, (g) deep reactive ion etching, (h) removal of all protective layers. The sketch is not drawn to scale. Si NW has a CD of 100 nm, whereas the SOI device layer thickness is 10 μm. Si NW in the scanning electron micrograph with false coloring has a 5-μm length, 100-nm width and 180-nm$\pm$20-nm thickness integrated with two electrodes with TAR = 50 (blue: suspended Si NW and anchors, green: electrodes and red: metal pads).

Agilent B1500A. Results are compared with the theoretical estimation based on Si NW geometry and resistivity. Current-voltage characterization of the Si NWs for different Si NW lengths are shown in figure 2.6. Results show a standard deviation in the order of 15% and 8% for Si NWs with a length of 5 μm and 8 μm, respectively. Experimental evaluation is carried out for 10 different samples for each Si NW geometry. Error between experimental and theoretical calculation is less than 10%.

Compressive [Allain et al., 2012b] and tensile [Najmzadeh et al., 2009] stresses in suspended Si NWs are imposed by the substrate and high-temperature oxidation, respectively. In this study, buckling was not observed indicating stress-free substrate.

Electrical characterization (figure 2.6) demonstrates negligible tensile stresses in Si NWs. The highest temperature in the present technology is achieved in LTO process before releasing Si NWs, while high-temperature thermal oxidation induces tensile stress in suspended Si NWs [Allain et al., 2012b]. Hence, conformal oxide coating through LTO process can be considered as an alternative approach for sidewall protection instead of thermal oxidation [Cleland and Roukes, 1996].

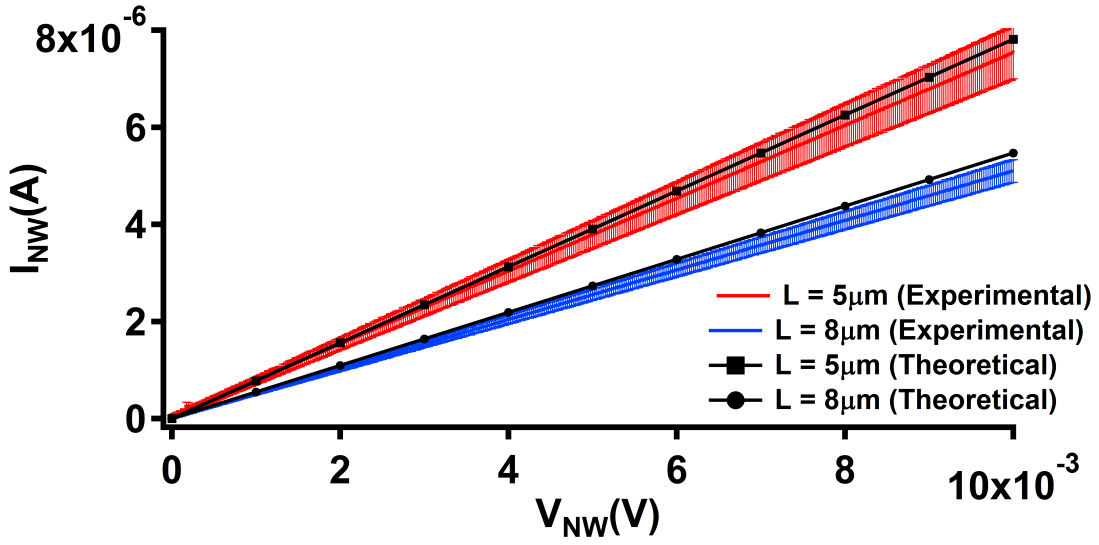


Figure 2.6: Current-voltage characteristics of the Si NWs with 100-nm width and 180-nm±20-nm thickness integrated with two electrodes with TAR = 50, and w = 200 nm.

We have shown the successful implementation of a monolithic multiscale integration approach, where Si NWs are obtained on a thick SOI. The present technology enables access to Si NWs as an active component beside other microelectronic or microelectromechanical devices on the same substrate. Incorporation of high-resolution lithography and a two-step etching process exhibits a state-of-the-art mechanical precision, where a two-order-of-magnitude difference between the Si NW and the microscale component is achieved with an ultimate TAR of 50.

Scale-up integration of Si NWs with massive microstructures is already introduced in various applications. One of the leading examples is the new-generation inertial

instruments with separate Si layers for the Si NW and MEMS. Here a thin SOI is used to generate the Si NW with a subsequent thick Si coating dedicated to MEMS [Robert et al., 2009, Allain et al., 2013]. Working on the same SOI for both the nano and microscale components, as proposed in this work, provides a promising simplification for the process technology. Furthermore, the present technology addresses the co-fabrication of NEMS with 3D-ICs for low power system designs. Such integration benefits from the advantage of near-zero leakage characteristics of NEMS along with high ON current of CMOS [Dadgour and Banerjee, 2009] with higher device density [Lau, 2014]. Scale-up integration approach introduces the feasibility of employing Si NWs for non-planar memories [Sacchetto et al., 2012, Liu et al., 2005]. Such high-density memory devices can be integrated with 3D-ICs in a monolithic fashion to reduce the gap between logic and memory performances [Liu et al., 2005].

2.5 Conclusion

The proposed semiconductor manufacturing approach is a new technology answering the needs of the multi-scale integration involving Si NWs. It is shown to work well with non-planar architecture and topographies, which can be considered extreme. It is monolithic and CMOS-compatible. A two-or-of-magnitude scale difference can be generated on the same SOI wafer, where nano and microscale features are obtained in the same batch. The approach is top-down and based on a combination of high-resolution lithography and a two-step etching process. A shallow etch defining the Si NW in the form of a surface protrusion is followed by a deep etch process, where a sufficiently extensive undercut releases the nanoscale protrusion in the form of a Si NW. During the same process microscale features are generated as well. Employing a conformal mask on the nanoscale protrusion is shown to protect Si NW up to an etch depth of 40 μm, the highest figure obtained so far in a monolithic fashion. Transmission electron micrographs reveal the evolution of Si NW cross-section providing a key understanding for the structural integrity of the obtained features. The proposed technology is also applied to SOI wafers. Si NWs are obtained with a TAR of 50

utilizing trench gaps as low as 200 nm. An expected behavior with a well-defined resistivity is obtained upon their electrical characterization. Hence, the approach is shown to successfully provide monolithic, stress-free Si NWs opening up a new opportunity for the manufacturing of Si NWs as a component of advanced 3D devices including MEMS and 3D ICs. Low-leakage FET switches, active NEMS resonators on thick substrates and miniature sensors with piezoresistive transduction are some of the promising applications enabled by the proposed technology and expected to become an integral part of next-generation microelectronic and microelectromechanical systems.

Chapter 3

DOWNSCALING OF SILICON PIEZORESISTIVE SENSORS

3.1 Overview

Multi-scale integration remains as the primary challenge in the fabrication of miniature piezoresistive sensors, as the co-fabrication of a silicon nanowire along with a microscale shuttle is the main architecture facilitating high-sensitivity transduction. The efforts in this field are marred by the lack of batch techniques compatible with semiconductor manufacturing. The technology introduced in chapter 2 is utilized here that leads to the fabrication of a piezoresistive silicon nanowire sharing the same single-crystalline device layer of a thick silicon-on-insulator wafer as the microscale component. As detailed in chapter 2, the approach is based on a combination of high-resolution lithography with a two-stage etching process. The demonstration is carried out by spanning an electrostatic comb-drive actuator and a micromechanical amplifier by a single nanowire. A gage factor range of 135 - 145 is obtained corresponding to an almost 20% resistance change for a nanowire strain of 1.26×10^{-3}. The technique is shown to generate a two-order-of-magnitude scale difference within the same silicon crystal. It also provides ease of electrical access to the nanowire, as the nanowire does not remain buried underneath the thick micromechanical system. With the associated lack of high-temperature processes and its CMOS-compatibility, the technique is a promising enabler for future miniaturized piezoresistive sensors.

3.2 Introduction

The use of Si NWs leads to unique developments in the fields of electronics [Bobba et al., 2012], communications and photovoltaics [Priolo et al., 2014] thanks to a set of surface and quantum confinement related effects. In addition, nano electromechanical systems (NEMS) gain further importance benefiting similarly from miniaturization. In this aspect, Si NWs constitute promising building blocks of ultra-sensitive, next-generation force sensor platforms used in physical [Naik et al., 2009] and biological[Patolsky and Lieber, 2005] sensing applications. Although Si NWs facilitate high-frequency operation [Truitt et al., 2007], low-power gain in electrostatic transduction poses a significant challenge. Piezoresistive (PZR) effect in Si NWs is introduced as an alternative efficient transduction method with promising improvements in nanoscale sensors [He et al., 2008]. The significance of the use of PZR effect in sensing applications is further highlighted by the introduction of the giant PZR effect through downscaling [He and Yang, 2006].

Various techniques for the successful measurement of Si NW PZR gauge factor (GF) are presented improving design and implementation of ultrasensitive detection [Koumela et al., 2011, Zhang et al., 2011, Neuzil et al., 2010]. One such sensing improvement lead to the emerging possibility of replacing capacitance-based motional detection, frequently used in MEMS, by high-sensitivity PZR systems via Si NW use [He et al., 2008]. A NW architecture is initially utilized as a nanoscale mechanical gauge [Wu et al., 2006] embedded within a microscale component, whose minute displacements are to be measured [Duc et al., 2007]. Si PZR effect is dopant-dependent [Tufte and Stelzer, 1963]. Hence, placing Si NWs in spots of maximum stress concentration along with the selective doping of both Si NWs and their contacts are required for forming PZR bridges for resistance tracking. Current leakage and fabrication complexity are the major difficulties associated with the use of PZR transduction in the embedded nano-gauge technique [Barlian et al., 2009]. Releasing the highly doped nanoscale gage in a suspended Si NW configuration addresses such challenges. However, suspended Si NWs have to be anchored to significantly thicker, microscale

shuttles posing integration issues.

A multiscale integration approach was presented earlier for a three-dimensional accelerometer concept [Robert et al., 2009]. The fabrication technique is based on the general definition of a NW on a thin SOI wafer through high-resolution lithography followed by etching. The process is followed by oxide encapsulation of Si NW and a subsequent deposition of a few-micron-thick Si layer as the MEMS component resembling EPi-SOI process [Renard, 2000]. A series of applications of this technique are reported for magnetometers [Ettelt et al., 2014] and gyroscopes [Walther et al., 2012]. Further applications in microphones [Guianvarc'h et al., 2013], pressure [Soon et al., 2010] and flow sensors [Zhang et al., 2012] benefit from the advantages of strain concentration in miniaturized PZR Si NWs and the amplified motion of the attached MEMS platform. Although pick-and-place integration technique [Zhang et al., 2011] is eliminated through the deposition of the additional Si layer for the MEMS component, the process cannot be completed using the device layer of the SOI wafer only. Furthermore, Si deposition through epitaxy necessitates high-temperature processing, while doped polySi growth requires complex process control regarding the uniformity of thickness and dopant concentration [Barlian et al., 2009]. In addition, thickness constraint imposed by the SOI device layer [Renard, 2000] is the major drawback for large-scale manufacturing. Hence, designing different PZR Si NWs on a single substrate is not possible. Finally, electromechanical properties of the additional doped Si layer for MEMS need to be tailored. Such shortcomings of this multi-layer approach can only be addressed through a monolithic integration of the Si NW with the MEMS component within the same device layer of an SOI wafer.

Monolithic Si NWs in bulk Si were recently achieved with an etch depth of 10 μm[Tasdemir et al., 2016], where a successful combination of high-resolution lithography and deep etch technology was developed resembling the SCREAM process[Shaw et al., 1993, Shaw et al., 1994]. The fabrication technique is based on the definition of a primary nanoscale protrusion on a thick substrate surface. The subsequent oxide encapsulation protects Si NWs throughout the following DRIE

process, during which the surrounding microscale architecture is generated. The process successfully spans a two-order-of-magnitude scale gap. DRIE process imposes a sufficiently deep undercut and thereby releases the nanoscale protrusion in the form of a Si NW. The structural integrity of the connection between the Si NW and its anchors was also verified by a series of nanomechanical tests highlighting the importance of the monolithic approach for creating a reliable interface between the micro and nanoscale components[Wollschläger et al., 2016]. Definition of Si NW through a shallow RIE process raises the possibility of obtaining Si NWs of different thickness on a single substrate.

Alignment of the Si NW axis with respect to the direction of MEMS motion, protection of Si NW during DRIE and design optimization for DRIE are the challenges ahead for the monolithic downscaling of Si NW PZR sensors using SOI technology. The present chapter addresses these challenges. Suitable protection of the nanoscale component during DRIE along with the development of a suitable DRIE recipe are the two most critical process aspects for securing a two-order-of-magnitude scale difference in the same batch. To the best of our knowledge, this is the first demonstration of PZR Si NW characterization integrated with MEMS within the same thick SOI platform. In the remainder of this chapter, electromechanical design and analysis of a comb-drive actuator integrated with a suspended Si NW is introduced first. The device is intended to carry out PZR characterization on Si NWs through uniaxial stretching via electrostatic actuation. A fabrication technique is developed for a highly doped, 10-μm-thick SOI wafer delivering a Si NW and the attached MEMS actuator in a single run. The chapter is concluded by the demonstration of the PZR effect through the measurement of GF for different Si NW geometries.

3.3 Device Design and Analysis

Integrated MEMS-NW architecture of this study is represented schematically in figure 3.1.a. It consists of an electrostatic comb-drive actuator, a mechanical amplifier and a NW spanning the gap between these two components. The motion of the actuator is

translated to the mechanical amplifier through the uniaxial stretching of the NW. The net displacement the Si NW undergoes is enhanced through the use of the mechanical amplifier. The amplifier is designed based on the double-folded flexural beam concept as depicted in figure 3.1(a)[Legtenberg et al., 1996]. The mechanical amplifier consists of four double-folded springs and serves the purpose of controlling the uniaxial strain on the Si NW. While this electromechanical setup allows a highly-controlled application of uniaxial strains, a simultaneous characterization of the current-voltage behavior of the stretched NW is also possible. figure 3.1.a depicts the associated electrical circuitry as well. Applied potentials include the actuator voltage, V_{MEMS}, Si NW potential, V_{NW}, and ground potential on the mechanical amplifier. The shuttle is also kept at potential V_{NW}. The potential difference between fixed and movable comb fingers creates an electrostatic attraction. The finger geometry is provided as an inset in figure 3.1.a, where L_1, L_0 and g represent zero-voltage overlap, finger length and gap between fingers, respectively. In-plane motion of the actuator takes place in the x-direction. Si NW acts as a resistive connection between the actuator shuttle held at V_{NW} and the mechanical amplifier at ground potential, thereby carrying an electric current, I_{NW}. Electric connections are made with spring anchors, while the contribution of springs to the electrical resistance is reduced through extending metal to Si NW anchors.

The displacement of the shuttle, U_{MEMS}, is imposed on the Si NW and consequently induces a displacement in the mechanical amplifier, U_{Amp}. The difference between U_{MEMS} and U_{Amp} is the net elongation of the Si NW. figure 1.b shows the lumped force-displacement model and the electrical connections of the Si NW PZR measurement setup. K_{MEMS}, K_{NW} and K_{Amp} are the stiffness values of the actuator, the NW and the mechanical amplifier, respectively. Uniaxial strain in the NW, ε_{NW}, can be calculated from the quasi-static equilibrium of the lumped system as

$$\varepsilon_{NW} = \frac{U_{MEMS} - U_{Amp}}{L_{NW}} \tag{3.1}$$

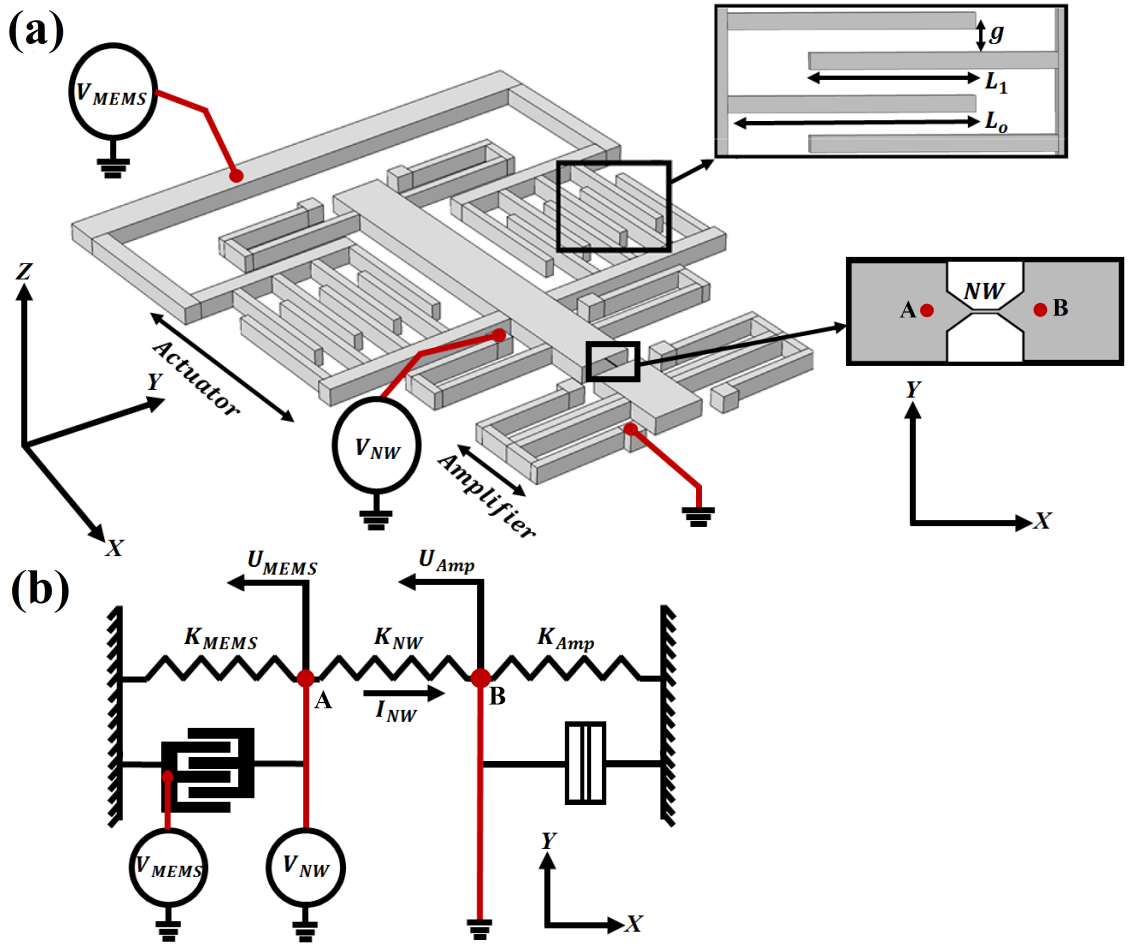


Figure 3.1: (a) Schematic of the device consists of actuator, Si NW and mechanical amplifier, (b) lumped mechanical model with electrical connections. The axis of loading, x, is aligned along $< 100 >$ crystal orientation.

$$U_{MEMS} = F_e\left(\frac{1}{K_{MEMS} + K_0}\right) \tag{3.2}$$

$$U_{Amp} = F_e\left(\frac{K_0}{(K_{MEMS} + K_0)K_{Amp}}\right) \tag{3.3}$$

where

$$K_0 = \frac{K_{NW}K_{Amp}}{K_{NW} + K_{Amp}} \tag{3.4}$$

Here F_e is the actuator electrostatic force and L_{NW} is the length of the NW. Electrostatic force can be calculated either with the simplified parallel-plate model

or by including fringe effects in finite element analysis. Uniaxial motion is not the only displacement component in comb-drive systems. Levitation and pull-in are to be considered as well. Levitation, z-displacement, is caused by the fringe field lines on the top of the fingers imposing an additional out-of-plane motion of the shuttle. Similarly, pull-in takes place, when mechanical stiffness can no longer compensate electrostatic force gradient. Although a low value of K_{MEMS} is preferred for large actuator displacement, pull-in criteria set a lower limit for the actuator stiffness [Legtenberg et al., 1996].

Si NW GF is defined based on the change of resistance, ΔR, as a function of the applied uniaxial strain as given in equation 3.5.

$$\frac{\Delta R}{R_0} = GF.\varepsilon_{NW} \tag{3.5}$$

where R_0 is the Si NW resistance under zero load. GF measurement is conducted by monitoring I_{NW}, current through the stretched Si NW. The measured resistance is a combination of the resistances of the Si NW and folded springs in addition to the contact resistance. This contact resistance is the direct outcome of the metal-semiconductor junction at nodes A and B in figure 3.1.b. Thus, including these additional components of resistance in the formulation is required, especially in the case of low doping levels of the Si device layer [Cui and Lieber, 2001] or applying a high potential on the Si NW [Zhang et al., 2011].

The actuator is designed to apply low uniaxial strains (less than 0.15%) on the attached Si NW with two distinct geometries as listed in Table 3.1. Here w corresponds to NW width, while t represents thickness. NW cross-sections are nearly rectangular as verified by previous cross-sectional TEM studies [Tasdemir et al., 2016]. Table 3.1 also provides a list of relevant dimensions and stiffness values of the actuator and the mechanical amplifier as predicted by the Euler-Bernoulli beam theory.

IV measurements are conducted under constant V_{NW} while sweeping V_{MEMS}. A Semiconductor Parameter Analyzer, Agilent B1500A, with B1517A SMU is used with a probe station. The equivalent contact resistance between probe pads and Si NW

Table 3.1: Device geometry and following lumped parameters. An actuator is designed for NWs with two different lengths.

NW	w *(nm)*			100	
	t *(nm)*			180	
	#1	L_{NW} (μm)	5	K_{NW}(N/m)	612
	#2	L_{NW} (μm)	8	K_{NW}(N/m)	382.5
Actuator	g (μm)			2	
	L_1 (μm)			50	
	L_0 (μm)			70	
	K_{MEMS} (N/m)			10.8	
Mechanical Amplifier	K_{Amp} (N/m)			10.8	

was measured to be 60-80 Ω. Compared to R_0 obtained through experimental and theoretical calculations in Section 3.5, which is on the order of $k\Omega$, this additional resistance remains negligible.

3.4 Fabrication Process

A monolithic approach to the integration of a Si NW with a MEMS actuator on a single SOI wafer is introduced. A 4"-diameter, $< 100 >$ wafer with a 10-μm-thick device layer, a 1-μm-thick BOX and a 380-μm-thick handle layer is used. The wafer is first doped with phosphorous to a mean resistivity of $5 \times 10^{-4} \Omega cm$. Doping was carried out in $POCl_3$ atmosphere at 1100 °C by creating a highly doped phosphorus oxide on the top surface. Then diffusion of phosphorus is conducted in nitrogen at 950 °C.

In the first step, Si NW is patterned with a 600-nm-thick e-beam resist HSQ 21% (Hydrogen silsesquioxane) in $< 100 >$ crystal orientation (figure 3.2.a). e-beam lithography is conducted in Vistec EBPG5000 system with a calibrated dose of 2500 $\mu C cm^{-2}$ and a beam energy of 100 keV. The subsequent resist development is carried

out in tetramethylammonium hydroxide (TMAH) 25% for 2 minutes. NW patterning is followed by metallization through lift-off. A 400-nm-thick PMMA 495k A8 and 160-nm-thick PMMA 950k A4 e-beam resists are spin-coated as the bottom and top layers, respectively. Following e-beam lithography with a dose of 1200 μCcm^{-2}, the development is carried out in MiBK (Methyl isobutyl ketone) for 1 minute and then IPA (Isopropyl Alcohol) for 1 minute. A 50-nm-thick platinum is coated through e-beam evaporation process after a 5-nm-thick chromium adhesion layer in a LAB 600H system. Lift-off process is carried out in an acetone bath for resist removal for 24 hours (figure 3.2.b).

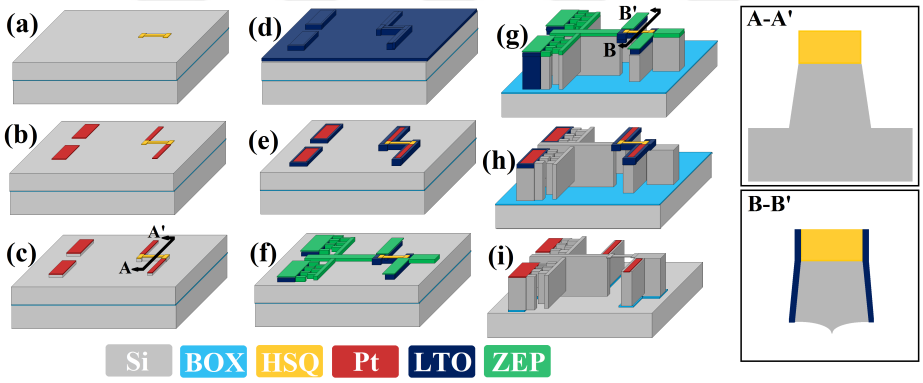


Figure 3.2: Si NW integration with MEMS on SOI. (a) e-beam lithography, (b) metal deposition by lift-off, (c) shallow Si etch, (d) low-temperature oxide coating, (e) directional oxide etching, (f) MEMS patterning, (g) deep reactive ion etching of Si, (h) resist removal and (i) release in HF vapor. Sections A-A' and B-B' depict Si NW protrusion after shallow etch and Si NW cross-section after deep etch, respectively. The sketches are not drawn to scale. Si NW has a CD of 100 nm, whereas the SOI device layer thickness is 10 μm.

Lift-off is followed by the first Si etching step. This is a shallow etch process defining the height of the Si NW. In this step, RIE with chlorine chemistry (Cl_2) is carried out in a STS multiplex inductive plasma etcher with a flow rate of 50 sccm and pressure of 5 mTorr. Metal lines as well as e-beam resist HSQ 21% serve as etch masks. This process is carried out to a depth of about 200 nm defining the Si NW in the form of a surface protrusion (figure 3.2.c). The cross-section A-A' of figure

3.2.c depicts one such structure. The trapezoidal cross-section is an indication of the RIE process [Vyvoda et al., 1998] and has been previously observed in our studies on bulk Si as well [Tasdemir et al., 2016]. A 100-nm-thick conformal low-temperature oxide (LTO) (figure 3.2.d) coating is carried out in a Centrotherm furnace through oxidation of Silane (SiH_4) at 425 °C with a pressure between 90 $mTorr$ and 250 $mTorr$. LTO on top surfaces is then removed by fluorine plasma etching in a SPTS Advanced Plasma System (APS) with fluoroform (CHF_3) (figure 3.2.e). This ensures adequate sidewall protection during the subsequent deep Si etching process.

Having achieved the definition of the nanoscale component, the next stage is concerned with the patterning of the higher-order structure. In our specific case this corresponds to MEMS consisting of the actuator and the mechanical amplifier. This aspect requires etching through the whole thickness of the device Si layer. For this purpose, e-beam lithography with a 500-nm-thick e-beam resist, ZEP 100%, is carried out, where MEMS is aligned with respect to the already formed Si NW protrusion (figure 3.2.f). Although e-beam lithography is used for the purpose of pilot production, optical lithography or any other combination of patterning techniques [Kaestner et al., 2013] can in principle be utilized as well.

The next stage is concerned with the second and last Si etching step. This time it is the DRIE process generating MEMS, while the associated undercut — linked to scallop formation — releases Si protrusion in the form of a free-standing Si NW. This way a single Si NW spanning the gap between the MEMS actuator and the mechanical amplifier is obtained (figure 3.2.g). The optimized recipe consists of plasma etching and passivation steps in pulses of SF_6 and C_4F_8 gases with a duration of 6.5 s and 2 s, respectively. This optimization is required to remove all Si underneath the Si NW to prevent the formation of additional Si whiskers upon further widening of the Si NW [Tasdemir et al., 2016]. As the emphasis of this work is placed on miniaturization of the released structure, a width of 100 nm is considered to be adequate.

The undercut associated with the isotropic component of DRIE leaves a curved bottom surface as a remnant of the two DRIE scallops etching Si from both sides.

This is evident in previous cross-sectional TEM studies [Tasdemir et al., 2016] and highlighted in the B-B' cross-section provided as an inset of figure 3.2. Finally, release is carried out first via resist removal in Tepla Gigabatch oxygen plasma system with a power of 600 W (figure 3.2.h) and then by oxide etching in hydrofluoric acid (HF) vapor at 60 °C (figure 3.2.i) in Idonus HF VPE-100. While HF vapor releases MEMS, it also removes all protection — both HSQ 21% and LTO — from Si NW surfaces.

3.5 Results

Figure 3.3.a depicts fabrication results for one device comprised of a MEMS actuator and a mechanical amplifier with a gap of 5 μm. This gap is spanned by a Si NW as shown in figure 3.3.b. In addition, an alternative design with a Si NW length of 8 μm is realized. A pair of electrodes is placed on both sides of the Si NW with a trench width of 400 nm. Similarly, a trench width of 200 nm is obtained as well. Electrodes are utilized to curb isotropy and hence control Si etching underneath the Si NW. DRIE process is then optimized based on the trench width between Si NW and electrodes. The minimum feature size on the actuator is 5 μm for the optimization of the release step (figure 3.3.c). BOX layer is completely removed from underneath the shuttle (cross-section A-A', figure 3.3.d), while oxide remains under anchors (cross-section B-B', figure 3.3.d). Metal is deposited on the stationary shuttle and also brought close to the tips of the Si NW.

IV characteristics of the suspended NWs are examined first using samples after removing ZEP 100% resist (figure 3.2.h). A linear voltage-current relation is obtained. Measurements exhibit a resistance of 1450±215 Ω and 2080±160 Ω for Si NWs with 5-μm and 8-μm lengths, respectively. An analytical verification based on the mean resistivity and dimensions as given in Table 1 provides corresponding resistances of 1402±140 Ω and 2241±225 Ω, respectively. Hence, a close correspondence is achieved indicating the success of the doping and patterning processes. Resistance variations can be linked to the changes of dopant concentration along the wafer. Modulation of the Si NW resistance is examined similar to the field effect transistor (FET) static

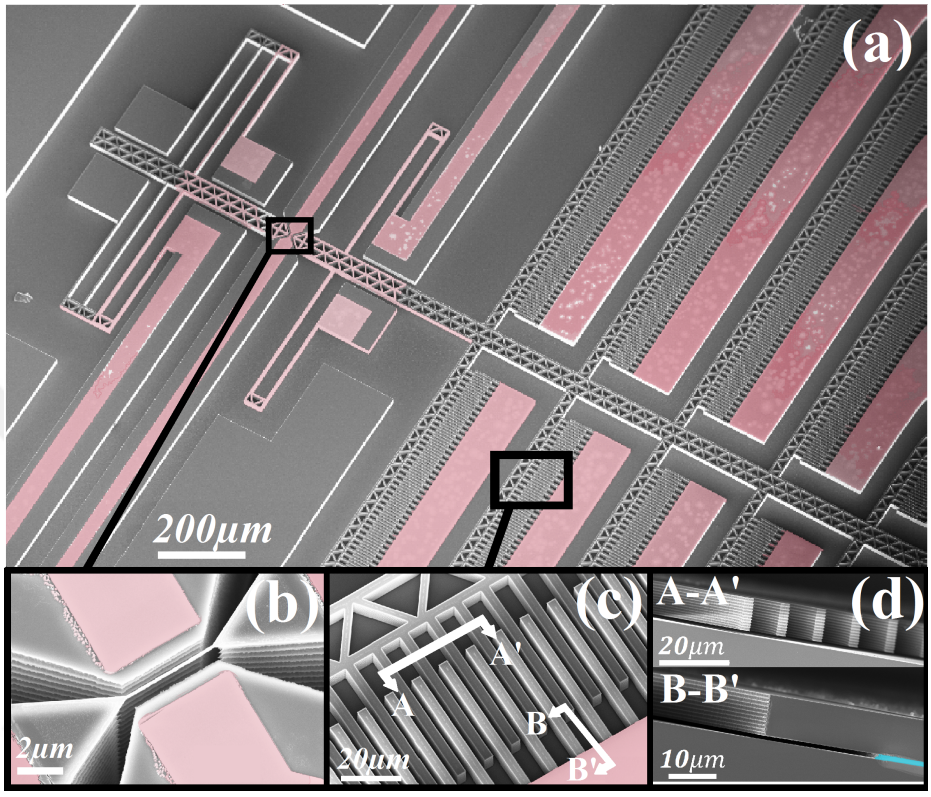


Figure 3.3: Fabricated device with false coloring, (a) the device consists of a comb-drive actuator, a mechanical amplifier and a Si NW spanning aforementioned components, (b) a close-up of the suspended Si NW between the actuator and the amplifier surrounded by two electrodes with a 400-nm gap, (c) a close-up of the comb-drive actuator, (d) cross section of comb-drive actuator highlighting anchored and released regions. Red and blue colors represent metal and BOX, respectively.

approach. No gate effect is observed as expected from the high doping level utilized in this study[Cui et al., 2000].

IV measurement is then repeated for Si NWs under uniaxial stress. For this purpose, a constant potential drop, V_{NW}, is imposed across each Si NW, while MEMS actuation voltage, V_{MEMS}, is increased at a constant rate. The current though the Si NW, I_{NW}, is then monitored using the same Semiconductor Network Analyzer and SMUs. figure 3.4.a depicts measurement results for the Si NW with a 5 μm length, while figure 3.4.b. indicates measurement results for the Si NW with a 8 μm length. In each case, I_{NW} is observed to increase upon stretching of the Si NW. A parabolic

relation is evident, which is directly reflected in the decreasing trend exhibited by Si NW resistance, also given in figure 3.4. Uniaxial strain is applied on Si NWs with different V_{NW} values between 1 mV and 10 mV, two of which, 5 mV and 10 mV, are shown in figure3.4. A resistance change of about 20% is observed for the maximum V_{MEMS} of 20 V.

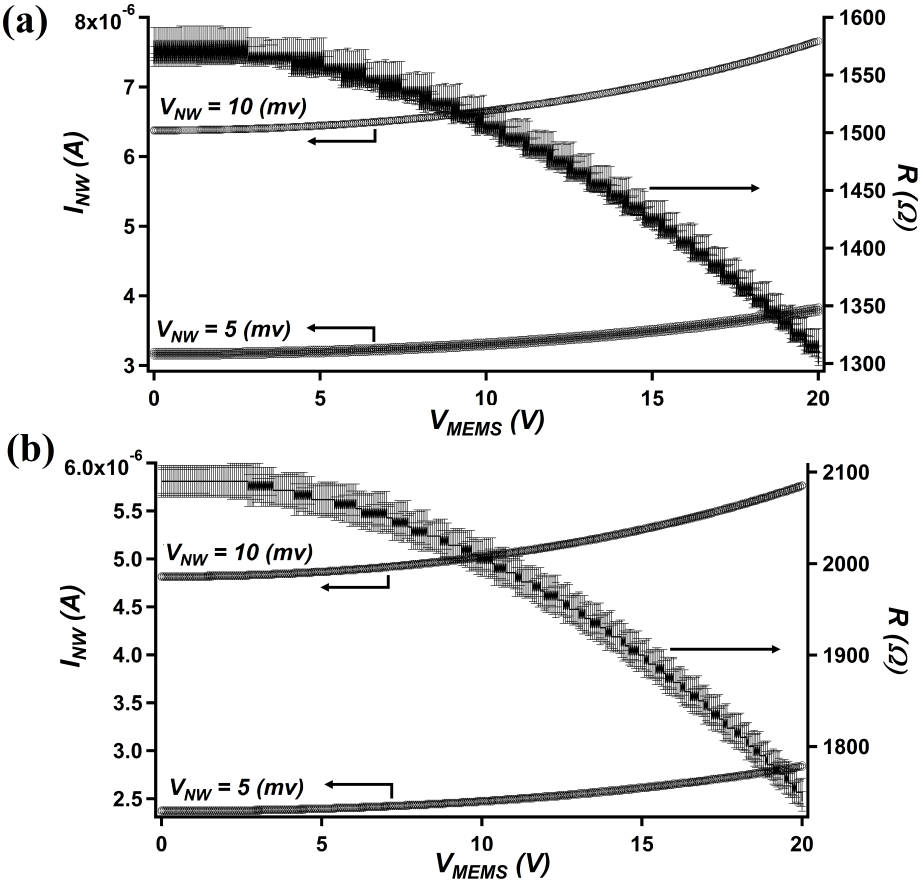


Figure 3.4: The evolution I_{NW} and Si NW resistance as a function of V_{MEMS} for Si NW lengths of (a) 5 μm and (b) 8 μm.

The dependence of GF on the resistance change is given by equation 3.3, where one needs an estimation for the imposed strain, ε_{NW}. For this purpose, a finite element analysis is carried out to calculate the electrostatic actuation force, from which ε_{NW} is then derived based on Eqns. 3.1 and 3.2. figure 3.5 provides this dependence of ε_{NW} on V_{MEMS} for different NW lengths of interest. Modulus of

elasticity of Si is taken as 168 GPa in these calculations. ε_{NW} turns out to be length-independent, because K_{MEMS} is negligible in comparison with K_{NW}, hence applied elongation is proportional to K_{NW}. The maximum strain of 1.26×10^{-3} corresponds to a displacement, U_{Amp}, of 0.3 μm for a Si NW length of 5 μm. In this case, the net stretching of the Si NW is 5.5 nm. Hence, our measurements remain within the linear elastic zone for Si [Zhang et al., 2016b]. Error bars in figure 3.5 are obtained based on the variation of Si NW dimensions as listed in Table 3.1. Displacements related to levitation in z are calculated to be less than 5 nm, a negligible number in comparison with Si NW cross-sectional dimensions and the uniaxial displacement.

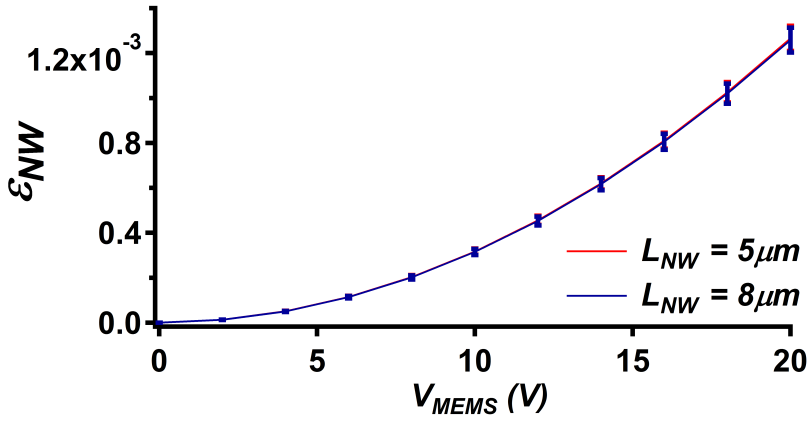


Figure 3.5: Uniaxial strain applied on Si NWs as a function of V_{MEMS}.

Having transformed V_{MEMS} to ε_{NW}, one can then find the dependence of the change of resistance on ε_{NW}. Results shown in figure 3.6 exhibit a linear trend with a constant GF. The range of GF obtained in our measurements is found to be between -145 to -135. The alignment of the Si NW pattern in crystalline orientations other than $< 100 >$ would also assist the evaluation of the corresponding GF. For practical purposes, we report the effective GF along $< 100 >$ incorporating the effect of all lateral strain components as well.

The influence of miniaturization into the nanoscale can be judged by a comparison with the heavily-doped bulk Si. Downscaling indicates a two-fold increase in

the piezoresistance coefficient [Tufte and Stelzer, 1963]. Compared to lightly-doped Si NWs with a critical dimension of 50 nm, GF in this work is more than twice indicating the effect of doping as well [Zhang et al., 2011, Kang, 2012]. Although the reported GF in this study is not in the order of those reported for the giant PZR effect, downscaling to sub-100-nm range [He and Yang, 2006] and/or field-effect gate control[Neuzil et al., 2010] are required to achieve GF in the order of 5000. The presented work is carried out in the linear elastic regime, while the transition to the nonlinear PZR behavior requires higher strains or gated Si NW[Zhang et al., 2011, Neuzil et al., 2010].

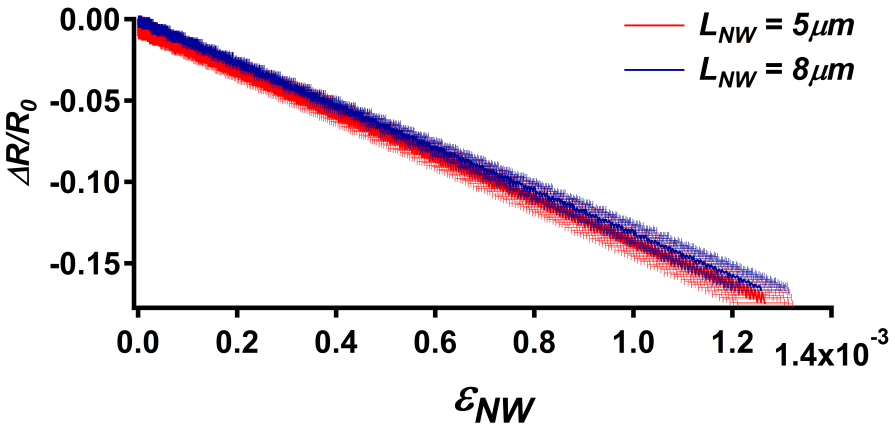


Figure 3.6: Relative change of Si NW resistance as a function of the applied uniaxial strain.

Finally, the repeatability of PZR measurements is investigated through a step-wise and repetitive application of different strain levels. Five different strains are applied at a fixed V_{NW} of 5 mV as shown in figure 3.7. Si NW is held at each strain level for a period of 20 s, after which further loading or unloading takes place. Results represent a stable and reversible electromechanical response indicating the promising nature of the proposed technique for the monolithic integration of Si NW PZR sensors.

In the proposed approach, lateral (in-plane) features are patterned by high-resolution lithography, while Si NW thickness (out-of-plane dimension) is defined by the extent of the shallow Si etch. In contrast to available techniques, this approach

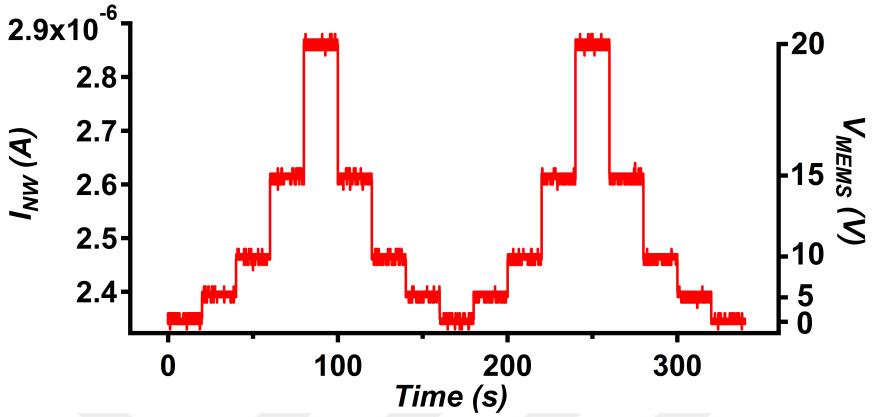


Figure 3.7: Quasistatic cyclic measurement of the current through the 8-μm-long Si NW at a constant $V_{NW} = 5$ mV subjected to a stepwise-varying actuator voltage.

provides a sound technology for obtaining Si NWs within a much thicker SOI device layer with accompanying higher-order architecture such as MEMS. The majority of alternative techniques yield a Si NW thickness equal to the device layer thickness [Arellano et al., 2008, Sansa et al., 2014, Lee et al., 2008]. Working with sub-micron device layers rules out any possibility of obtaining MEMS in the same batch. Epi-SOI process [Walther et al., 2012, Allain et al., 2012a] similarly relies on thin SOI wafers for the definition of the Si NW component. However, a much thicker Si layer is required for the definition of the MEMS component, which is deposited subsequently through a high-temperature process. There are also few studies striving to achieve a Si NW within a much thicker Si crystal. An earlier example reports the challenges of fabricating a nanoscale Si beam in bulk Si mainly related to the protection against plasma etching. Intensive etch rate in protective oxide layer, similar to Si etch rate, causes the loss of the NW over a shallow trench [Cleland and Roukes, 1996]. A more recent example employs a sequence of two Bosch processes with varying scallop sizes. Fine scallops are used to a certain depth defining the NW, after which coarse scallops are utilized for NW release and MEMS fabrication. The approach is reported to lead to contamination and rough sidewalls of the Si NW due to the presence of scallops [Tsuchiya et al., 2016]. Alternatively, oxide thinning is used for size reduction as

well [Tsuchiya et al., 2016]. Oxidation followed by sacrificial etching poses serious challenges when it comes to preserving submicron trench widths. Furthermore, generation of residual stresses upon this high-temperature process is of further concern [Najmzadeh et al., 2009]. The present method successfully addresses these shortcomings and provides Si NWs registered with MEMS within the same Si device layer. Furthermore, as the Si NWs remain close to the surface — as opposed to being buried underneath the MEMS layer — doping and surface-related processes such as contact formation become straightforward tasks to achieve.

The use of PZR transduction improves sensitivity and imparts noise immunity in various force sensor applications. A possible replacement of the capacitance-based motion detection is particularly appealing accompanied by a significant size reduction as well. Various pilot studies are reported for the use of PZR transduction in magnetometers [Ettelt et al., 2014] , gyroscopes [Walther et al., 2012], microphones [Guianvarc'h et al., 2013], pressure [Soon et al., 2010] and flow sensors [Zhang et al., 2012]. The challenges in such previous integration work include the use of separate Si layers for nano and microscale components, a high temperature budget in addition to the relative location of the Si NW with respect to MEMS. This work is aimed to address these challenges in a monolithic fashion. Hence, the present technology can be utilized in the batch-compatible miniaturization of various MEMS-based motion detectors.

3.6 Conclusion

In this chapter, we present a monolithic approach to register Si NWs with higher-order structures such as MEMS within a thick SOI device layer. The process is based on a combination of high-resolution lithography, conformal protection and a two-stage etching process, described with more details in chapter 2. A nanoscale surface protrusion generated through a shallow etch step is coated with a conformal oxide protection. A subsequent deep etch step releases the surface protrusion in the form of a NW, while the surrounding MEMS and electrode architecture are simultaneously

formed. The implications of the technique are investigated for the case of PZR transduction, where minute displacements of an electrostatic MEMS - mechanical amplifier assembly are detected via tracking of the Si NW resistance. A GF range of -145 to -135 is obtained corresponding to an almost 20% resistance change for a uniaxial NW strain of 1.26×10^{-3}. This translates to a 5.5-nm axial deformation for a NW length of 5 μm.

The resulting successful integration of Si NWs with MEMS within the same SOI device layer addresses the drawbacks of available techniques, primarily related to the difference between Si NW and MEMS thicknesses and the necessity of a separate MEMS layer deposition technique, usually a high-temperature processes. The approach is shown to accommodate a two-order-of-magnitude scale difference. Furthermore, it is CMOS-compatible and provides a straightforward path for NW doping and contact formation. As it does not rely on thin SOI technology, it also allows — in principle — the co-fabrication of multiple Si NW thicknesses on the same wafer. As this multi-scale integration is accomplished in a batch-compatible fashion, the proposed approach carries significant implications for physical and biological miniaturized PZR sensor technologies.

Chapter 4

ELECTROMECHANICAL RESONATOR APPLICATIONS

4.1 Overview

In this chapter, we present incorporation of silicon nanowire electromechanical resonators with microscale devices through the monolithic technique described in chapter 2. Frequency response of silicon nanowire resonators are characterized based on frequency down-mixing. The present chapter addresses the shortcoming related to available bottom-up and thin-substrate technologies for modern sensors and 3D-ICs.

4.2 Introduction

ICs have witnessed a unique improvement in functionality and performance through downscaling, while significant challenges lie ahead for keeping up the pace of miniaturization [Thompson and Parthasarathy, 2006]. Recent semiconductor manufacturing is marching toward 3D ICs to overcome complexity of miniaturization in conventional planar devices [Davis et al., 2005], where batch fabrication of multiple length scales is the immediate challenge. A similar development is taking place in micro electromechanical systems (MEMS), where new-generation physical sensors exploit the mechanical sensitivity brought by the introduction of piezoresistive Si NW gages into conventional MEMS architecture [Esfahani et al., 2017, Robert et al., 2009]. With a two-order-of-magnitude difference between the MEMS layer thickness and the CD of the Si NW, the associated setting is inherently 3D.

In addition to their role as stress concentration elements leading to elevated mechanical sensitivity, Si NWs also have other significant advantages such as overcoming signal losses and increasing resonance frequency, two features already widely used in

NEMS. Although integration of NEMS with CMOS technology offers improvement in power consumption for large-scale integration, the integration of NEMS with 3D ICs faces new challenges in the third dimension. Available NEMS technology has so far been defined for thin microelectronic substrates conventionally consisting of a Si NW with lateral electrodes. Suspended Si NWs in the third dimension can potentially tackle such 3D integration challenges.

As detailed in chapter2, a monolithic technology for the incorporating Si NWs in thick SOI wafers was introduced, where the Si NW remains an integral part of the SOI device layer, in which other components such as MEMS are co-fabricated [Tasdemir et al., 2015, Tasdemir et al., 2016, Yilmaz et al., 2017, Esfahani et al., 2017]. This is achieved through a combination of high-resolution lithography and a two-step etching process. The first shallow etch creates a nanoscale protrusion on the surface, which is then released through the isotropic etch component of the following DRIE. Based on this IC-compatible technology, the present chapter is the first report of its application to piezoresistive Si NW resonators in thick SOI substrates. Electrostatic actuation and piezoresistive readout are utilized. Resonance behavior is characterized for a NW geometry embedded within a 10-μm-thick device layer. Frequency response for first and second modes are presented using frequency down-mixing technique. In addition to piezoresistive sensors described in chapter 3, the applications of the technique for Si NW resonators in new-generation sensors and power-efficient ICs are investigated through addressing the shortcomings associated with available bottom-up and thin-SOI technologies.

4.3 Device Architecture and Measurement

The device is designed based on a suspended piezoresistive Si NW electromechanical resonator spanned between microscale electrodes. Electrostatic actuation and piezoresistive transduction mechanisms are utilized for electromechanical resonance. Lateral gate induces a mechanical vibration in the double-clamped Si NW. The piezoresistive behavior of the highly-doped Si NW provides the transduction between mechanical

and electrical domains. Fabrication technique is developed on a 100-mm-diameter, highly doped $< 100 >$ SOI wafer with a 10-μm-thick device layer, a 1-μm-thick buried oxide (BOX), and a 380-μm-thick handle layer. The wafer is doped with phosphorous to a mean resistivity of 5×10^{-4} Ω.cm. Fabrication details can be found in chapter 2 and 3. It should be emphasized that this technique yields Si NWs incorporated with 3D devices having an ultimate thickness of 40-μm, presented in chapter 2. Such monolithic scale-up integration technique uses an innovative combination of etching and protection processes.

A suspended Si NW between two lateral electrodes spanning a 10-μm-deep trench is shown in figure 4.1 .a. A gap of 400 nm between the Si NW and electrodes is achieved corresponding to a trench aspect (depth-to-width) ratio of 25. Frequency response of the device is characterized based on the frequency down-mixing approach. The high-frequency signal from the mechanical motion, ω_C, of the resonator is converted to a lower frequency, ω_L, to be detected by a lock-in amplifier. The frequency response is measured based on the two source-1ω detection mechanism [Sansa et al., 2012] (figure 4.1.b).

Measurements are taken within a vacuum chamber at two different pressures of 1 bar and 4×10^{-3} bar. Frequency sweeps around the first and second modes of the Si NW are shown in figure 4.1.c and figure 4.1.d, respectively. The resonance peak is detected at 43.69 MHz and 101.03 MHz for the first and second modes, respectively. The difference in the signal amplitudes obtained under the atmospheric pressure and in vacuum can be traced back to the increase of quality factor. Considering the oxide encapsulation around the Si NW, a finite element analysis for the frequency response of the resonator architecture yields resonance frequency of 47.09 MHz and 100.98 MHz for the first and second modes, respectively.

Frequency response for different gate bias voltages, V_{gate}^{DC}, is obtained through sweeping the DC bias voltage, V_{gate}^{DC}. Results are depicted in figure4.2. Increasing the bias voltage from 4 V to 15 V changes the signal amplitude from 0.2 μV to 0.8 μV at the pressure of 4×10^{-3} bar (figure 4.2.a). Second-mode peaks for the same device

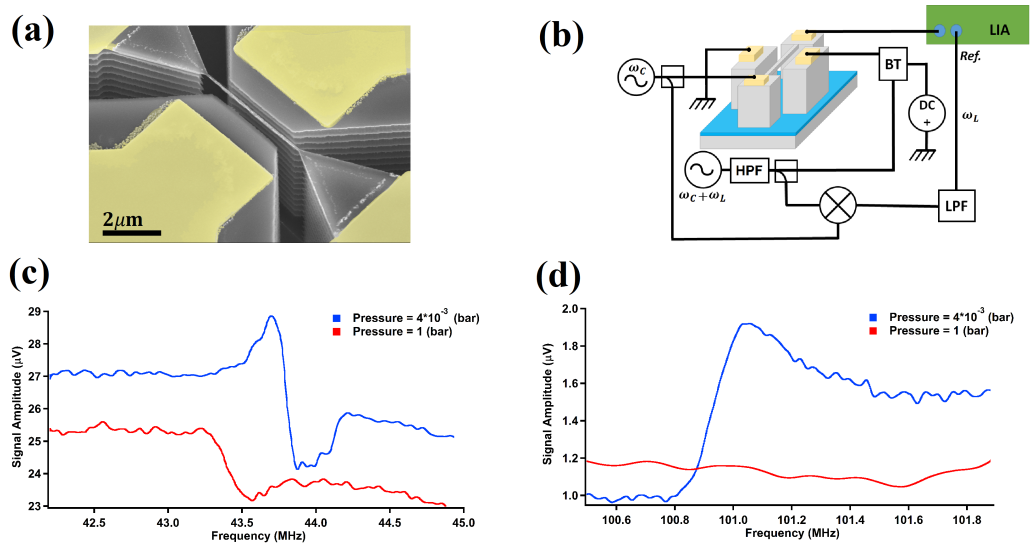


Figure 4.1: (a) Si NW resonator with a 5-μm length, 100-nm width and 200-nm thickness surrounded by two electrostatic gates with a gap of 400-nm (false color with yellow representing metal pads), (b) Schematic diagram of the measurement circuit. LIA: lock-in amplifier, BT: bias tee, LPF: low pass filter, (c) First-mode frequency response of the device at drive NW voltage V_{NW}^{AC}=0.4 V and driving bias voltage V_{gate}^{AC}=6 V at a DC level of V_{gate}^{DC}=6 V at the atmospheric pressure and a pressure of 4×10^{-3} bar , (d) Second-mode frequency response of the device at drive NW voltage V_{NW}^{AC}=0.4 V and driving bias voltage V_{gate}^{AC}=10 V at a DC level of V_{gate}^{DC}=15 V at atmospheric and a pressure of 4×10^{-3} bar(All AC voltages are peak-to-peak magnitude).

can be seen in figure 4.2.b. A linear dependence of the signal amplitude on the bias voltage is obtained for both modes as depicted in figure 4.2.c. This observation is a sign of the Lorentzian nature of the mechanical resonance [He et al., 2008]. Resonance peaks exhibit a quality factor, Q, on the order of 280-340. Furthermore, nonlinear transition in the first mode of frequency response indicates mechanical resonance in the Si NW (Fig.2.d). We note that field effect arising from the electrostatic actuation could modulate the resistance, while this effect for the highly-doped Si NW of this work is negligible [Esfahani et al., 2017]. Hence, the modulated resistance in Si NW is a direct result of mechanical strain during resonance.

Frequency stability (Allan deviation) measurement is carried out as well (figure

4.3). A fractional frequency fluctuation on the order of 3-6 ppm is achieved. The Allan deviation obtained in this study is comparable with previous studies for high-resolution mass detection [Feng et al., 2007]. This stability can be improved through further size reduction of Si NWs.

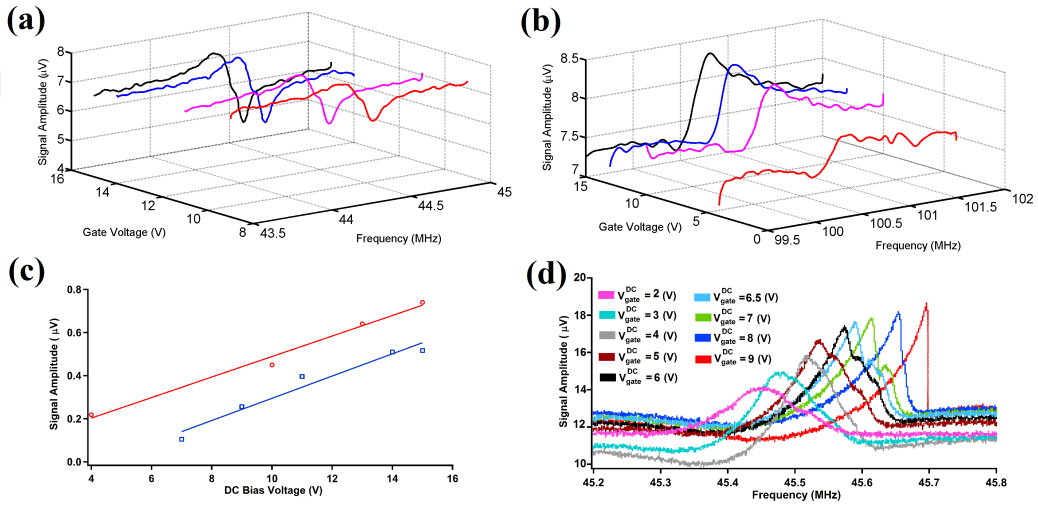


Figure 4.2: (a) First-mode, and (b) Second-mode electromechanical resonance for various bias voltages, V_{gate}^{DC}, at a drive voltage of V_{NW}^{AC}=0.4 V and a driving bias voltage of V_{gate}^{AC}=6 V measured at a pressure of 4×10^{-3} bar and room temperature (c) The linear variation of the signal amplitude with DC bias voltage, V_{gate}^{DC}, (d) linear to nonlinear transition in the first mode of frequency response for various bias voltage, V_{gate}^{DC}, at a drive voltage of V_{NW}^{AC}=0.4 V and a driving bias voltage of V_{gate}^{AC}=10 V measured at a pressure of 2×10^{-12} bar and temperature of 100K (All AC voltages are peak-to-peak magnitude).

The proposed monolithic integration of the Si NW with the surrounding microscale architecture within the same Si crystal eliminates assembly drawbacks related to bottom-up approaches. Based on standard IC-compatible processes the fabrication technology is shown to deliver Si NW electromechanical resonators within the same thick substrate with a two-order-of-magnitude scale difference between the Si NW and the surrounding architecture. This approach addresses the contribution of Si NW resonators with higher-order architectures in modern electronic devices [Thompson and Parthasarathy, 2006, Choudhury, 2010]. Implementation of *in-situ*

actuation and readout in electromechanical resonators enables the incorporation of large resonator arrays in very-large scale integration (VLSI) implementation.

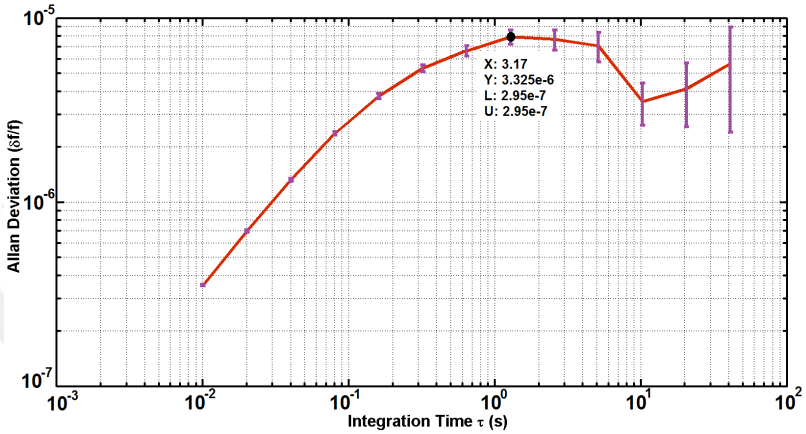


Figure 4.3: (Allan deviation as a function of the integration measurement time (measurement is carried out at a pressure of 2×10^{-12} bar and temperature of 100K).

4.4 Conclusion

In summary, contribution of Si NW electromechanical resonator and microscale devices with two-order-of-magnitude scale difference is presented. The approach uses high-resolution lithography and two steps of etching to span a suspended Si NW between lateral electrodes, detailed in chapter 2. The presented technique uses standard semiconductor manufacturing processes. Electrostatic actuation with piezoresistive transduction mechanisms are employed. Frequency measurement is carried out based on frequency down-mixing technique. Mechanical vibration in piezoresistive Si NW is depicted through pressure damping, linear behavior of signal amplitude with DC bias voltage and nonlinear transition in frequency response. The approach promises an IC- and VLSI-compatible approach for a monolithic integration of NEMS with 3D-devices.

Chapter 5

FREQUENCY RESPONSE MODELING OF NANOWIRE RESONATORS

5.1 Overview

The full potential of the nanoelectromechanical systems, NEMS, as one of the leading examples among the new-generation sensing technologies, is yet to be realized. One of the main challenges on the road is the mechanical modeling of their core elements, the tiny mechanical building blocks such as the nanowire resonators. The success of the engineering design of such miniaturized systems will depend heavily on the availability of accurate mechanistic models with the least possible computational cost. Although a variety of models are available for this purpose, the boundaries between their admissible domains remain rather vague. For example, analytical approaches including Euler-Bernoulli and Timoshenko beam theories provide closed-form solutions and work reasonably well for moderate nanowire geometries, and hence, they are frequently utilized in the literature. However, their validity in the case of extreme surface-to-volume ratios remains questionable. Classical finite element method can partially be used to address these deficiencies. On the other hand, molecular dynamics provide accurate results, while nanowire geometries studied with this computationally demanding technique usually remain confined to dimensions below those of practical interest. To address these issues, a benchmarking study among analytical and numerical techniques is carried out, where Surface Cauchy-Born theory serves as the reference. Using gold nanowires with different dimensions and boundary conditions, it is observed that analytical models are applicable within a length-to-thickness ratio range of 7-11 in the fixed-fixed configuration, whereas they can be used safely

within a length-to-thickness ratio range of less than 25 in the fixed-free configuration. Deviations as high as 50% are encountered for length-to-thickness ratios exceeding 11 for both the analytical approach and the classical finite element method in the fixed-fixed structure. The deviations are quantitatively linked to the dominance of the surface effect through the use of the Surface Cauchy-Born model. For length-to-thickness ratios less than 7, the lack of cross-sectional deformations in analytical treatment is also observed to lead to high deviations for the fixed-fixed configuration through the comparison with Higher-Order beam theories. Results are verified with silver nanowires as well. This chapter provides a guideline for selecting the optimum mechanical model given the nanowire resonator dimensions and boundary conditions.

5.2 Introduction

Recent advances in nanotechnology lead to the utilization of nanomechanical devices in ultra-small systems, NEMS, with high performance and low power consumption [Craighead, 2000, Ekinci and Roukes, 2005]. The use of nanomechanical resonators is of specific interest in the field of physical sensors with resolutions reported in femtoNewton [Marago et al., 2008] and yoctogram [Chaste et al., 2012] levels in force and mass sensing, respectively. Similarly, single-molecule sensing is reported in biological sensors [Naik et al., 2009, Eom et al., 2011]. The entire transduction principle is based on the detection of the shift in the resonance frequency as a result of physical or biochemical interactions [Ekinci and Roukes, 2005]. Furthermore, tuning of the resonance frequency is also achieved through the generation of a stiffening mechanism in the resonator by electrostatic [Kozinsky et al., 2006], electrothermal [Jun et al., 2006] or passive [Chiao and Lin, 2004] means. The wealth of such techniques introduced over a relatively short time period indicates the promising nature of the technology, where the availability of suitable frequency response modeling is the key to a successful design.

Nanomechanical resonators take various forms. The resonator geometry of specific interest in this work is the NW. Evanescent mode resonators with the capability

of frequency tuning [Liu et al., 2009], tuning fork resonators [Bartsch et al., 2011] and diaphragm resonators [Li and Lee, 2011] are examples of bulk structures with a high thickness and a low flexural length. On the contrary, NW resonators opened up new possibilities in CMOS integration [Stern et al., 2007], in photonics [He and Yang, 2006] and in piezoresistive transducers [Yan et al., 2009]. State-of-the-art monolithic processes have the capability of providing NWs with a length-to-thickness ratio of up to 150 [Tasdemir et al., 2015]. At this point it becomes critical to judge the suitability of various available mechanical models, as resonator mechanical behavior becomes size-dependent with reduced dimensions. In fact, mechanical characterization of these one-dimensional nanostructures showed a dramatic size dependence specifically in ZnO [Chen et al., 2006], Ag [Jing et al., 2006] and Pb [Cuenot et al., 2004] NWs. Various studies including those by Chen et al. [Wang and Li, 2007], Song [Song et al., 2011] and Wang et al. [Wang and Feng, 2007] reported the contribution of surface elasticity in the NW mechanical response, while the importance of the transverse shear in carbon nanotube (CNT) resonators was studied via analytical formulations [Wang et al., 2006].

Various mechanical models are utilized for NW resonators. The most straightforward means for the modeling of the frequency response is a simple Euler-Bernoulli (EB) beam theory, where the transverse motion of the resonator cross-section is taken into account. Effects due to shear and rotary inertia can further be included through the Timoshenko (TM) beam theory [Weaver Jr et al., 1990]. One particular instance, where the difference between EB and TM is appreciable, is the modeling of higher-order resonance modes in Au NWs [Olsson et al., 2010]. The discrepancy can be explained based on geometric arguments, where higher-order mode shapes with a larger number of inflection points lead to elevated shear and rotary inertia effects. Although TM formulation effectively captures those effects, the applicability of TM as a function of NW architecture including boundary conditions and aspect ratio remains to be further studied.

The main drawback of TM is the presence of the shear correction factor to ac-

count for the inconsistency in the shear stress distribution over the NW cross-section [Kaneko, 1975]. Several methods are proposed for the estimation of the shear correction factor. For example, Cowper [Cowper, 1966] proposes a shear coefficient analysis based on the three-dimensional elasticity, whereas Hutchinson [Hutchinson, 2001] uses the Hellinger-Reissner variational principle. Analytical formulations based on TM shear correction factors cannot be achieved in complicated cross-sections and boundary conditions. Therefore, numerical treatments based on these theories are proposed to reduce computational complexity [Hughes et al., 1977]. In contrast to the shear correction factor in TM, higher-order beam (HOB) theories include the shear strain distribution over the beam cross-section as exhibited both by analytical [Kant and Gupta, 1988] and numerical [Heyliger and Reddy, 1988] approaches and thereby eliminate the shear correction factor.

Neglecting some components of NW deformation is not the only deficiency in the analytical treatment. Surface effects become appreciable in nanoscale structures [Cammarata, 1994]. To further introduce the surface effect, Young-Laplace equation is used in EB and TM beam models. Hence, surface elasticity is implemented into the system in the form of a thin layer on the surface with its own set of elastic properties. The effective flexural rigidity of the NW resonator is then derived based on this bi-layer architecture [Wang and Li, 2007, Wang and Feng, 2007, Olsson and Park, 2012].

Finite Element Method (FEM) can be used as a numerical tool to include all components of deformation. Resonance frequency of the continuum body can be derived based on the solution of the eigenproblem for the discretized continuum body by utilizing stiffness and mass matrices [Bathe, 2006]. The continuum body is considered as homogeneous with averaged, uniform mechanical and physical properties. Recently, the quasicontinuum method is developed to include non-homogeneities in a continuum system. This allows the derivation of the constitutive response based on the interatomic potentials. Based on the discretization of the system, local calculation represents homogeneous deformation in a defect-free crystal and non-local formulation

captures highly energetic regions in crystal defects [Tadmor et al., 1996b].

Recently, SCB method based on the quasicontinuum modeling is developed to implement the surface energy in the mechanical modeling of nanoscale materials. In this numerical method, strain energy density of the system is divided into the surface and bulk components. The fact that surface atoms have fewer nearest neighbors causes an intrinsic surface stress in nanostructures. Atoms with dangling bonds on the surface are thought to be the reason for the alteration of the resonance frequency of some metal [Park and Klein, 2008b] and silicon NWs [Park, 2008]. Molecular Dynamics (MD) constitutes the other extreme, where heterogeneous regions such as surface [Branício and Rino, 2000], crystal reorientation [Park et al., 2005] and atomic imperfections [Kang and Cai, 2010] can be included in mechanical calculations. However, in regard to the geometry and thermodynamics of the NW resonator, it necessitates significant computational resources and therefore has severe limitations regarding NW dimensions.

In summary, a number of modeling efforts on the mechanical behavior of nanomechanical resonators have been reported, where the main motivation is to achieve the highest possible accuracy with manageable computational resources and time [Wang and Li, 2007], [Song et al., 2011], [Wang and Feng, 2007], [Wang et al., 2006], [Weaver Jr et al., 1990], [Bathe, 2006], [Tadmor et al., 1996b], [Park and Klein, 2008b], [Park, 2008]. Selection of the optimum modeling approach is a challenging task. While analytical techniques necessitate the minimum amount of computational requirements, their applicability in extreme resonator geometries remains rather limited. On the other hand, one can achieve the highest accuracy through atomistic formulation, while such studies request a significant computational time. Hence, a comparative study is needed to provide a guideline for assessing the zones of validity for such a wide variety of modeling approaches. In this chapter, limitations in analytical and numerical tools in the frequency response modeling are investigated taking a number of resonator geometries and boundary conditions into account. Au and –to some extent –Ag NWs with $< 100 >$ orientation are used as

models.

In the remainder of this chapter, major analytical (EB and TM) and numerical (FEM and SCB) tools are considered for the mechanical analysis of NW resonators. After introducing the framework, the influences of transverse shear, rotary inertia and surface energy on the frequency response are investigated as a function of resonator characteristics including cross-sectional area, length and surface area-to-volume ratio. Under this set of conditions, limits of the zones of validity of the various models of interest are quantified. The chapter is concluded with a guideline for selecting the optimum engineering formulation in each geometrical domain based on a balance between accuracy and computational effort.

5.3 Formulation

5.3.1 Analytical Models

EB theory is based on the resonator translational motion in the thickness direction, where rotational and shear effects are neglected, and this transverse deflection is assumed to be small [Weaver Jr et al., 1990]. The model is frequently used in the literature due to its simplicity. The motion in the transverse direction, w, as a function of the position, x,(figure5.1) and time, t, can be expressed as

$$EI\frac{\partial^4 w}{\partial x^4} + \rho A\frac{\partial^2 w}{\partial t^2} = 0 \tag{5.1}$$

where $E, I, \rho \; and \; A$ are the modulus of elasticity, the moment of inertia, the density and the cross-sectional area, respectively. Solution of equation5.1 is based on the separation of variables with $w(x,t) = X(x)T(t)$. The shape function of the n^{th} vibrational mode is computed as a function of the boundary conditions. Once the eigenvalue for the shape function is found, vibration frequency is determined accordingly [Weaver Jr et al., 1990].

The above approach can be improved by including rotational and transverse shear effects based on TM beam theory. The equation of motion is then given by

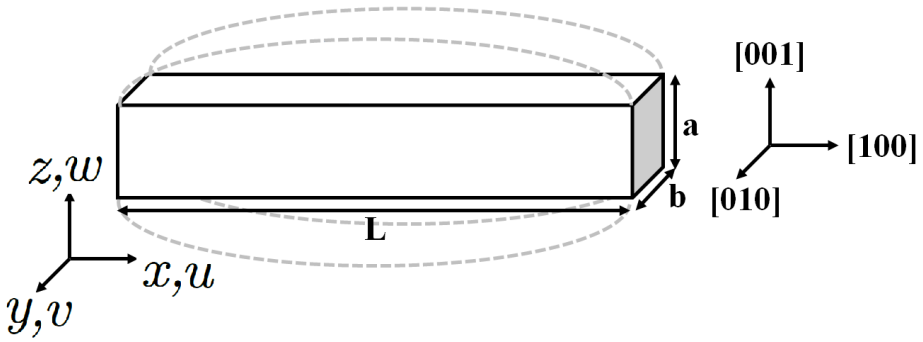


Figure 5.1: NW geometry considered for the flexural resonator with displacements u, v and w in x, y and z directions, respectively.

$$EI\frac{\partial^4 w}{\partial x^4} + \rho A\frac{\partial^2 w}{\partial t^2} - \rho I(1 + \frac{E}{k'G})\frac{\partial^4 w}{\partial x^4} + \frac{\rho^2 I}{k'G}\frac{\partial^4 w}{\partial t^4} = 0 \tag{5.2}$$

where the additional parameters, $k' and\ G$, represent Timoshenko shear coefficient (depending on the shape of the beam cross-section) and shear modulus, respectively [Weaver Jr et al., 1990]. The shear coefficient, k', is introduced to compensate shear stress non-uniformity over the cross-section. Despite various numerical and experimental attempts to evaluate this parameter, Timoshenko estimation [Weaver Jr et al., 1990] is commonly used for beam deformation problems. In this study, conventional Timoshenko′s estimation is employed. By utilizing the separation of variables, the general form of the shape function of the n^{th}vibrational mode can be determined. The solution of the governing equation for the eigenvalue similarly leads to the derivation of the resonance frequency for the specific mode.

5.3.2 Numerical Models

In FEM, elastic modulus and mass density are employed to determine stiffness matrix (K) and mass matrix (M), respectively. The shape function and the strain displacement matrix capture deformation of the beam in all directions. K and M matrices are implemented in the generalized eigenproblem (equation 5.3) to derive the resonance frequency, $f = \omega/2\pi$, [Bathe, 2006].

$$K - \omega^2 M = 0 \tag{5.3}$$

In this technique continuum properties are usually employed and the resonance frequency is thus obtained. However, one can extract the constitutive response from the interatomic potentials as well . This forms the basis of the Cauchy-Born hypothesis [Tadmor et al., 1996b, Park and Klein, 2008b]. In this approach, the strain energy density, $\varphi(C)$, is expressed as a function of the interatomic potential, U, for deformed bond length via continuum quantities such as the right stretch tensor, C. This work utilizes interatomic potentials as proposed by Embedded Atomic Method (EAM) [Foiles et al., 1986]. EAM is defined in a form of traction between embedding energy, F_m, as a function of electron density, $\overline{\rho_m}$,derived from Hartree-Fock calculations and electrostatic energy, ϕ_{mn}, of cores. Strain energy density for EAM interatomic potential can be expressed as

$$\varphi(C) = \frac{1}{2\Omega_0} \sum_{m=1}^{nb} \{F_m(\overline{\rho_m}) + \Phi_m\} \tag{5.4}$$

$$\Phi_m = \frac{1}{2} \sum_{n \neq m}^{nb} \phi_{mn}(r_{mn}(C)) \tag{5.5}$$

$$\overline{\rho_m} = \sum_{n \neq m}^{nb} \rho_n(r_{mn}(C)) \tag{5.6}$$

where, nb is the total number of bonds of a fully coordinated atom in bulk, Ω_0 is atomic volume in undeformed body, ρ_n is the contribution of atom n into the electron density of atom m and r_{mn} is deformed bond length between atoms m and n. The material tangent modulus, D, is determined as

$$D = 4\frac{\partial^2 \varphi}{\partial C_{ij} \partial C_{kl}} \tag{5.7}$$

For nanoscale objects with a high surface area, the surface energy will become important and contribute significantly to the total energy. At this point, the total energy of the continuum body can be expressed in bulk and surface energy density terms. Surface energy density, $\gamma(C)$, is calculated the same way as its bulk counterpart, while the summation on the surface quadrature point has fewer bonding than the bulk. This difference in atomic arrangement on the surface causes a 3×3 stress tensor with normal components. This allows surface relaxation due to the lack of bonding for the atoms at the surface. For these non-bulk layers, the surface strain energy density based on the Surface Cauchy-Born (SCB) method can be written as

$$\gamma(C) = \frac{1}{2\Gamma_0} \sum_{n \neq m}^{nbs} U(r_{mn}(C)) \tag{5.8}$$

where nbs represents the number of bonds for an atom on the surface and Γ_0 is atomic area in undeformed surface. The total potential energy for the continuum system subjected to a prescribed traction, T, can be written in a discretized form based on the nodal displacement,u_i, number of elements,N_e, and number of nodes, N_n, as

$$\Psi(\{u_i\}) = \sum_{e=1}^{N_e} [\int \varphi(C) d\Omega + \int \gamma(C) d\Gamma] - \sum_{a=1}^{N_n} [(T.u_a) N_a] dS_0 \tag{5.9}$$

Additional surface energy in equation5.9 leads to the incorporation of the surface effect in the stiffness matrix, K. The stiffness matrix with surface energy can be extracted by minimizing the total potential energy. Resonance frequency is then derived by solving the associated eigenproblem.

5.4 Case Studies for Nanowire Resonators

Having outlined the techniques to be utilized in the modeling of the frequency response, we next introduce the specifics of the NW resonators. All numerical examples

are performed on single-crystalline gold nanowires with $< 100 >$ longitudinal orientation with {100} transverse surfaces as illustrated in figure5.1. EB, TM, FEM and SCB models are utilized under fixed-fixed and fixed-free boundary conditions (BCs). Four different NW architectures are taken into account in this work, which consider NWs with square constant cross-sectional area (SCSA), rectangular constant cross-sectional area (RCSA), constant length (CL) and constant surface area-to-volume ratio (CSAV) as summarized in Table5.1. This choice facilitates the study of flexural deformation in addition to the effects of cross-sectional dimensions and surface-to-volume ratio through covering all relevant geometrical parameters. Length, L, and thickness, a, are the main geometrical parameters that appear in the analytical treatment [Weaver Jr et al., 1990]. Hence, length-to-thickness ratio, L/a, used as the NW aspect ratio (AR) in this work will be considered as the independent parameter to evaluate the evolution of the resonance frequency.

As explained above, SCB is known as an alternative to MD with a good accuracy for the prediction of the mechanical behavior, as SCB accounts for the surface energy [Park and Klein, 2008b, Esfahani et al., 2016a]. Therefore, SCB will be considered as the reference technique of this work to normalize the results of other techniques with f_{SCB} referring to the fundamental frequency predicted by SCB.

Modulus of elasticity, shear modulus, mass density and Timoshenko shear coefficient are taken as 35 GPa, 12 GPa, 19300 kg/m^3 and 5/6, respectively [Weaver Jr et al., 1990], [Foiles et al., 1986]. Numerical calculations are conducted based on the EAM interatomic potentials for gold single crystals using the parameters defined by Foiles et al. [Foiles et al., 1986] to derive bulk and surface strain energy densities. NWs with four non-bulk layers in SCB models are initially out of equilibrium due to the presence of the surface stresses. The minimum energy configuration is obtained while accounting for the surface stresses. Finite element discretization is realized based on the hexahedral element with 5000 to 30000 nodes. The eigenvalue problem (equation5.3) is solved by utilizing the Krylov-Schur method based on the RayleighRitz approach. All resonance frequency reported in this work is

Table 5.1: Summary of geometries considered (All dimensions are $L \times b \times a$ in (nm)).

SCSA	RCSA	CL	CSAV
$30 \times 10 \times 10$	$30 \times 15 \times 10$	$50 \times 6 \times 10$	$30 \times 10 \times 10$
$50 \times 10 \times 10$	$50 \times 15 \times 10$	$50 \times 8 \times 10$	$47.1 \times 9.42 \times 9.42$
$70 \times 10 \times 10$	$70 \times 15 \times 10$	$50 \times 12 \times 10$	$64.3 \times 9.18 \times 9.18$
$90 \times 10 \times 10$	$90 \times 15 \times 10$	$50 \times 15 \times 10$	$81.4 \times 9.04 \times 9.04$
$110 \times 10 \times 10$	$110 \times 15 \times 10$	$50 \times 18 \times 10$	$98.5 \times 8.96 \times 8.96$
$130 \times 10 \times 10$	$130 \times 15 \times 10$	$50 \times 24 \times 10$	$115.7 \times 8.9 \times 8.9$
$150 \times 10 \times 10$	$150 \times 15 \times 10$	$50 \times 30 \times 10$	$132.8 \times 8.85 \times 8.85$
$170 \times 10 \times 10$	$170 \times 15 \times 10$		$150 \times 8.82 \times 8.82$
$190 \times 10 \times 10$	$190 \times 15 \times 10$		$167.1 \times 8.79 \times 8.79$
$210 \times 10 \times 10$	$210 \times 15 \times 10$		$184.2 \times 8.77 \times 8.77$
$230 \times 10 \times 10$	$230 \times 15 \times 10$		$201.4 \times 8.75 \times 8.75$
$250 \times 10 \times 10$	$250 \times 15 \times 10$		

the fundamental frequency, the bending mode of deformation in thickness direction.

5.5 Results and Discussion

figure5.2 presents the behavior of the SCSA architecture for fixed-fixed (left) and fixed-free (right) BCs. Normalized fundamental resonance frequencies, f/f_{SCB}, are plotted as a function of AR in both cases. Deviations from the reference are observed to be dramatically boundary-condition-dependent. Normalized frequencies change between 0.6 and 1.6 for the fixed-fixed BC, while changes in normalized frequencies are relatively negligible (less than 10%) for the fixed-free BC, i.e. cantilever configuration. A deviation of less than 10% is considered as a threshold for the loss of accuracy in this work. According to this criterion, all techniques work reasonably well for ARs up to 25 with the fixed-free BC, while three zones are identified for the fixed-fixed BC:

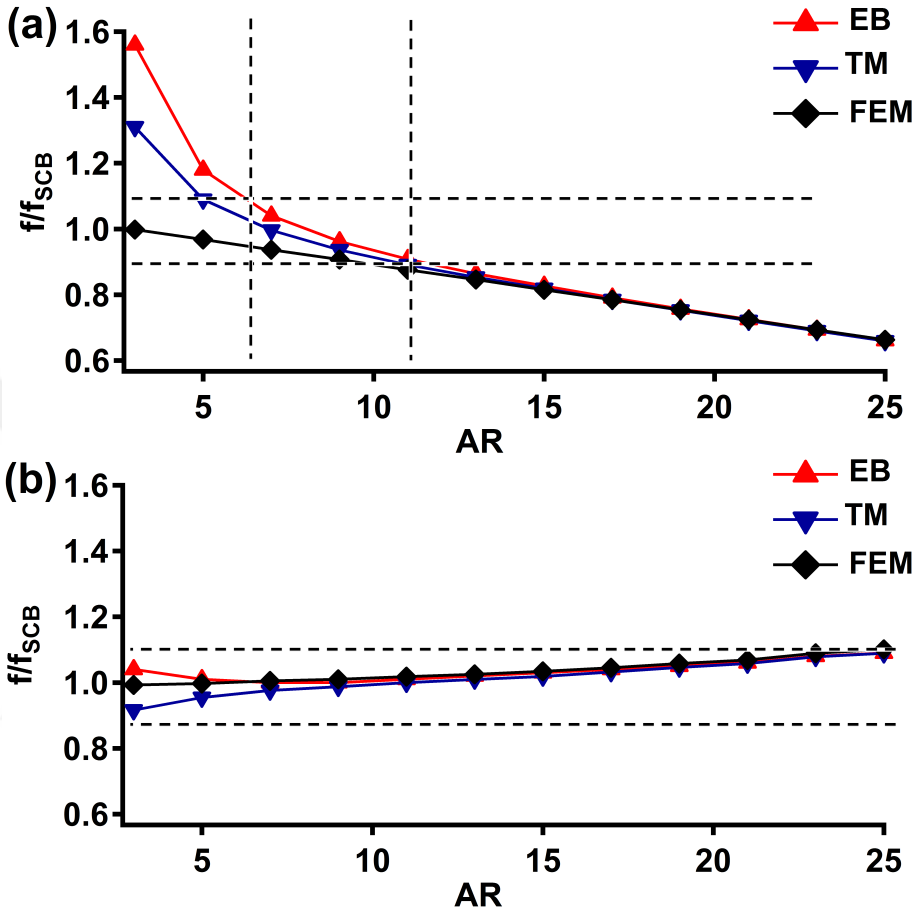


Figure 5.2: Fundamental resonance frequency as a function of AR in EB, TM and FEM methods for (a) fixed-fixed and (b) fixed-free BCs for SCSA.

- Zone 1: A low-AR beam, less than 7, where analytical formulations provide a dramatic over-prediction in frequency response modeling.

- Zone 2: Good correspondence between analytical and numerical calculations with moderate ARs between 7 and 11.

- Zone 3: A slender NW with high AR, more than 11, where all techniques converge but underestimate the frequency due to the increased contribution of surface energy.

An overestimation in the analytical prediction for AR less than 7 (Zone 1) is

shown for the fixed-fixed BC, where the resonance frequency predicted by EB method increases to more than 150% of the SCB for AR = 3. An underestimation in all three methods for aspect ratios higher than 11 (Zone 3) can be observed for the fixed-fixed BC, where the resonance frequency predicted by all three methods reduces to less than 70% of the SCB value for AR = 25. Neglecting transverse shear and rotary inertia in analytical formulations appears to be justified in the cantilever configuration, as no such zones can be observed for the fixed-free BC in figure5.2. Gradual overestimation in all three methods for slender NWs is evident, where a deviation exceeding 10% is recorded only for ARs beyond 25.

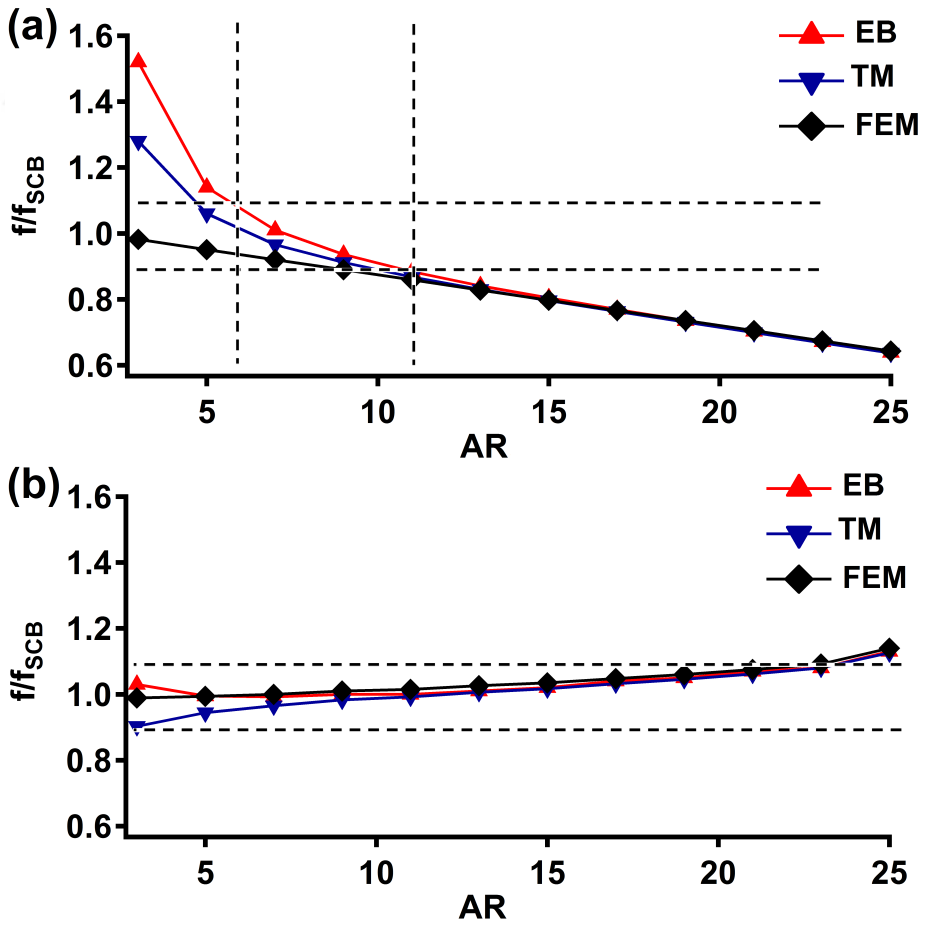


Figure 5.3: Fundamental resonance frequency as a function of AR in EB, TM and FEM methods for (a) fixed-fixed and (b) fixed-free BCs for RCSA.

In-plane dimension, b, describing the NW width in figure5.1 enters the analytical formulation both through the cross-sectional area and the moment of inertia (equation5.1 and 5.2). The influence of width on shear, rotary inertia and cross-sectional deformation is the subject of controversy [Kaneko, 1975, Cowper, 1966]. The effect of this in-plane dimension is investigated through RCSA geometry. Fundamental resonance frequencies for RCSA geometries as a function of AR are shown in figure5.3. They exhibit the same trend as SCSA. In the case of the fixed-fixed BC, three distinct zones are obtained including overestimation in analytical formulations, proper conformity in all calculations and advent of surface energy effects, while the fixed-free architecture represents only surface effects in slender NWs.

To further clarify the influence of the in-plane dimension on the accuracy of analytical formulations for the fixed-fixed BC, the case of CL of Table5.1 is considered with a constant AR of 5 (Zone 1). Resulting resonance frequencies by EB and TM methods as a function of width-to-thickness ratio, b/a, for the fixed-fixed BC are presented in figure5.4. Normalized frequencies change between 1.18 and 1.23 for EB, while TM provides a better approximation and delivers a variation between 1.09 and 1.14. Considering constant shear strain in TM leads to more reliable results in this geometrical domain. Results show an insignificant effect, less than 5%, of the in-plane dimension on the over-prediction exhibited by analytical calculations. This further verifies that variations in the in-plane dimension have a negligible effect on shear strain and rotary inertia. Despite the numerous studies [Kaneko, 1975, Cowper, 1966, Hutchinson, 2001] to express flexural deformation as a function of the cross-sectional area, figure5.4 demonstrates that the cross-sectional area itself is not a proper choice for representing shear and rotary inertia effects in analytical calculations.

Let us now focus specifically on the choice of an appropriate criterion for predicting the dominance of surface effects. Zone 3 in fixed-fixed NWs (figure5.2 and figure5.3) hints at the importance of the surface energy in NWs with a high surface area. Similarly, fixed-free NWs with extreme AR encounter surface stress effects. Dangling bonds on the surface of the NW resonator provide an intrinsic unbalanced

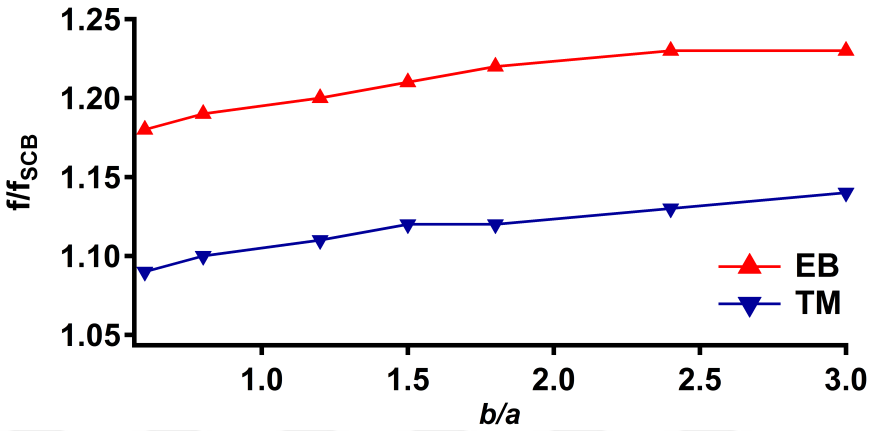


Figure 5.4: Fundamental resonance frequency as a function of width-to-thickness ratio in EB and TM methods for fixed-fixed BC for CL.

force causing surface stress. This surface stress is responsible for contraction in metal NWs [Park and Klein, 2008b] and expansion in silicon NWs [Park, 2008]. Surface energy remains unaccounted for in analytical methods and classical FEM. This contribution is considered in the SCB method in this work, which serves as the reference against which all other techniques are checked. Surface energy becomes significant in Zone 3, where a tensile surface stress exists for the fixed-fixed BC. The lack of surface energy in the analytical treatment and classical FEM leads to an underestimation in the frequency. Compressive strain in the fixed-free BC caused by surface stress [Park and Klein, 2008b] leads to an overestimation in all three methods (Zone 3 in figure5.2 and 5.3). This over-prediction exhibited by analytical and FEM calculations becomes significant only for AR in excess of 25 for the fixed-free BC.

Surface effect in slender NWs can be captured only with SCB or atomistic calculations. Proposed analytical calculations based on the Young-Laplace method can be utilized to implement surface energy in mechanical response modeling [Wang and Feng, 2007, Wang and Feng, 2009, He and Lilley, 2008b]. Utilizing effective bending moment and surface effect factor into the analytical calculations can reduce resonance frequency deviation in Au NWs from 60% to 15% for AR=25 [He and Lilley, 2008b]. In contrast, fitting error in the effective flexural rigidity

[Wang and Li, 2007, Wang and Feng, 2007, He and Lilley, 2008b] and uncertainties in bulk and surface material properties [Wang and Feng, 2007, He and Lilley, 2008b] are the main sources of deviation for these methods.

The surface-to-volume ratio is a critical feature in a variety of studies on nanoscale mechanical response, where the surface effect is dominant [Roukes, 2001]. In the present study, AR is highlighted in the demonstration of the surface effect as shown by the case of CSAV of Table 1. Here the surface area-to-volume ratio is kept constant over a variety of ARs. Results are given in figure5.5 for both BCs. They exhibit a similar trend in comparison to SCSA and RSCA of Figs. 5.2 and 5.3, respectively. Three zones for the fixed-fixed BC exist, while the increasing surface effect in slender NWs is also evident for the fixed-free BC. Results indicate the dominant surface effect even though the surface area-to-volume ratio is kept constant.

Furthermore, FEM predictions for SCSA and RCSA are plotted in figure5.6 as a function of different surface area-to-volume ratios in Zone 3. The specific configurations are obtained by increasing the length from 30 nm to 250 nm whereas the cross-sectional area is kept 100 nm^2 and 150 nm^2 for SCSA and RCSA, respectively. The outcome is interesting. With increasing surface area-to-volume ratio the surface effect diminishes. For example, in the case of SCSA, the normalized frequency of about 66% obtained for a surface area-to-volume ratio of 0.408 is observed to increase to about 88%, when the surface area-to-volume ratio is increased to 0.418. A similar reduction in surface effect is evident in RCSA as well. Previous experimental [Verbridge et al., 2007] and numerical [Park and Klein, 2008b] studies also reported changes in the resonance frequency with a constant surface are-to-volume ratio. In parallel, one can argue that the surface stress is independent from surface area-to-volume ratio. Hence, figure5.5 and 5.6 clearly demonstrate that AR is a more applicable criterion in predicting the dominance of surface effects in NW mechanical behavior compared to the surface area-to-volume ratio.

After having clarified the extent of the surface effect we can now turn our attention to the discrepancy between analytical and numerical methods for low AR (Zone

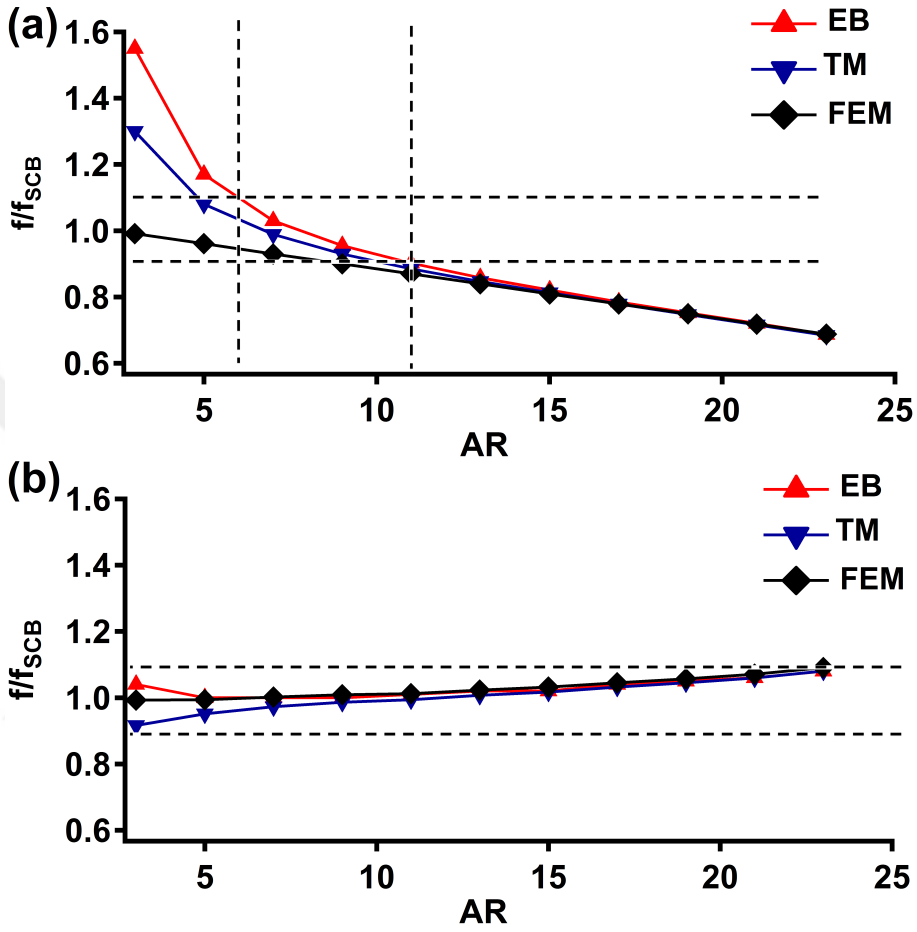


Figure 5.5: Fundamental resonance frequency as a function of aspect ratio in EB, TM and FEM methods for (a) fixed-fixed and (b) fixed-free boundary conditions for CSAV.

1). Analytical formulations are based on the translational motion, w, in the flexural direction (z axis in figure5.1). Increasing shear and rotary inertia effects with the fixed-fixed BC leads to significant displacements in longitudinal and in-plane directions along x and y axes in figure5.1, respectively. These displacements cause a dramatic overestimation in the analytical calculations in Zone 1. Convergence between numerical and analytical calculations is only obtained in Zone 2 ($7 < AR < 11$). On the other hand, the free end in the cantilever configuration prevents deformations in directions other than the flexural direction. Hence, pure translational motion and convergence between numerical and analytical methods in the fixed-free configuration

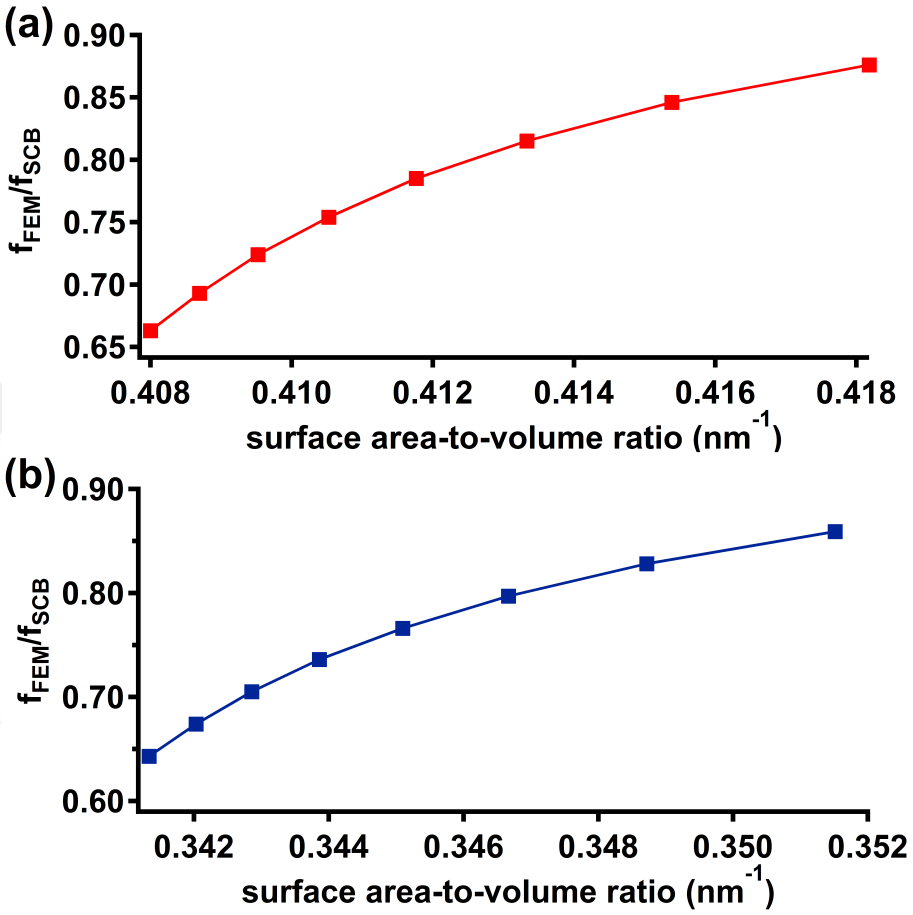


Figure 5.6: Fundamental resonance frequency as a function of surface area-to-volume ratio with FEM for (a) SCSA and (b) RCSA.

can be seen for almost all geometries.

To further demonstrate the importance of the longitudinal displacement, u, on the flexural rigidity in Zone 1, quasistatic stiffnesses in EB and TM methods are compared with those obtained via HOB theory for the case of SCSA geometries. Bickford formulation in HOB [Reddy et al., 1997] is utilized with quadratic variation of the transverse shear strain. figure5.7 depicts stiffness values obtained through EB and TM methods normalized by those of the HOB method, K/K_{HOB}, for both fixed-fixed and fixed-free BCs. The deviation of both EB and TM methods from HOB theory demonstrates the dependence on NW geometry and BCs. Normalized stiffness changes between 1 to 3 for the fixed-fixed BC, while variation for the fixed-free BC

remains confined to within 1 to 1.3. EB and TM methods extract the same stiffness as HOB theory for AR values exceeding 15.

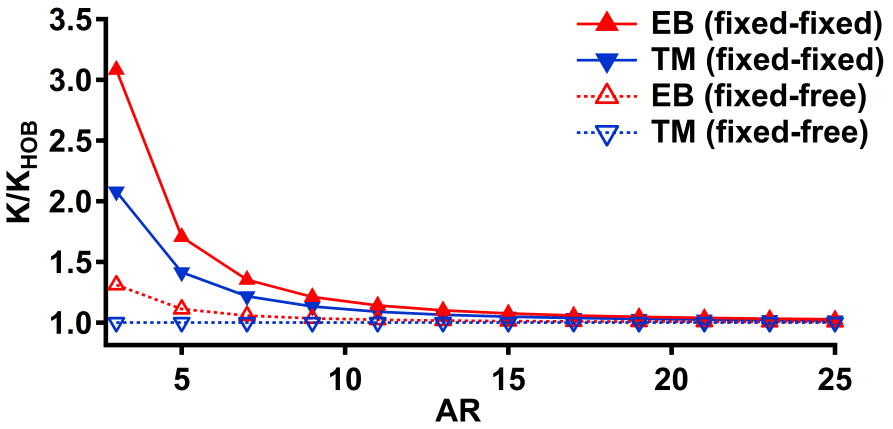


Figure 5.7: Quasistatic stiffness as a function of aspect ratio in EB and TM methods for fixed-fixed and fixed-free boundary conditions for SCSA geometries.

Over-prediction of stiffness in EB and TM theories for low AR (Zone 1) can be traced back to neglecting shear deformation in the NW cross-section for the fixed-fixed BC, while these deformations are relatively insignificant in the fixed-free configuration. TM theory retains all assumptions of the EB method except for maintaining cross-sections normal to the longitudinal axis in flexural deformation. This assumption predicts a constant shear strain across the thickness [Weaver Jr et al., 1990], whereas a parabolic variation in shear strain exists over the cross-section in reality [Heyliger and Reddy, 1988, Reddy et al., 1997]. Hence, TM theory overestimates mechanical stiffness, which is the main reason of the high deviation in Zone 1 for the fixed-fixed BC. Since shear effects are eliminated in EB theory, a higher amount of deviation as a result of overestimation in mechanical stiffness is identified (figure5.2, 5.3 and 5.4). The importance of transverse shear and rotary inertia effects hints at the relative weakness of analytical formulations for AR less than 7 with the fixed-fixed BC. Classical finite element method can be utilized as an alternative tool with less computational effort than SCB. Utilizing HOB theories in Zone 1 is a challenging task due to the geometrical dependency in the primitive strain definition and a

comparable computational effort with FEM. Convergence of analytical and numerical calculation is a strong justification for the selection of analytical methods in Zone 2 as the low-cost technique with an acceptable accuracy. As shear and rotary inertia effects are negligible for the fixed-free BC, EB theory can directly be utilized in the frequency response modeling of cantilevers with AR less than 25.

Finally, the effect of material properties is studied to clarify limitations of analytical and numerical tools for different face-centered crystals. To demonstrate the effect of the crystalline material, the fundamental resonance frequency of Ag NWs for SCSA geometries for fixed-fixed and fixed-free BCs is calculated. Modulus of elasticity, shear modulus, mass density and Timoshenko shear coefficient are taken as 89 GPa, 32.5 GPa, 10500 kg/m^3 and 5/6, respectively [Weaver Jr et al., 1990, Foiles et al., 1986]. Numerical work is performed according to the EAM interatomic potentials for Ag single crystals using the parameters defined by Foiles et al. [Foiles et al., 1986] to derive bulk and surface strain energy densities.

The resulting behavior is provided in figure5.8 for a Ag single-crystal NW with $< 100 >$ longitudinal orientation with $\{100\}$ transverse surfaces. SCSA configuration is used with fixed-fixed (left) and fixed-free (right) BCs. A similar trend to that of Au NWs given previously in figure5.2 is observed for Ag as well. Three distinct zones are obtained for the fixed-fixed BC. The effects of neglected transverse shear strain for low AR NWs (Zone 1) and surface energy for slender NWs (Zone 3) are once again evident. EB formulation predicts resonance frequency more than 165% of the SCB for AR = 3, while underestimation in all three methods for AR higher than 17 can be observed. The lack of surface energy in all three methods leads to an underestimation of the resonance frequency beyond 80% for AR = 25 in the fixed-fixed configuration. Surface effect is found to be negligible for AR less than 25 for the fixed-free BC.

Although Ag NWs present the same trend as Au NWs, identified zones end up having slightly different AR limits. For example, a comparison of the limits of Zone 1 in Figs. 2 and 8 highlights the dominant shear strain effect in the analytical treatment of Ag. A higher shear effect in Ag is evident from the higher ratio of axial and lateral

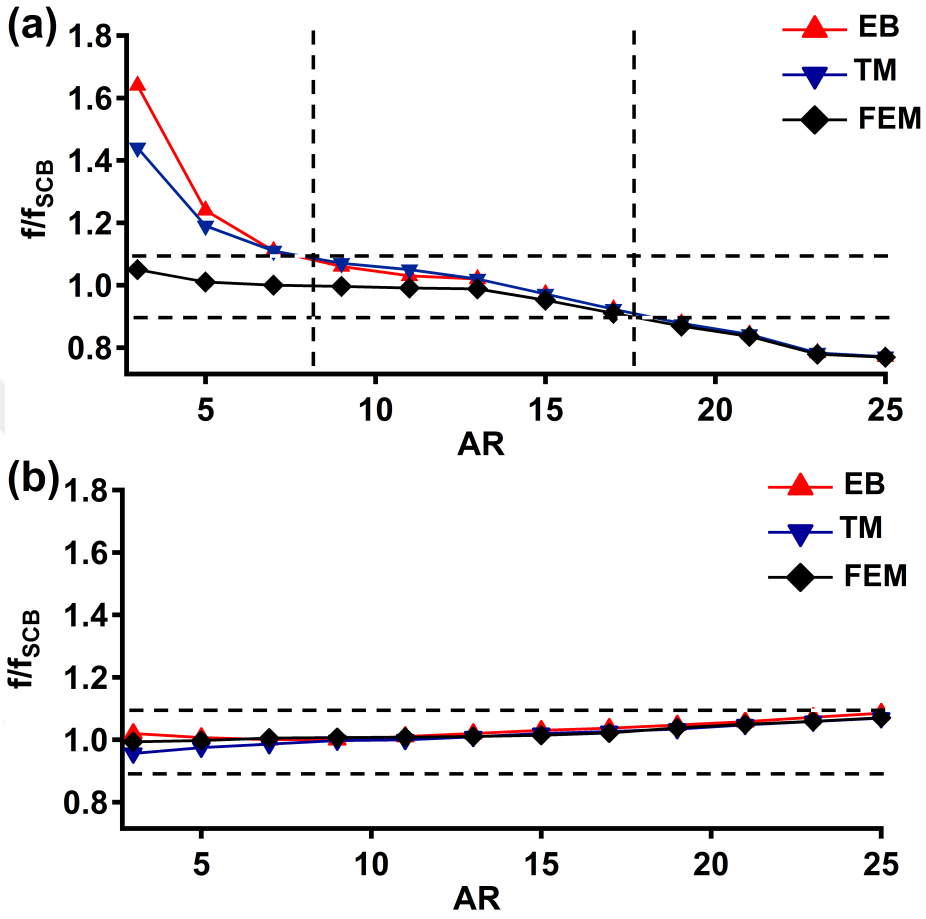


Figure 5.8: Fundamental resonance frequency of Ag NWs as a function of aspect ratio in EB, TM and FEM methods for (a) fixed-fixed and (b) fixed-free boundary conditions for SCSA.

elastic moduli, D_{11}/D_{12} [Foiles et al., 1986]. The influence of surface energy becomes noticeable in Ag NWs only beyond an AR of 17 as opposed to the limiting AR value of 11 in Au. This difference is linked to the embedded energy function, where a higher rate of change of embedded energy in Au crystal surface leads to a higher surface stress [Foiles et al., 1986].

All calculations in this study are kept limited to the fundamental resonance frequency in the flexural mode. Different surface stress behavior for further modes as a function of geometry and BC was previously reported [Park and Klein, 2008b]. This would necessitate a further investigation for the determination of the AR limits

regarding analytical and numerical formulations. For fcc NWs with a longitudinal orientation other than $< 100 >$ the constitutive response and nearest neighbor arrangement on the surface need to be redefined for SCB. This aspect is worth being considered in further studies. Last but not least, recent studies highlight the importance of temperature in the thermomechanical behavior at the nanoscale as well [Esfahani et al., 2016a]. Determination of the zones of validity for different models at finite temperatures is as well the subject of another future work.

5.6 Conclusion

A guideline for selecting the optimum engineering tool for the frequency response modeling of flexural nanowire resonators is introduced. Euler-Bernoulli and Timoshenko beam theories along with classical finite element method and Surface Cauchy-Born theory are considered. Specific zones in terms of NW aspect ratio are determined, where analytical and numerical results are compared to those provided by the Surface Cauchy Born theory. Various resonator properties are considered including the cross-sectional area, length and surface area-to-volume ratio. Based on practical considerations, two boundary conditions, fixed-fixed and fixed-free (cantilever) configurations, are considered. Major outcome of this chapter can be listed as follows:

Fixed-Fixed boundary condition:

- Euler-Bernoulli and Timoshenko beam theories are invalid for aspect ratios less than 7 for gold, and less than 8 for silver. In this particular zone, Finite Element Method is recommended as an efficient tool instead of analytical formulations.

- Considering their low computational requirements, Euler-Bernoulli and Timoshenko beam theories offer reliable results for intermediate aspect ratios between 7 and 11 for gold and between 8 and 17 for silver. At the lower end, Timoshenko theory works better in predicting the frequency response.

- For aspect ratios beyond this intermediate zone, Surface Cauchy-Born theory is

the most effective tool for capturing the surface effect on the frequency response.

Fixed-Free boundary condition:

- Euler-Bernoulli beam theory works well for all aspect ratios less than 25. Although Timoshenko beam theory can be omitted in this zone, caution should be exercised for cross-sections, where the height, a, grows considerably compared to the width, b.

- Surface Cauchy Born theory is recommended for resonator aspect ratios in excess of 25.

Deficiencies in Euler-Bernoulli and Timoshenko beam theories are linked to the simplifying assumptions involved, *i.e.* the elimination of shear stress in Euler-Bernoulli beam theory and the assumption of constant shear strain in Timoshenko beam theory. Despite their low computational cost, employing these two formulations requires a well-defined guideline. Although the quantities reported in this chapter are directly applicable to single-crystalline gold and silver NWs in $< 100 >$ orientation at zero absolute temperature, they can be considered as a guideline for selecting the modeling tool for other similar resonator materials. Poisson′s ratio, shape of the cross-section [Weaver Jr et al., 1990], surface energy [Park and Klein, 2008b] and temperature [Esfahani et al., 2016a] are the main parameters that would cause changes in the transition between zones. Further work is needed to address these effects. The importance of finite temperature is especially important and is recently considered in literature in parallel with the Surface Cauchy-Born theory [Esfahani et al., 2016a].

Chapter 6

THERMO-COUPLED SURFACE CAUCHY-BORN

6.1 Overview

There are remarkable studies geared towards developing thermomechanical analyses of nanowires based on quasiharmonic and Molecular Dynamics simulations. These methods exhibit limited applicability due to the associated computational cost. In this chapter an engineering finite-temperature model based on Surface Cauchy-Born theory is developed, where surface energy is accounted for in the prediction of the thermomechanical response. This is achieved by using a temperature-dependent interatomic potential in the standard Cauchy-Born theory with a surface energy contribution. Simultaneous calculation of thermal and mechanical stresses is achieved by eliminating the diagonalization matrix of entropy in the quasiharmonic system. This leads to a reduction in the degrees of freedom by more than 99% in comparison with equivalent Molecular Dynamics models. For the purpose of validation, results obtained on copper and nickel nanowires through the proposed method are compared with those of the more involved Molecular Dynamics simulations. This comparison verifies the significant reduction in the computational process with an acceptable accuracy. Hence, the proposed method provides a promising engineering tool without compromising the underlying physics of the problem and has potential implications in the effective modeling of the nanoscale thermomechanical behavior.

6.2 Introduction

Nanowires (NWs) have been under intense development in recent years due to their unique mechanical, optical and electrical properties. They are utilized

in various applications including electronics [Sacchetto et al., 2009] and photonics [Yan et al., 2009]. A further emerging field of their application is nanoelectromechanical systems (NEMS), where they are mainly utilized as transducers for high-resolution mass [Hanay et al., 2012] and force sensing [Sage et al., 2015]. Measurements down to yoctogram [Chaste et al., 2012] and femtoNewton [Marago et al., 2008] are reported. Most of these techniques involve the dynamic-mode operation of the NW, where changes in the resonant behavior are monitored as indicators of external mechanical effects [Sadek et al., 2010, Gil-Santos et al., 2010, Yang et al., 2006]. Hence, NWs serve as ultra-small mechanical components, where size reduction proves to be extra advantageous in sensing applications. The main advantages are associated with i) their high frequencies of operation leading to high sensitivities and high resolution, ii) their ability of deterministic integration with higher-order structures such as electrodes, and iii) the ease of their use as transducers, especially through piezoresistivity in Si NWs [Walther et al., 2012, He and Yang, 2006, Sansa et al., 2014, Erdem Alaca, 2009], and stretchable conductors with metal NWs [Xu and Zhu, 2012, Yao and Zhu, 2015].

It is well known that mechanical properties exhibit dramatic size dependence. For example, [Cao and Chen, 2008] reported a significant size dependence of the modulus of elasticity in ZnO NWs [Cao and Chen, 2008]. Similarly, [Cuenot et al., 2004]. showed an increase in the modulus of elasticity in silver and lead NWs in smaller diameters [Cuenot et al., 2004]. Further effects such as phase transformations in gold NWs [Diao et al., 2003] and pseudoelastic behavior in NWs made of shape memory alloys [Park et al., 2005] are linked to the reduction of size. As the mechanical behavior of NWs is core to the operation of the majority of NEMS applications, modeling of their mechanical properties becomes a critical task. It proves to be a challenging task as well, as size reduction leads to the dominance of quantum effects due to the confinement by free surfaces and interfaces [Wang and Herron, 1991]. A key feature of a free surface or an interface is the difference in their atomic arrangement due to the lack of bonding neighbors. This leads to a different set of elastic properties

of surfaces from that of the bulk, where fully coordinated atomic arrangements and balanced forces exist.

A wide range of analytical models for the size-dependent elastic properties at the nanoscale has recently been developed. These models are usually based on enhanced classical continuum mechanics that use a bulk/surface decomposition to study surface effects with varying nanostructure dimensions. For example, Wang [Wang and Feng, 2009] and He [He and Lilley, 2008a] presented the surface effect on bending and resonance frequency of NWs by utilizing a surface layer of finite thickness and the Young-Laplace equation. On the contrary, an extensive range of multiscale modeling studies investigates problems with continuum methods with an atomic-scale resolution. These techniques can generally be referred to as atomistic-based continuum analyses or quasicontinuum methods. In this approach a general continuum finite element formulation is utilized to characterize the mechanical response of a given system. A finite element analysis provides a continuum system with adaptive model refinement to save fully atomistic details and supplies a multi-scale analysis capability by refining the mesh size near lattice defects and highly energetic regions such as stacking faults and dislocations [Tadmor et al., 1996b] and elastic and plastic deformations [Tadmor et al., 1996a] in solids. The main difference of the atomistic-based continuum analyses from classical finite element methods is the derivation of the constitutive response from an atomistic standpoint rather than empirical rules and phenomenological models [Tadmor et al., 1996b].

Recently, [Park et al., 2006] proposed a multiscale Surface Cauchy-Born (SCB) method to capture atomic-scale surface stress effects based on decomposing the potential energy into bulk and surface components, where bulk and surface stresses constitute distinct terms in the variational equation. This decomposition is the basis of capturing surface energy as the size of the continuum body decreases and the surface energy becomes dominant[Park et al., 2006]. This method was successfully utilized to demonstrate size dependence in bending behavior [Yun and Park, 2009] and resonance frequency of metallic [Park and Klein, 2008b] and Si [Park, 2008] NWs due

to the free surface energy. Although the aforementioned atomistic-based continuum analyses can describe phenomena such as size-dependence, surface energy and crystal non-uniformity, their use is confined to cryogenic systems. As classical interatomic potentials such as Lennard-Jones (LJ), Embedded Atom Method (EAM) and Tersoff are defined in static atomistic systems at zero absolute temperature, modeling of the thermomechanical response in nanostructures with atomistic resolution constitutes a novel challenge in engineering applications.

Only recently the temperature-dependent interatomic potential was developed as an efficient molecular calculation technique to model high-temperature behavior [Subramaniyan and Sun, 2008]. For example, in MD simulations, the effect of temperature is accounted for by thermal vibrations of each atom, where the system is permitted to progress dynamically by integrating Newtons equations of motion for each atom over time for the atomic system. [Dupuy et al., 2005] proposed a finite-temperature method by a combination of statistical mechanics and finite element calculations [Dupuy et al., 2005]. [Xiao and Yang, 2006], [Liu and Li, 2007], [Jiang et al., 2005] and [Tang et al., 2006] developed a multiscale Helmholtz free energy method based on the CauchyBorn approximation. In this method, the effect of the finite temperature is accounted for by the local harmonic approximation, which relates the entropy to the vibration frequencies of the system[Xiao and Yang, 2006, Liu and Li, 2007, Jiang et al., 2005, Tang et al., 2006].

The effect of free surface on mechanical properties is one of the most sought-after modeling aspects in NEMS. As NEMS designs and applications are under constant evolution, engineering approaches with straightforward, computationally less demanding numerical techniques relevant to operation conditions such as finite temperatures are highly needed. In this chapter, we present the thermo-coupled surface Cauchy-Born (TSCB) model, a continuum-based theory with multiscale coupling for the thermomechanical analysis of NWs at finite temperatures where surface stress has a significant contribution. Based on the developments of the MD and the Helmholz free energy methods to capture surface effects at finite temperatures, the present

chapter proposes to implement temperature in the definition of the interatomic potential as opposed to using temperature as a kinetic component in entropy calculations from quasiharmonic approximations. This is achieved by utilizing Engineering Molecular Mechanics (EMM) proposed by [Subramaniyan and Sun, 2008] as an alternative molecular simulation tool [Subramaniyan and Sun, 2008] within the SCB method. Compared to MD and quasiharmonic models the proposed method requires less computational power and provides a bridge between fundamental scientific modeling efforts and practical engineering applications without compromising accuracy.

In the remainder of this chapter the Surface Cauchy-Born hypothesis is introduced first, followed by the description of the combination of molecular mechanics with finite element calculations. The results of the finite element simulations are compared with traditional MD calculations for validation. This chapter is concluded by analyzing the accuracy of the proposed method for the prediction of the modulus of elasticity as an essential parameter in mechanical response modeling. Finally, the opposing effects of surface and thermal energies on the mechanical response are demonstrated.

6.3 Methodology

The quasicontinuum method has been developed to investigate the mechanical response of a continuum body with atomic scale interactions. In this approach, a classical continuum finite element formulation is employed to characterize the mechanical response of a given system, where the constitutive response of the system is determined by interatomic calculations. The basic idea is that every point in a continuum corresponds to a very large region on the atomic scale. Thus, the constitutive response at that point may be obtained by deforming the underlying crystal structure by the local strain to obtain the local state of stress. This constitutive response is derived by utilizing ordinary interatomic interactions such as LJ and EAM for metals and Tersoff potential for covalent systems.

Since the quasicontinuum method does not account for the surface energy contribution at the nanoscale, the SCB model was developed by [Park et al., 2006] to

capture surface effects within the framework of the atomic-based continuum analysis. In this method, the energy of the system is divided into bulk and surface components. The interatomic potential can be turned into the Bulk Cauchy-Born approximation by two steps: converting the potential energy into a strain energy density through normalization by the atomic volume,Ω_0, and then deforming the neighbors around each atom homogeneously via continuum mechanics quantities such as the deformation gradient F, or right stretch tensor $C = F^T$ F[Park et al., 2006]. As the result, the strain energy density at finite temperatures, $\varphi(C,T)$, can be expressed as a function of the temperature-related interatomic pair potential, U_T, as

$$\varphi(C,T) = \frac{1}{2\Omega_0}\sum_{m=1}^{nb} U_T(r^m(C),T) \tag{6.1}$$

where nb is the total number of bonds to a representative bulk atoms, Ω_0 is the atomic volume in the reference configuration with undeformed bond vector R^m, and r^m is the deformed bond length at atom m and its neighbors

$$r^m = \sqrt{R^m.CR^m} \tag{6.2}$$

This energy equivalence forms the basis of the traditional CB hypothesis, in which lattice defects are not considered. When the strain energy function at finite temperatures is known, the continuum stress can be derived by differentiating the material strain energy density function with respect to the right stretch tensor, where there is no need to divide the stress into mechanical and thermal portions [Yun and Park, 2008]. The second Piola-Kirchoff stress at finite temperature can be written as

$$S_T = 2\frac{\partial\varphi(C,T)}{\partial C} \tag{6.3}$$

whereas the temperature-related spatial modulus D_T is defined as

$$D_T = 4\frac{\partial^2\varphi(C,T)}{\partial C_{ij}\partial C_{kl}} \tag{6.4}$$

The lack of any decomposition requirement of stress and modulus into their mechanical and thermal components provides a significant advantage in comparison to the

Helmholz free energy methods. All points in the bulk are considered in equilibrium with a fully coordinated atomic structure in the BCB hypothesis and all points on the surface have fewer bonding neighbors that leads to a surface stress. Therefore, the SCB was developed to include surface energy in NWs by capturing surface stress due to the uncoordinated atoms on the surface. The strain energy density of a body can be expressed in bulk and surface terms by decomposing the potential energy into bulk and surface components. The relationship between the continuum strain energy density and the total potential energy of a defect-free system at a finite temperature can thus be expressed as

$$\sum_{m=1}^{n_{atom}} U_T^m(r,T) = \int_{\Pi_0} \varphi(C,T)d\Omega + \int_{\Gamma_0} \gamma(C,T)d\Gamma \tag{6.5}$$

where $\varphi(C,T)$ is the bulk strain energy density integrated over the volume of the body, Π_0, in which all atoms are fully coordinated and $\gamma(C,T)$ is the surface strain energy density, integrated in each non-bulk surface layer of the body, Γ_0, in which the atoms are not coordinated at high temperatures. The strain energy density on the surface at a finite temperature can be written as

$$\gamma(C,T) = \frac{1}{2\Gamma_0} \sum_{m=1}^{nbs} U_T(r^m(C),T) \tag{6.6}$$

where *nbs* is the number of bonds for an atom on the surface. Similar to the bulk continuum thermomechanical stress, the surface Piola-Kirchoff stresses at high temperatures can be defined as

$$\widetilde{S_T} = 2\frac{\partial\gamma(C,T)}{\partial C} \tag{6.7}$$

where the surface stress, $\widetilde{S_T}$, is a 3×3 tensor with normal components which allows surface relaxation as the atoms lying at the surface are not fully coordinated. This stress formulation is different from the conventional definition of a 2×2 surface stress [Shenoy, 2005] which includes only tangential terms. Similarly, the surface spatial modulus,$\widetilde{D_T}$, can be defined as

$$\widetilde{D_T} = 4\frac{\partial^2\gamma(C,T)}{\partial C_{ij}\partial C_{kl}} \tag{6.8}$$

The total potential energy at finite temperature for the continuum body in which the temperature-related strain energy was decomposed into bulk and surface components under an external load $\overline{T}$ can be written as

$$\Psi(u,T) = \int_{\Pi_0} \varphi(C,T)d\Omega + \int_{\Gamma_0} \gamma(C,T)d\Gamma - \int (\overline{T}.u)d\Gamma \tag{6.9}$$

To obtain a suitable form for the finite element calculation, the standard discretization of the displacement field $u(X)$ can be utilized by using shape functions as

$$u(X) = \sum_{I=1}^{nn} N_I(X)u_I \tag{6.10}$$

where N_I represent the shape or interpolation functions, nn are the total number of nodes in the discretized continuum and u_I represent the displacements of node I. Differentiating equation (6.9) with respect to the nodal displacement at the minimum potential energy gives the finite element nodal load balance as

$$\frac{\partial \Psi}{\partial u_I} = \int_{\Pi_0} B^T S_T F^T d\Gamma + \int_{\Gamma_0} B^T \widetilde{S_T} F^T d\Gamma - \int_{\Gamma_T} N_I \overline{T} d\Gamma \tag{6.11}$$

where $B^T = ((\partial N_I)/\partial X)^T$ is the strain displacement matrix. equation (6.11) requires an iterative method to solve the non-linear system of equations to determine the nodal displacements that minimize the energy of the continuum body.

The strain energy density at a finite temperature in the crystal structure can be derived by using EMM, which was developed for temperature-dependent interatomic potentials to analyze static MD at high temperatures. The interatomic potential in MD simulations and the Helmholz free energy are temperature independent, *i.e.* temperature effects are included by allowing the system to evolve dynamically according to the Newtons equation of motion and kinetic energy in entropy calculation, respectively. In the EMM [Subramaniyan and Sun, 2008], the thermal vibration of each atom is replaced with a few parameters in the interatomic potential to capture the global averaged temperature-dependent behavior of the system. It has thus been proposed to use thermal expansion to represent the effect of temperature in materials at

the atomic level. The LJ potential taking the temperature dependence into account can be expressed as

$$U_T(r) = \epsilon_T[(\frac{R_T}{r})^{12} - 2(\frac{R_T}{r})^6] \tag{6.12}$$

where

$$R_T = (1 + \alpha T)R_0 \tag{6.13}$$

$$\epsilon_T = -[U_0(R_T) + k_B T] \tag{6.14}$$

in which k_B is the Boltzmann constant, R_T and ϵ_T are the LJ parameters at temperature T, and U_T is the temperature-dependent interatomic potential. R_0 and α are interatomic distance at 0K and thermal expansion coefficient, respectively.

In the present work, the temperature-dependent interatomic potential is utilized to study surface energy at finite temperatures, where the TSCB method is developed as an alternative to the MD and quasiharmonic models for crystalline solids at finite temperatures. Simultaneous derivation of mechanical and thermal stresses makes the technique easier to implement and leads to a significant increase in efficiency. For this purpose we propose utilizing the temperature-dependent interatomic potential turning the quasicontinuum method more practical for engineering applications. To evaluate the accuracy of the proposed method, a numerical study is conducted on copper and nickel NWs, where interactions in an FCC crystal are modeled using temperature-dependent LJ potentials and results are compared with those of MD simulations.

6.4 Numerical Model

All numerical examples are presented for the FCC single-crystalline Cu and Ni NWs oriented along the $< 100 >$ direction with $\{100\}$ surfaces. The NWs have a square cross-section of 30×30 unit cells and a length of 100 unit cells. The atomic interactions are modeled using temperature-dependent LJ interatomic potentials [Subramaniyan and Sun, 2008] with a truncation after the third shell of the nearest

neighbors. This approach leads to two non-bulk layers of atoms at the surfaces as illustrated in figure6.1.

All SCB calculations utilize regular eight-node hexahedral elements. The temperature-dependent interatomic potential at different temperatures is considered with the following parameters [Subramaniyan and Sun, 2008] for copper ($R_0 = 2.6\mathring{A}$; $\epsilon_0 = 0.167eV$ and $\alpha = 17 \times 10^{-6}K^{-1}$)and for nickel($R_0 = 2.258\mathring{A}$; $\epsilon_0 = 0.195eV$ and $\alpha = 13 \times 10^{-6}K^{-1}$) .

NWs are defined in the form of cantilevers, fixed at one end and free to move at the other one for surface stress relaxation (figure6.1). In the first step, no external loads are applied and all deformations obtained are due to the thermomechanical surface stresses.

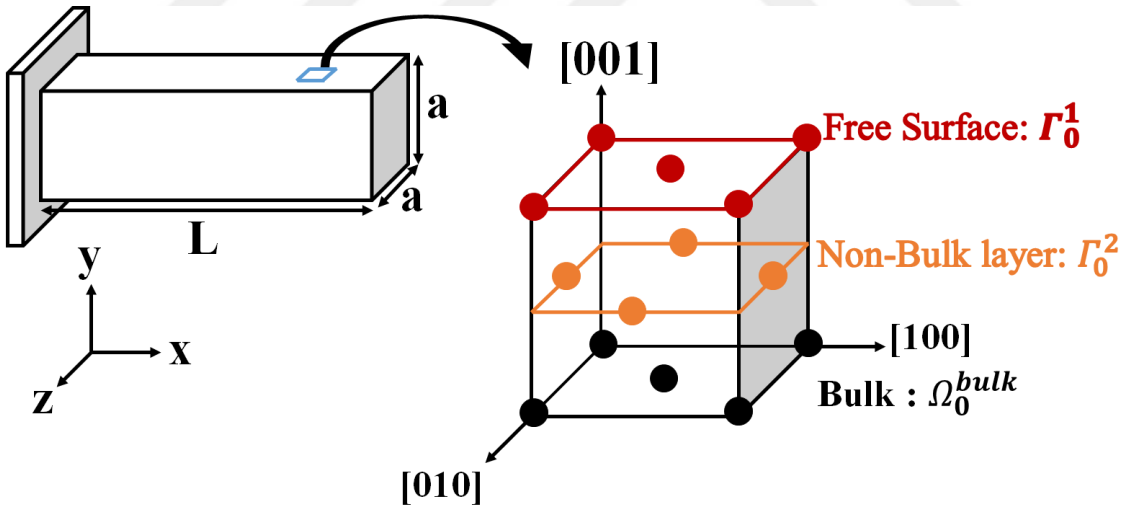


Figure 6.1: NW geometry considered for surface stress relaxation (Left) and Bulk and Non-bulk layers in crystal orientation (Right).

In the second step, uniaxial tension is applied along the $< 100 >$ direction of the NWs up to a strain of 0.2% at different temperatures. The modulus of elasticity is extracted from the resulting stress-strain curves at finite temperatures. All numerical simulations based on the proposed method are compared with fully atomistic calculations obtained by the Sandia-developed simulation code LAMMPS [Plimpton, 1995].

The same LJ potentials for NWs containing 373961 atoms are used in the MD simulations. A time step of 1 fs is used for the numerical integration. The system is equilibrated for 80 ps in a Nose-Hoover [Nosé, 1984] canonical (NVT) ensemble and 60 ps in a microcanonical (NVE) ensemble.

This is then followed by the application of strain along the NWs under a canonical ensemble. The equivalent isothermal SCB model contains a regular mesh of 1323 elements and 1792 nodes, which results in a 99.5% decrease in the number of the degrees of freedom as compared to the full-blown MD simulation. The volume integral in (6.11) is taken using $2 \times 2 \times 2$ Gaussian quadrature, while the surface integrals are evaluated using 2×2 Gaussian quadrature. The FEM solution is obtained by utilizing a non-linear Newton solver.

6.5 Results and Discussion

Initially, the numerical calculation based on the proposed method for the copper and nickel NWs at 0K is compared with the MD calculation. Due to the surface stress, the free end of the NW contracts upon relaxation. The longitudinal displacements found by the proposed model and MD calculations at 0K are shown in figure6.2. The proposed numerical method replicates the displacement profile in the longitudinal direction quite well, where a compressive strain of -0.414% and -0.098% are predicted, while the MD calculation predicted a contraction of -0.431% and -0.11% for Cu and Ni NWs, respectively. As predicted in previous literature [Park et al., 2006], due to the surface stress at 0K, the free end contracts, thus resulting in a compressive strain in the NW. This compressive strain is dramatically geometrical dependent, where long and slender NWs with higher transverse surface area endure a higher compressive strain compared to short and thick NWs [Yun and Park, 2009].

Analyzing and comparing the proposed method with corresponding MD calculations include the following three aspects:

1. Axial and transverse displacement profile in the proposed method vs. MD calculation for Cu NWs,

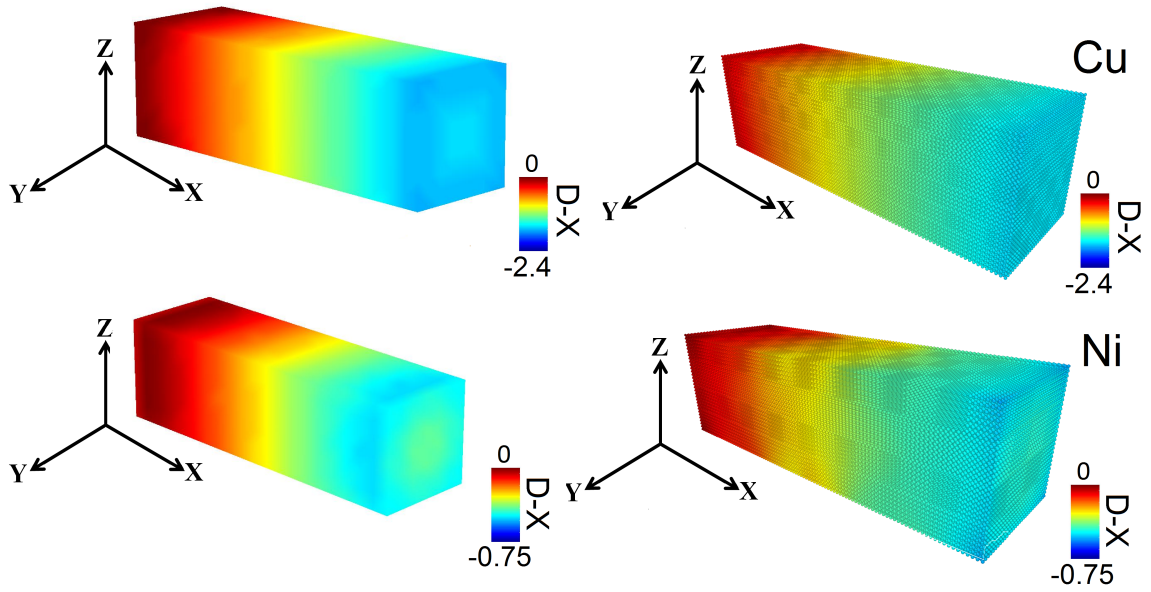


Figure 6.2: x-displacement for copper and nickel NWs with $100 \times 30 \times 30$ unit cells at 0K for TSCB (left) and MD (right).

2. Longitudinal strain of the stress-free system in the proposed method vs. MD simulation, and

3. Modulus of elasticity for the proposed model and MD calculations at different temperatures for Cu and Ni NWs.

In the first step, the TSCB calculation for a relaxed cantilever is compared with a snapshot of the MD calculations at 300K, 400K and 500K. The displacement profile in the x-direction for both TSCB and MD simulations are shown in figure6.3. The TSCB model replicates the displacement field in the x-direction at different temperatures to a good degree. It shows that the proposed multiscale approach can accurately capture the effect of thermal stress and surface stress in nanostructures at the same time.

The displacement in the transverse direction for the MD simulation is then calculated. The results are compared once again with those provided by the proposed model. The overall snapshot of the y-displacements at 500K for the TSCB and MD studies are shown in figure6.4. A good correspondence is observed as a result.

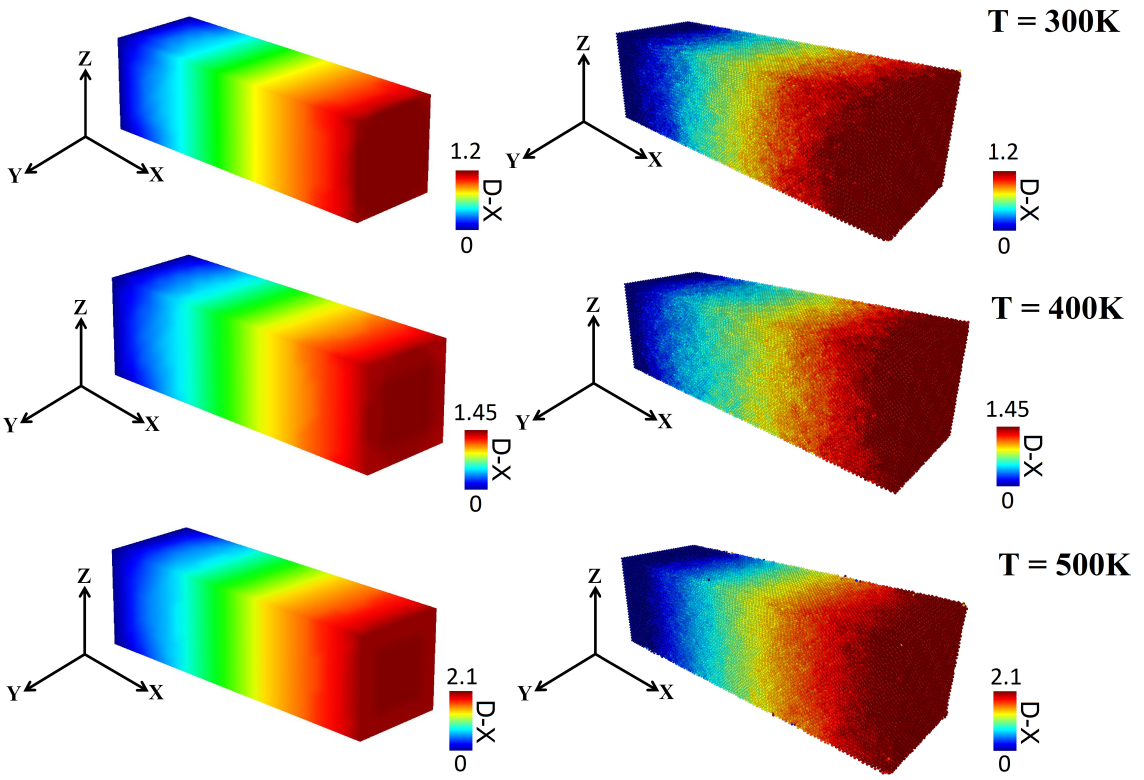


Figure 6.3: x-displacement for $31.6nm \times 10.8nm \times 10.8nm$ copper nanowire for TSCB (left) and the MD method (right) at 300K, 400K and 500K.

In the second step, the longitudinal strain for relaxed copper and nickel NWs at finite temperatures for both TSCB and MD simulations are calculated to further evaluate the accuracy of the proposed method in the estimation of the surface and thermal energies. This is achieved by measuring the displacement at the free end (figure6.5). Results indicate a good agreement between the TSCB and MD methods. We note that the effects of edges and corners are ignored, where the small nanostructures with effective edges and corners [Zhao and Yakobson, 2003] can be studied directly through the atomistic calculations.

The modulus of elasticity is a key parameter when studying the mechanical response of materials under static and dynamic loads.In the third step of validation, this fundamental parameter as predicted by the proposed method is compared with full, atomistic simulation results (figure6.6). Once again, the results demonstrate a

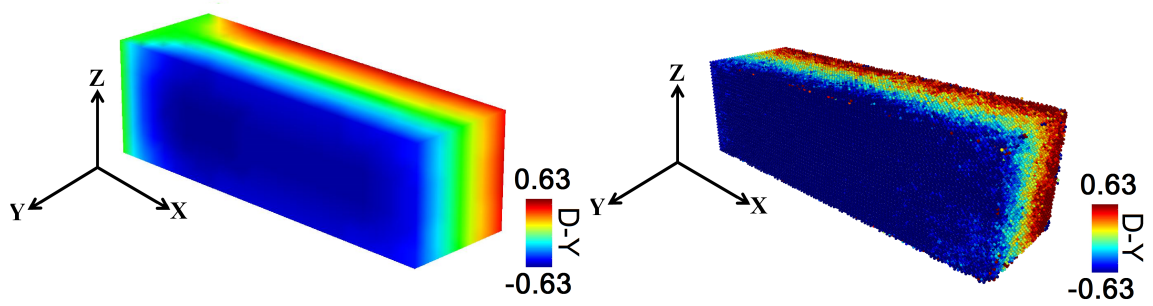


Figure 6.4: y-displacement field for $31.6nm \times 10.8nm \times 10.8nm$ copper nanowire for TSCB (left) and the MD (right) at 500K.

good agreement between the TSCB and MD methods in predicting the linear elastic response of NWs at temperatures below 500K. The capability of the TSCB method over 500K can be considered in a future study in the absence of any phase transformations, dislocation nucleation, and other crystal defects. Otherwise, non-local quasicontinuum methods should be used.

Finally, the capability of the proposed method for bulk structures without surface stress is validated by experimental results in the temperature range from 4K to 300K. Measured elastic properties of a copper single crystal in the $< 100 >$ direction based on the ultrasonic pulse technique [Overton Jr and Gaffney, 1955] was compared with the proposed method for the bulk strain energy, where the surface term in equation (6.11) was eliminated (figure6.7). The predicted elastic properties based on the proposed method have less than 8% error in comparison with experimental measurements verifying the proficiency of the proposed method for thermomechanical analysis of bulk FCC crystal structures as well.

Implementing temperature-dependent interatomic potentials in the SCB hypothesis was proposed by this work to study thermomechanical behavior of NWs. Thermomechanical calculation on relaxed and strained NWs proved the accuracy of the proposed model. Predicted elastic constants for NWs with surface energy contribution exhibit a higher stiffness compared to those reported by experimental studies for bulk crystal [Overton Jr and Gaffney, 1955].This shows the effect of surface atoms

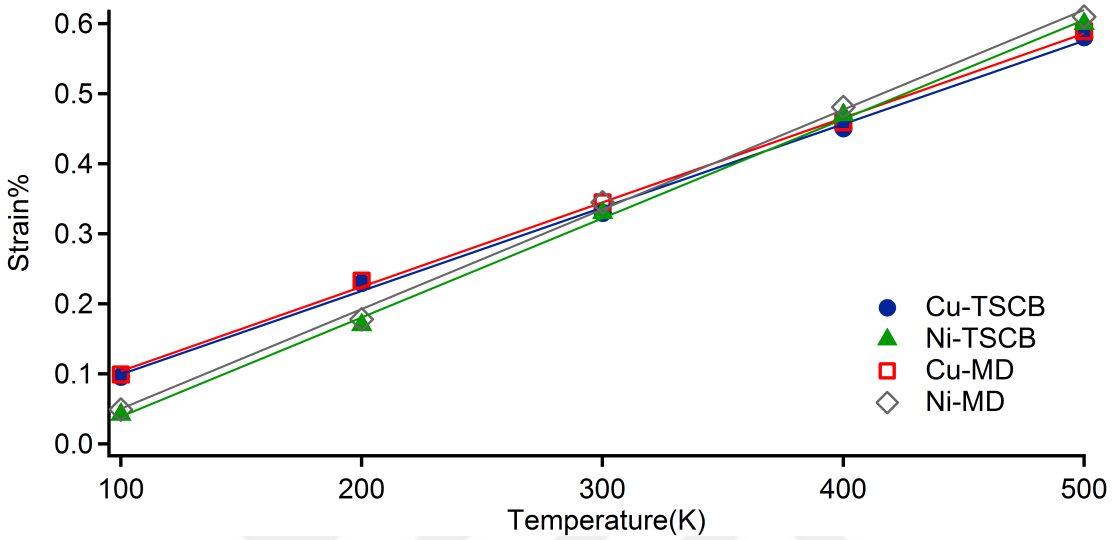


Figure 6.5: Uniaxial strain due to the interaction between surface and thermal stresses for $100 \times 30 \times 30$ unit cells copper and nickel NWs at different temperatures for TSCB and MD calculations.

on the mechanical response of NWs. We note that predicted elastic constants and uniaxial strains are in the $< 100 >$ crystal orientation. Thermomechanical properties along other crystal orientations can be considered in future studies.

The overall investigation is based on the two-body Lennard-Jones interatomic potential in metals with linear embedded energy [Foiles et al., 1986]. The temperature-dependence in interatomic potentials is included in the finite element calculations. For metals with non-linear embedded functions such as gold [Foiles et al., 1986], temperature-dependent embedded atom method (EAM) can be used instead [Subramaniyan and Sun, 2010]. The proposed method is applicable for defect-free single crystals. To include any imperfection in the crystal structure, non-local quasicontinuum model [Tadmor et al., 1996b] can be utilized.

6.6 Conclusion

We present the Thermo-coupled Surface Cauchy-Born method (TSCB), a multiscale coupling continuum-based theory at finite temperatures for the thermomechanical

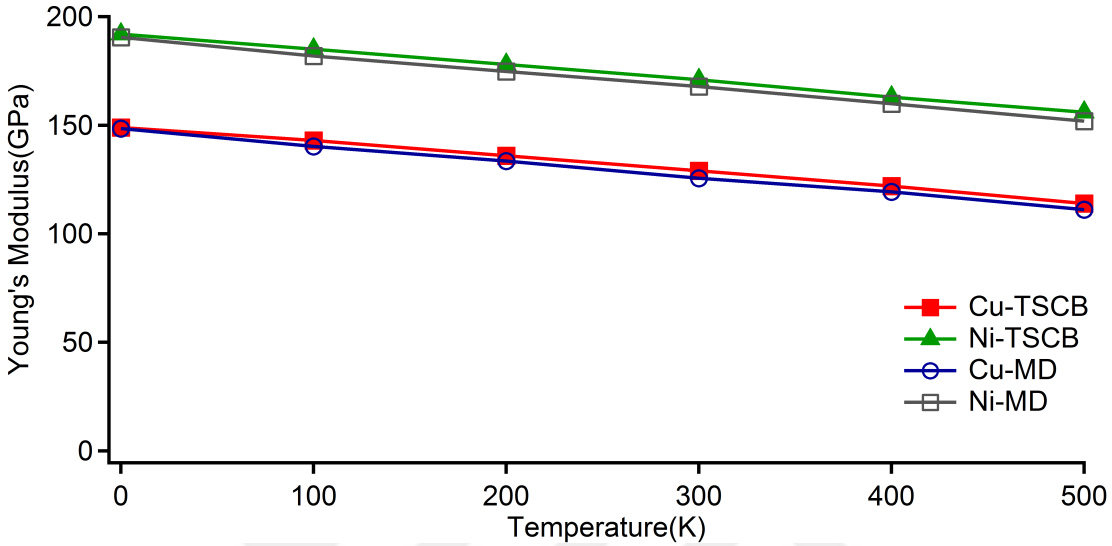


Figure 6.6: Youngs modulus at different temperatures predicted by TSCB and MD calculations.

analysis of NWs where surface stress has a significant contribution. The method is based on utilizing temperature-dependent strain energy density regarding EMM temperature-dependent interatomic potentials. This method provides a good accuracy and it is shown to be computationally much less demanding in comparison with available methods for the thermomechanical analysis with surface effects such as MD and quasiharmonic methods. The major outcome of this study is the possibility of utilizing temperature-dependent interatomic potentials to derive strain energy density for modeling surface effects. Implications of this chapter can be summed up as follows:

1. The possibility of coupling a temperature-dependent interatomic potential with the Cauchy-Born hypothesis for thermomechanical investigations in NWs and similar nanomechanical components.

2. Simplifications in calculations and dramatic reduction in computational efforts without a significant loss of accuracy. This provides a promising engineering tool without compromising the underlying physics of the problem.

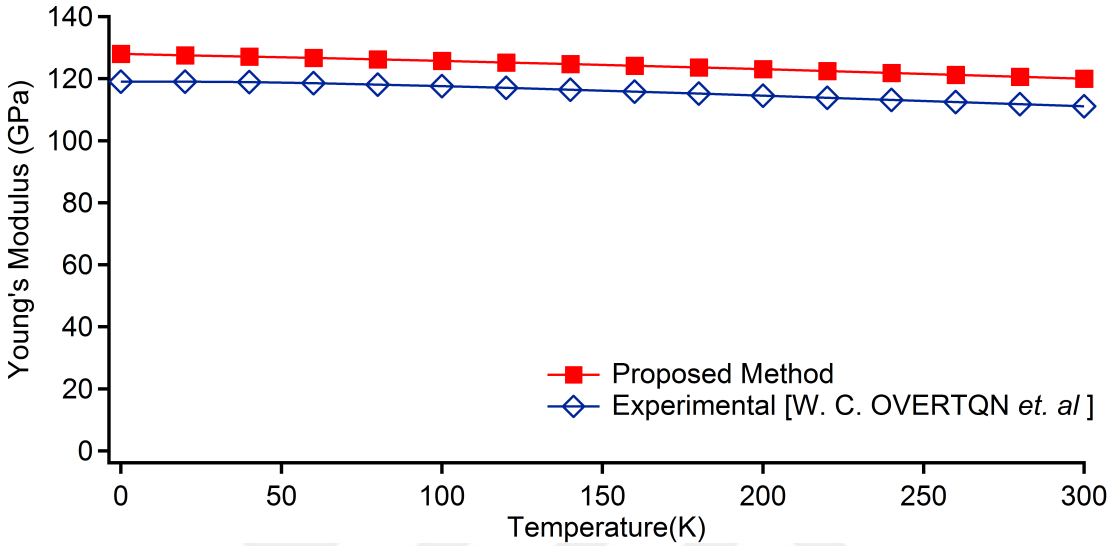


Figure 6.7: Youngs modulus at different temperatures predicted by the proposed method and experimentally.

3. The dominance of thermal stress over mechanical stress with increasing temperature leading to a transition in the NW strain profile from contraction to expansion.

Overall the performance of the TSCB technique in terms of simulation accuracy and computational demand is evaluated very positively. This initial study can further evolve to the derivation of momentum and heat equations in 3-dimensional nanostructures where surface stress effects and size-dependency are taken into the account.

Chapter 7

SILICON NANOWIRE MECHANICAL MODELING: SIZE AND ORIENTATION DEPENDENCE

7.1 Overview

As truly nanoscale building blocks, silicon nanowires find applications in electromechanical and electronic devices. A deeper understanding of their transport properties is of utmost importance for improving the performance of such devices or for introducing new functionalities. Due to this reason, the size dependence of properties has become a major field of study. The determination of the mechanical properties of silicon nanowires has proved to be specifically challenging with contrasting conclusions drawn from experimental and computational studies regarding the surface stress effect. In this respect a comprehensive study on crystal orientation and geometrical parameters can shed light on the role played by the surface stress in determining silicon nanowire mechanical behavior. This is accomplished by linking the local surface stress at the atomic scale to the overall behavior of the continuum system. The chapter starts by a primary surface analysis through atomistic simulations for silicon {100} and {110} surfaces. The implication of the surface stress on the mechanical behavior of a continuum system — nanowire in this work — is predicted through the basic elasticity problems. Surface stress is then transferred to the continuum system using the Surface Cauchy-Born approach. Deformation associated with the surface stress is computed for two different cantilevers with longitudinal orientations in $< 100 >$ and $< 110 >$ having {100} and {100}/{110} transverse surfaces, respectively. Results indicate twist deformation at the free end of $< 100 >$ silicon nanowires with rectangular cross-sections. Similarly, bending deformation is observed for $< 110 >$

silicon nanowires. A case study is carried out to emphasize the importance of surface stress in the operation of a nanowire electromechanical switch. Due to the associated deformations, surface stress is observed to cause variations in the electrostatic force along the nanowire cross-section by as much as 50%. The presented approach indicates a proper pathway to analyze surface stress effect on the mechanical behavior of nanowires. Addressing the existing controversy regarding the contribution of surface stress in the mechanical behavior of silicon nanowires, results in this chapter can provide a guideline for the interpretation of existing and the design of future experimental investigations.

7.2 Introduction

In the multi-disciplinary world of nanotechnology, NWs have found application in various fields. These one-dimensional structures have nanoscale cross-sectional dimensions along with a few micrometers of length, exhibiting an inherent three-order-of-magnitude scale difference. Such an extreme structural configuration introduces unique mechanical, optical and electrical properties [Zhang et al., 2016a]. The remarkable contribution of NWs in the field of nanoelectromechanical systems (NEMS) lead to the development of a series of new-generation sensors [Patolsky and Lieber, 2005, Sacchetto et al., 2011] and communication devices [Ekinci and Roukes, 2005, Durrani et al., 2013]. Specifically, Si NWs have emerged as promising NEMS building blocks due to their compatibility with IC. Some of their capabilities demonstrated so far include high-frequency operation beyond GHz [Ekinci and Roukes, 2005], mass detection at the level of zepto-gram [Gil-Santos et al., 2010], force sensing with a pico-Newton-level resolution [Arlett et al., 2011] and real-time biological sensing [Arlett et al., 2011, Carrara et al., 2012]. Hence, a comprehensive evaluation of Si NW electromechanical properties for such architectures is the key to improve design and implementation.

Downscaling Si NWs induces changes in transport properties. Among them, the

transition from indirect to direct band gap in Si NWs [Ma et al., 2003] is a significant phenomenon. MD simulations [Ponomareva et al., 2006] and density functional theories [Delley and Steigmeier, 1995] report surface effects on the band gap change confirming the experimental observation [Read et al., 1992, Ma et al., 2003]. Furthermore, such a modification of the bandgap energy influences optical characteristics enabling luminescence [Holmes et al., 2001]. Similar investigations on the size dependence of optoelectronic properties of Si NWs lead to unique applications in communications and photovoltaics [Priolo et al., 2014]. In addition, similar changes in thermal properties are reported for Si NWs [Hochbaum et al., 2008]. Finally, mechanical properties constitute the focus of the majority of NEMS studies for sensing applications [Craighead, 2000, Ekinci and Roukes, 2005].

Various methods have been utilized to measure the mechanical properties of Si NWs including resonance tracking [Li et al., 2003], bending via atomic force microscopy (AFM) [Hoffmann et al., 2006] or external probes [Wollschläger et al., 2016], electrostatic pull-in [Sadeghian et al., 2009], uniaxial tension test [Zhu et al., 2009] and nanoindentation [Sohn et al., 2010]. Available experimental results on Si NWs exhibit a significant size dependence of elastic properties. Li et al. [Li et al., 2003] and Sadeghian et al. [Sadeghian et al., 2009] showed a reduction of the modulus of elasticity in Si NWs in $< 110 >$ crystal orientation through top-down fabrication methods. Similarly, Zhu et al. [Zhu et al., 2009] and Kizuka et al. [Kizuka et al., 2005] reported a reduction in the modulus of elasticity in Si NWs grown through bottom-up approaches in $< 110 >$ and $< 100 >$, respectively. While synthesized Si NWs in $< 111 >$ exhibit an elastic modulus similar to that of the bulk Si [Hoffmann et al., 2006] — with a significant amount of data scatter due to varying levels of alignment success of the self-assembly with respect to micro-trenches — [Tabib-Azar et al., 2005], a slightly increase, *i.e.* stiffening, through size reduction is reported as well [Gordon et al., 2009].

While the presence of the native oxide and other surface defects are assumed to play an important role in the size dependence of the mechanical behavior

[Sadeghian et al., 2009], surface stress effect — as a direct result of dangling bonds on a particular surface — is considered to be the main parameter [Li et al., 2003]. Surface energy in Si is investigated through computational and experimental approaches. Sander et al. [Sander and Ibach, 1991] showed the changes in surface stress through the adsorption of oxygen on the surface, where surface stress profile was reported to be compressive and tensile on {111} and {100} crystal planes, respectively. Beside surface modification through atomic adsorption, surface reconstructions are investigated for different dimers. Such reconstruction can lead to a reduction in the surface energy in Si NW. Schlier et al. [Schlier and Farnsworth, 1959] reported a (2×1) periodicity on the (100) surface. Scanning tunneling microscopy observations and first-principle calculations exhibit a change in the surface morphology with a reduction of dangling bond density resulting in different surface stress states [Baski et al., 1997]. Furthermore, configuration of atomic bonds on the Si surface can be modified through the application of an external load. Sanz et al. [Sanz-Navarro et al., 2004] demonstrated atomic re-arrangement on the surface during nanoindentation using MD simulations. Finally, in resonance-based studies surface stress remains as a controversial subject from the size dependence point of view. While it is considered as the main reason for the reduction of the resonance frequency of Si NWs with reduced size [Sadeghian et al., 2009, Li et al., 2003], computational approaches predict a negligible surface stress effect [Park, 2008].

This controversy regarding the mechanical behavior of the Si crystal can be addressed through the fundamental calculation of the atomic stress. Stress calculation based on Hardys formula [Zimmerman et al., 2004] necessitates a modification to include many-body bond-order terms in the virial theorem [Chen, 2006]. Further consideration is required to study mechanical behavior of Si NWs with a high surface contribution. Various computational approaches are utilized to predict the Si NW mechanical behavior by taking the surface effect into consideration. The continuum method incorporates the surface effect by including geometrical and surface elastic parameters in the effective stiffness calculation [Miller and Shenoy, 2000]. In

contrast, more complicated MD calculations employ the density functional theory to calculate mechanical properties through downscaling Si NWs to sub-20-nm thickness [Rudd and Lee, 2008]. Selecting the optimum approach necessitates a proper guideline for the mechanical modeling [Esfahani et al., 2016b], where multiscale approaches are proposed as efficient tools. SCB [Park et al., 2006] is one such numerical method integrating the surface energy into the continuum calculations. The method is based on deriving constitutive response of the bulk and surface from the interatomic potentials. The method predicts mechanical behavior of metal [Park and Klein, 2007, Esfahani et al., 2016b] and Si NWs [Park and Klein, 2008a] at 0 K, while thermo-coupled SCB [Esfahani et al., 2016a] is recently introduced as an efficient approach for including surface energy at a finite temperature.

Computational studies have been carried out mostly for Si NWs with square cross-sections in $< 100 >$ crystal orientation [Rudd and Lee, 2008, Park and Klein, 2007, Park and Klein, 2008a], while experimental studies report non-symmetric [Sadeghian et al., 2009, Li et al., 2003] and circular cross-sections [Tabib-Azar et al., 2005, Zhu et al., 2009, Kizuka et al., 2005] fabricated through top-down and bottom-up approaches, respectively. Hence, analyzing the surface stress effect on the Si NW behavior necessitates a comprehensive investigation of crystal orientations and geometrical parameters.

In this chater, we present size and crystal orientation dependence of Si NW surface stress through a primary surface analysis via atomistic benchmark and transition to multiscale modeling, SCB, for continuum structures. The theoretical framework is explained first including Si atomic description, the SCB theory and Si surface in continuum frameworks. Then, surface stress is calculated for $\{100\}$ and $\{110\}$ surfaces through the virial theorem. After the implementation of the surface stress in the atomistic system, it is then transferred to the continuum. Surface stress is calculated for continuum systems based on the SCB approach. Deformation associated with the surface stress is computed through minimizing the total energy of the system for Si NWs with fixed-free (cantilever) boundary condition. The study is carried

out for Si NWs in two different longitudinal crystal orientations of $< 100 >$ and $< 110 >$ with $\{100\}$ and $\{110\}/\{100\}$ transverse surfaces, respectively. The effect of the cross-sectional profile on such deformation is also investigated. Results are compared against those obtained through molecular statics simulations. Deformation of Si NWs is linked to the atomistic calculations and additional degrees of freedom in the continuum definition. This chapter is concluded with an investigation of the direct implication of size and crystal orientation on the electromechanical behavior of a Si NW forming a nanoelectromechanical switch near a gate electrode.

7.3 Theory

7.3.1 Atomic-level description

Silicon has diamond lattice structure in the form of two partially overlapping FCC lattices (figure 7.1). Each bulk atom in the FCC group A has four-folded interatomic bond with four atoms from the FCC group B in a tetrahedral form representing two perpendicular planes (110) and $(1\bar{1}0)$. Tersoff-T3 interatomic potential [Tersoff, 1989] is utilized in the present work with a corresponding expression of the many-body potential, U, as

$$U = \frac{1}{2}\sum_{i \neq j} V_{ij} \tag{7.1}$$

with V_{ij} representing bonding energy between atom i and j as follows

$$V_{ij} = f_c(r_{ij})(Me^{-\lambda r_{ij}} - b_{ij}Ne^{-\mu r_{ij}}) \tag{7.2}$$

where r_{ij} is the distance between atom i and j, f_C is cut-off function utilized for including effectively a nearest-neighbor potential, M is the coefficient of the repulsive force and N is the coefficient of attractive force. The function of bond order, b_{ij}, describes the dependence of the bond-formation energy on the local atomic arrangement due to the presence of the other neighboring atoms and it is given by

$$b_{ij} = (1 + \beta^n \zeta_{ij}^n)^{-1/2n} \tag{7.3}$$

where ζ_{ij}, the effective coordinate number, is expressed as

$$\zeta_{ij} = \sum_{k \neq i,j} f_c(r_{ij}) g(\theta_{ijk}) \tag{7.4}$$

with $g(\theta_{ijk})$ representing the stabilization function of the tetrahedral structure and θ_{ijk} representing the bonding angle between i-j and i-k bonds (figure7.1).

$$g(\theta_{ijk}) = 1 + \frac{c^2}{d^2} - \frac{c^2}{d^2 + (h - cos\theta_{ijk})^2} \tag{7.5}$$

All coefficients in the formulation are listed in Table 7.1. For each bond, the bond order function depends on the number of the neighboring atoms within the cut-off distance. Tersoff-T3 potential is based on the many-body potential for nearest neighbors. Thus, any bulk atom has four bonds in the initial configuration with bond length equal to $\sqrt{3}a_0/4$, with a_0 being the lattice parameter of the Si crystal.

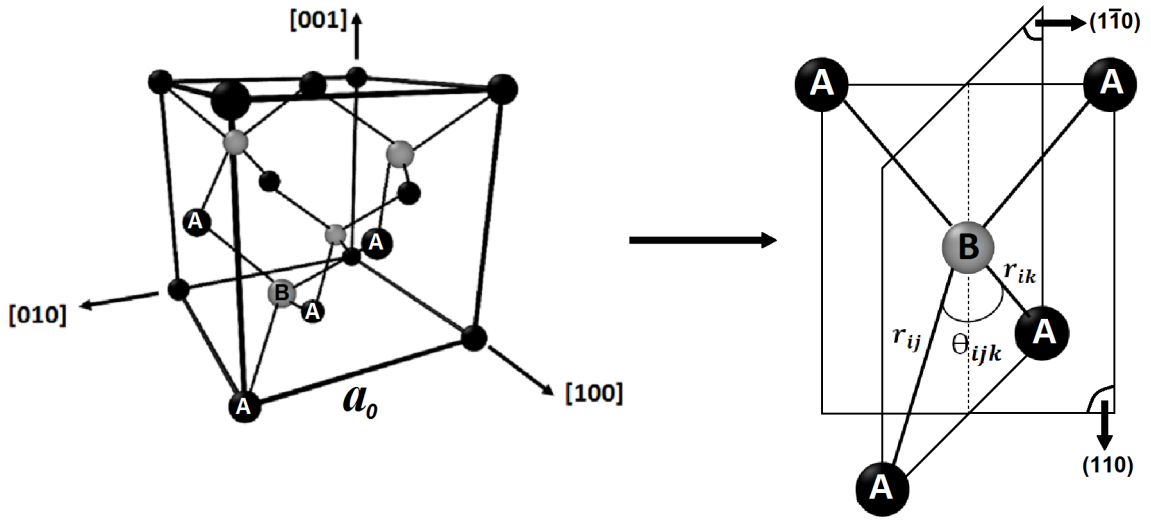


Figure 7.1: Diamond cubic lattice structure of Si as two interpenetrating FCC lattices.

Table 7.1: Constant parameters for Tersoff-T3 potential [Tersoff, 1989].

Parameter	Value
M	1830.8 eV
N	471.18 eV
λ	2.4788 $\mathring{A}^{-1}$
μ	1.7322 $\mathring{A}^{-1}$
β	1.1×10^{-6}
n	0.78734
c	100390
d	16.217
h	-0.59825

7.3.2 SCB formulation

To formulate a constitutive law for a continuum framework starting from the atomic interactions in the crystal, Cauchy-Born hypothesis can be utilized based on Green elastic theory. Continuum stress and modulus are calculated based on the strain energy density function, φ. Formulating strain energy density with continuum terms such as deformation gradient, F, or right stretch tensor, $C = F^T F$, provides material frame indifference. Strain energy density for the Tersoff-T3 potential can be express as

$$\varphi = \frac{1}{\Omega_0} \sum_{i \neq j} U(r_{ij}) \tag{7.6}$$

where Ω_0 is the atomic volume in the undeformed configuration. There is an additional inner displacement for the two interpenetrating FCC lattices (Lattice A and B in figure 7.1) resulting from energy relaxation with respect to the initial atomic positions [Park et al., 2006]. Cauchy-Born rule for deformed bond, r_{ij}, can be express as

$$r_{ij} = FR_{ij} + \xi \tag{7.7}$$

where R_{ij} is the bond vector in reference configuration and ξ is the induced displacement between two FCC groups in the undeformed body. For an atomic system with no thermal fluctuation at $0K$, the strain energy density can be defined based on the interatomic potential for the deformed bond vector and the internal degree of freedom, hence, $\varphi = \varphi(C, \xi)$. The strain energy density for a deformed system is minimized with respect to the internal displacement to derive the equilibrium internal degree of freedom, $\xi = \xi(C)$ as

$$(\frac{\partial \varphi}{\partial \xi}) = 0 \tag{7.8}$$

This leads to an expression of the strain energy density merely as a function of C, such that $\varphi = \varphi(F, \xi) \equiv \hat{\varphi}(F)$. The second Piola-Kirchhoff stress, S, and elastic constants, D_{IJKL}, for Tersoff-T3 potential can be obtained from the strain energy density as follows:

$$S = 2\frac{\partial \hat{\varphi}}{\partial C} \tag{7.9}$$

$$D_{IJKL} = 4\frac{\partial^2 \hat{\varphi}}{\partial C_{IJ} \partial C_{kl}} - 4[\frac{\partial^2 \hat{\varphi}}{\partial \xi_P \partial \xi_Q}]^{-1} \frac{\partial^2 \hat{\varphi}}{\partial C_{IJ} \partial \xi_P} \frac{\partial^2 \hat{\varphi}}{\partial C_{KL} \partial \xi_Q} \tag{7.10}$$

Surface energy for a continuum body can be captured based on the SCB theory [Park et al., 2006]. According to this approach, the total energy of the system is expressed in terms of bulk and surface components. The constitutive law for bulk nodes can be extracted from fully coordinated atoms, where the strain energy is calculated for all neighbors. This facilitates the derivation of the bulk elastic properties for a defect-free crystal structure. On the other hand, the surface constitutive law is

derived from unbalanced atoms having different strain energy than the bulk atoms leading to a different constitutive law for the surface nodes. This surface stress due to the dangling bonds causes deformation in NWs in the form of contraction for FCC NWs [Park and Klein, 2007] and expansion for Si NWs [Park and Klein, 2008a] in $< 100 >$ crystal orientation. The total potential energy of the continuum body can be expressed as

$$\Pi(u) = \int \varphi(C) d\Omega + \sum_{n=1}^{N_{surface}} \int \gamma^n(C) d\Gamma^n \tag{7.11}$$

where γ^n is the surface energy for surface n with a different atomic arrangement than that within the bulk. This difference provides a new internal degree of freedom for the surface n, ξ_s^n. The surface strain energy density for a deformed system must then be minimized according to the surface internal displacement as

$$(\frac{\partial \gamma^n}{\partial \xi_s^n}) = 0 \tag{7.12}$$

Hence, the surface strain energy density becomes a function of continuum deformation only, such that $\gamma^n = \gamma^n(C, \xi) \equiv \hat{\gamma}^n(C)$. The surface second Piola-Kirchhoff stress, S_s^n, and elastic constants, $D_{s\,IJKL}^n$, can then be expressed as follows:

$$S_s^n = 2\frac{\partial \hat{\gamma}}{\partial C} \tag{7.13}$$

$$D_{s\,IJKL}^n = 4\frac{\partial^2 \hat{\gamma}}{\partial C_{IJ} \partial C_{kl}} - 4[\frac{\partial^2 \hat{\gamma}}{\partial \xi_P \partial \xi_Q}]^{-1} \frac{\partial^2 \hat{\gamma}}{\partial C_{IJ} \partial \xi_P} \frac{\partial^2 \hat{\gamma}}{\partial C_{KL} \partial \xi_Q} \tag{7.14}$$

7.3.3 Surface energy in $\{100\}$ *surface*

The specific atomic arrangement on a crystal surface imposes a surface stress. This can contribute to the mechanical behavior especially if the surface has a dominant presence, as it is the case with NWs [Miller and Shenoy, 2000, Park et al., 2006]. The

atomic arrangement on the surface defines the stress state based on the symmetrical invariance. Si crystal structure has rotational invariance by considering the internal degree of freedom, ξ. Therefore, the conjunction of the surface energy variation with respect to the initial configuration determines the surface stress state. Surface atomic arrangement for the unreconstructed {100} plane is shown in figure 7.2.

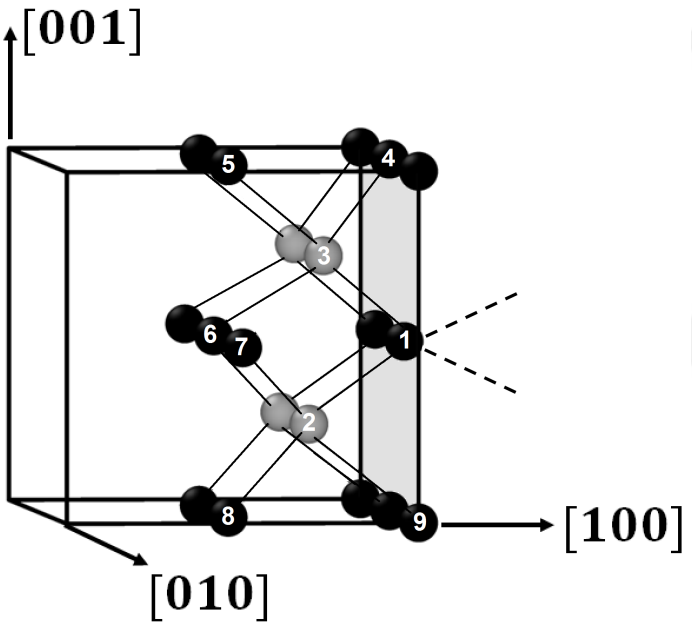


Figure 7.2: Illustration of the atomic arrangement on the {100} surface (grey-shaded). Black and grey atoms represent FCC lattice groups A and B, respectively. Dashed lines depict dangling bonds of the surface atom 1.

Let us consider black atom 1 of group A as the surface atom with two dangling bonds on the {100} surface. It has two bonds with two grey atoms 2 and 3 in group B. Grey atom 3 has fully coordinated bonding with black atoms (1, 4, 5, 7). Similarly, grey atom 2 has four-folded arrangement providing two perpendicular planes with atoms in group A (1, 7, 8, 9). Black atom 1 is displaced with respect to atoms in group B (atoms 2 and 3). This is how atoms 2 and 3 are taken into account in the estimation of the surface energy. Therefore, atoms 1, 2 and 3 primarily contribute to the surface energy. Hence, the surface energy density for the {100} plane can be written as

$$\gamma_{100}^{n} = \frac{1}{\Gamma_{100}^{n}}\left(\sum_{j=2,3} V_{1j}(r_{1j}) + \sum_{k=1}^{4} V_{2k}(r_{2k}) + \sum_{m=1}^{4} V_{3m}(r_{3m})\right) \tag{7.15}$$

where Γ_{100}^{n} is the area per atom on the $\{100\}$ surface. Surface atoms — atoms 1, 2 and 3 — are located on the (011) plane, while the corresponding atoms defining the mirror (opposing) $(\bar{1}00)$ surface are on the $(0\bar{1}1)$ plane. This atomic configuration on both sides of the Si NW can, in principle, lead to stresses of opposite sign. Further investigation for such an anti-symmetric atomic configuration on mirror surfaces will be carried out in Section7.4 through an atomistic calculation.

7.3.4 Surface energy in $\{110\}$ *surface*

We have seen that breaking two bonds of the four-folded arrangement provides a unit cell with $\{100\}$ surfaces (figure 7.2), where one un-balanced atom with two bulk atoms contribute to the internal degree of freedom. However, the formation of the $\{110\}$ surface necessitates the removal of one atom in each atomic group A and B (figure 7.3). This operation requires both atomic groups A and B on the free surface lose one bond in [110] direction. Surface atoms are displaced with respect to the atoms located on the closest layer within the bulk.

Atoms on the $\{110\}$ surface (2 and 4 in group B, 1 and 3 in group A) form three bonds as opposed to four in the bulk. Each of these group-A atoms has three bonds with two group-B atoms on the $\{110\}$ surface (atoms 2 and 4) and one bond with a group-B atom in the bulk (atom 6). With the same configuration, each group-B atom on the surface is connected to three group-A atoms, two of which are located on the $\{110\}$ surface (atoms 1 and 3) and another one in the bulk (atom 5). Therefore, a surface unit cell can be considered as a group of atoms on the top surface and one layer into the bulk contributing to the internal displacement. Surface energy for a unit cell of $\{110\}$ surface can thus be expressed as

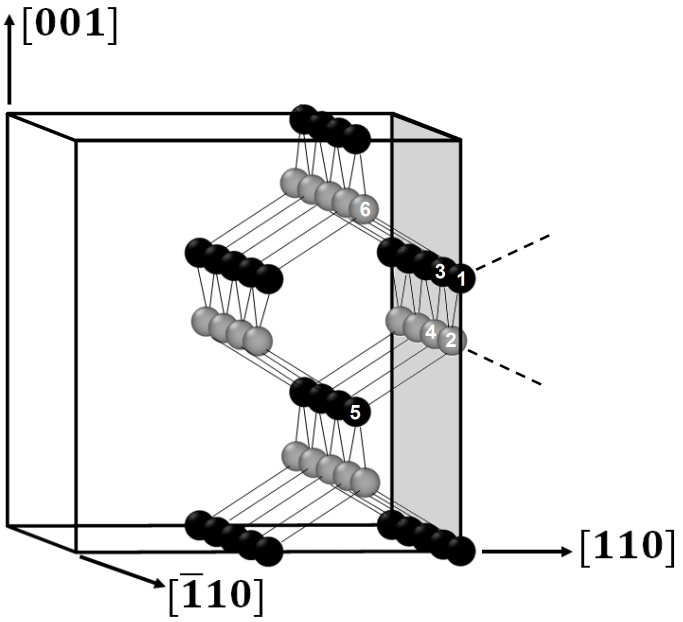


Figure 7.3: Schematic of atomic bonding on the {110} surface (grey shaded). Black and gray atoms represent FCC lattice groups A and B, respectively. Dashed lines depict dangling bonds of the surface atoms 1 and 2.

$$\gamma_{110}^{n} = \frac{1}{\Gamma_{110}^{n}}\Big(\sum_{j=2,4} V_{3j}(r_{3j}) + \sum_{k=1}^{4} V_{6k}(r_{6k}) + \sum_{p=1}^{4} V_{2p}(r_{2p}) + \sum_{q=1}^{4} V_{5q}(r_{5q})\Big) \tag{7.16}$$

where Γ_{110}^{n} is the area per atom on the surface {110}. Surface atoms (2 and 4 in group B, 1 and 3 in group A) have two bonds in (110) plane with one bond in $(1\bar{1}0)$. Such atomic arrangement can induce surface stress in [100] and [110] directions. Additional calculations will be conducted in Section 7.4 for clarifying atomic stress profile on the free surface.

7.4 Surface stress benchmark

As a continuum concept stress is difficult to express at the atomic scale. Therefore various studies have been devoted to the development of an atomic-level stress

simulation connecting continuum definitions with atomic systems using a multi-scale mechanical modeling platform. To evaluate the surface stress state in different Si crystal orientations, the thin film model is considered with free surfaces in x-direction and a periodic boundary condition in y- and z-directions (figure 7.4). Thin film thickness is considered to be large enough to prevent interference of the two free surfaces. Since there is no external force acting on the free surfaces and the two other remaining directions have periodic boundary conditions, the stress in the thickness direction provides an indication for the atomic stress state on the free surface. Although the virial theorem — an approach based on volumetric average calculation — cannot predict the correct magnitude of the stress at the free surfaces [Zimmerman et al., 2004], stress state forms the main focus of this section. Such an evaluation of the surface stress is directly linked to the atomic arrangement on the free surfaces as indicated in Figs. 7.2 and 7.3.

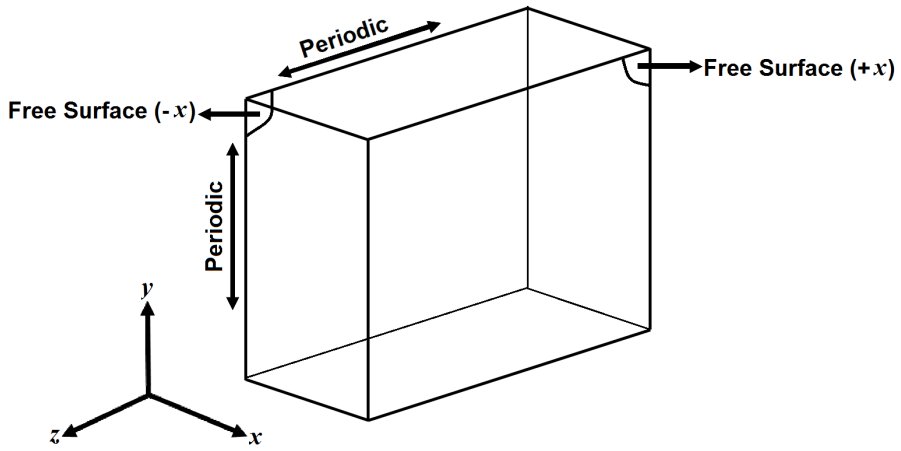


Figure 7.4: Thin film consists of two periodic boundary conditions in y- and z-directions and two free surfaces in x-direction.

Atomic stress in a quasistatic system without any thermal oscillations can be expressed as [Zimmerman et al., 2004]

$$\pi_{ij}^{\mu} = \frac{1}{2\Omega_0^{\mu}}\left(\sum_{\alpha=1}^{N}\sum_{\beta\neq\alpha}^{N}\frac{1}{r^{\alpha\beta}}\frac{\partial U(r^{\alpha\beta})}{\partial r}(\nu_i^{\alpha\beta}\nu_j^{\alpha\beta})\right) \tag{7.17}$$

where Ω_0 is the atomic volume in the undeformed atomic system for atom μ, N is the total number of atoms, $r^{\alpha}\beta$ is atomic distance between two atoms α and β, $\nu_j^{\alpha\beta} = \nu_i^{\alpha} - \nu_i^{\beta}$ and U is the interatomic potential. Atomistic simulation is carried out for the thin film model (figure 7.4) to analyze stress on {100} and {110} surfaces. Film thickness is taken to be 40 atomic layers. Atomic stress is calculated for a film with a crystal orientation of [100], [001], and [010] in x-, y-, and z-directions, respectively. Stress profile along the thin film thickness (x-direction) is shown in figure 7.5.a. All components of the stress tensor are depicted along the normalized thin film thickness. Stress state on the top three atomic layers ($+x$) are shown in further detail in figure 7.5.b.

Data plotted in figure 7.5 exhibit negligible stress components within the bulk, while they increase significantly towards the surface. All normal components $(\sigma_{xx}, \sigma_{yy}, \sigma_{zz})$ of the stress tensor on the {100} surface are compressive. Shear stresses σ_{xy} and σ_{xz} are negligible, while shear stress σ_{yz} has a positive sign on the (100) surface and a negative sign on the $(\bar{1}00)$ surface. Such non-symmetric distribution of shear stresses on mirror surfaces can be linked to the specific atomic configuration on the surface. A surface atom on (100) surface (atom 1 in figure 7.2) has bonds with two bulk atoms (atoms 2 and 3 in figure 7.2) lying on (011), while the corresponding surface atom on $(\bar{1}00)$ surface is connected to bulk atoms on $(0\bar{1}1)$. Such 90°-rotation for surface bonding on mirror {100} surfaces leads to shear stress components in opposite directions.

Stress along the film thickness in $< 110 >$ direction on {110} free surfaces is calculated next for a film with crystal orientation of [110], [001], and $[\bar{1}10]$ in x, y, and z-directions, respectively. figure 7.6.a shows all of the six component of the stress tensor along the atomic layers of the thin film in x-direction. Atomic stress on the top three layers in x-direction is depicted in a close-up in figure 7.6.b. Similar to the atomic stress on {100} surfaces, bulk atoms are found to be stress-free, while stress tensor on the free surface has compressive normal components $(\sigma_{xx}, \sigma_{yy}, \sigma_{zz})$ only. Shear stresses σ_{xz} and σ_{yz} are insignificant. Shear stress σ_{xy} for atoms in group

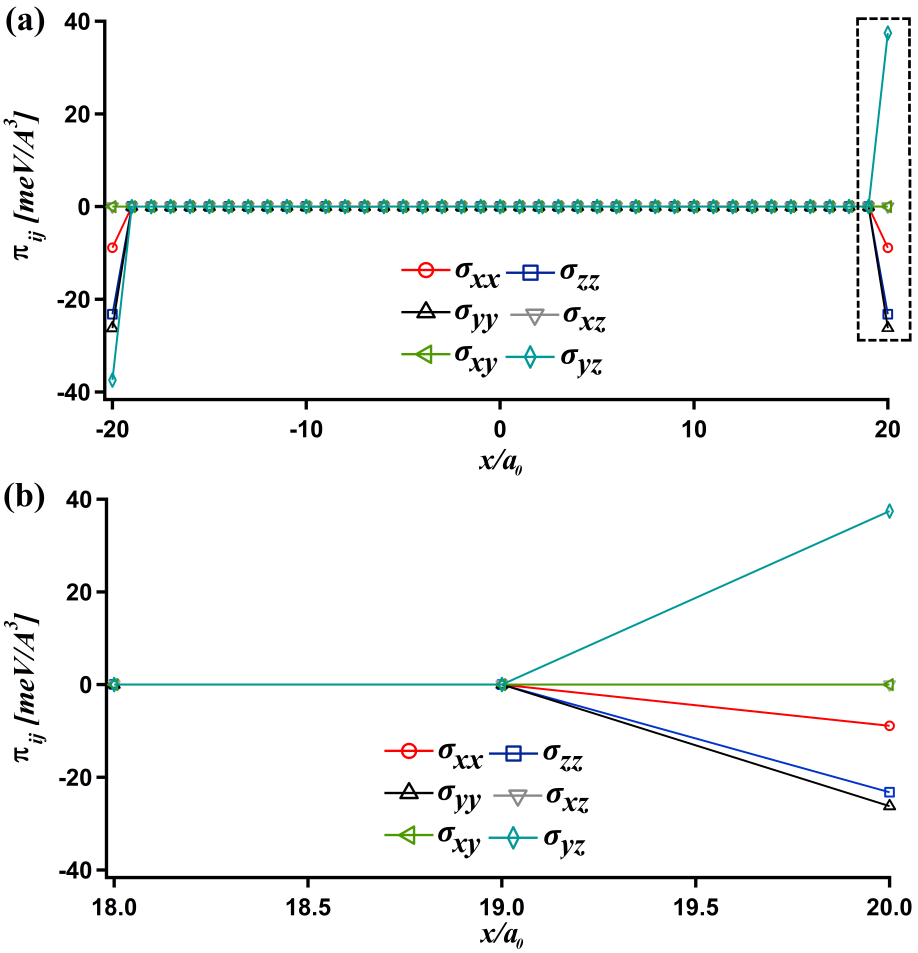


Figure 7.5: (a) Atomic stress based on the virial theorem (Eq. (16)) along the thin film thickness, x, in $< 100 >$ direction with $\{100\}$ free surface, (b) A close-up (within the dashed box of (a)) showing details of the atomic stress components in the immediate vicinity of the top surface $(+\ x)$.

A (atoms 1 and 3 in figure 7.3) , σ_{xy}^{A}, has a positive sign on (110) and a negative sign on $(\bar{1}10)$, while this shear stress for atoms in group B (atoms 2 and 4 in figure 7.3) , σ_{xy}^{B}, behaves in an opposite fashion, *i.e.* it assumes a negative sign on (110) and a positive sign on $(\bar{1}10)$. Atoms in group A on the free surface displace with respect to the atoms in group B located one layer into the bulk (atom 6 in figure 7.3) in $< \bar{1}11 >$ direction. In contrast, the displacement of atoms in group B on the free surface with respect to the atoms in group A located one layer into the bulk (atom 5 in figure 7.3) takes place in $< \bar{1}1\bar{1} >$ direction. Such mutually perpendicular displacement of atoms

on the free surface in group A and B causes a reverse sign in shear stress σ_{xy}.

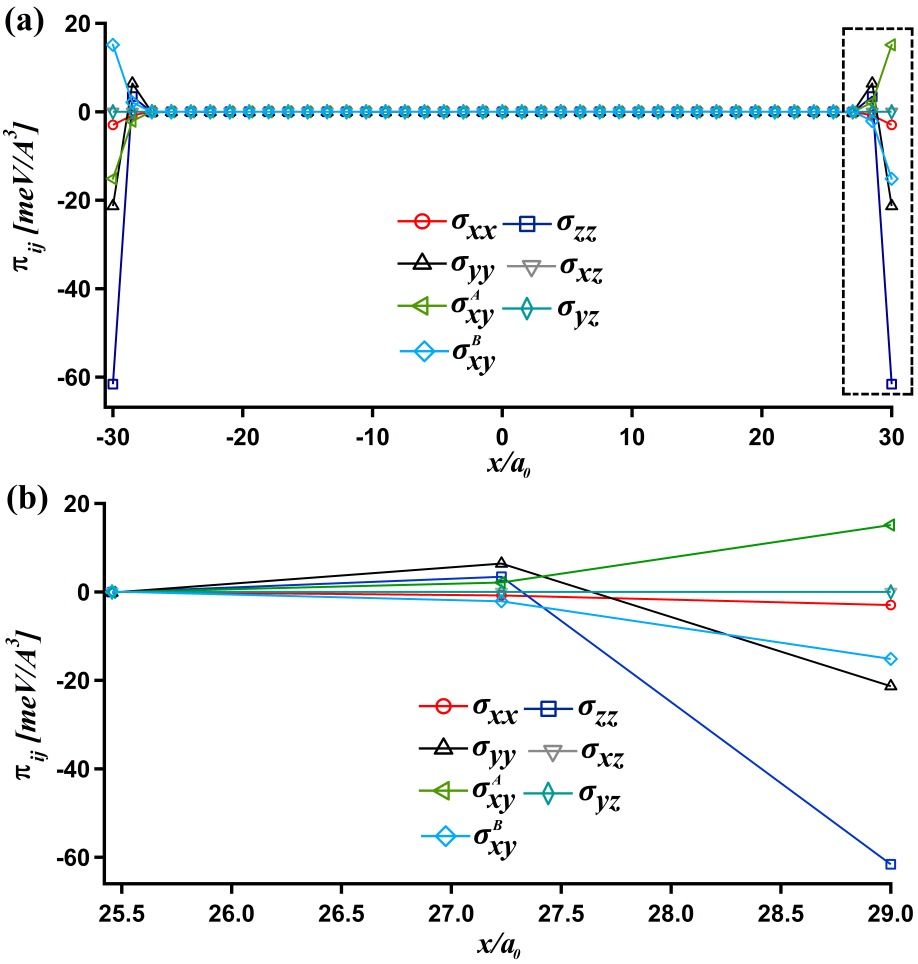


Figure 7.6: (a) Atomic stress based on the virial theorem (Eq. (16)) along the thin film thickness, x, in $< 110 >$ direction with $\{110\}$ free surface, (b) A close-up showing details of the atomic stress components in the immediate vicinity of the top surface $(+\ x)$.

7.5 Numerical study

Based on the atomistic calculation of the previous section, atomic stresses are studied for $\{100\}$ and $\{110\}$ Si crystal surfaces. The implication of the distribution of stresses in Si NWs — as the leading NEMS component — is investigated by transferring the intrinsic surface stress to a continuum system through the SCB approach. The impact

of such surface stresses on the deformation of Si NWs is studied. Numerical examples are carried out on Si NWs with fixed-free boundary conditions in two different crystal orientations. Results are compared with molecular statics simulations. The impact of the anti-symmetric surface stress on the deformation of Si NWs with rectangular cross-sections is investigated. All numerical calculations in this study are conducted at $0K$.

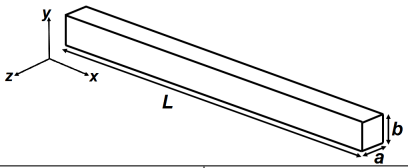
All NWs are defined in the cantilever form by fixing one end, whereas the other end is free to move enabling one to capture surface stress relaxation. Involved dimensions and orientations are listed in Table 7.2. Two different crystal orientations with different aspect ratios (AR), defined as thickness-to-width ratio, b/a, are considered. Numerical calculations are performed with regular eight-node hexahedral elements without an external load. All numerical simulations are compared with fully atomistic calculations obtained by the Sandia-developed simulation code LAMMPS [Plimpton, 1995] using the Tersoff-T3 potential [Tersoff, 1989]. Molecular static simulations consisted of 410,000 to 1.2 million atoms, while numerical calculations consisted of 19,000 to 50,000 degrees of freedom. Quasistatic calculations are performed in atomistic and numerical simulations to obtain the minimum energy in the presence of the surface stress.

7.6 Results and Discussion

7.6.1 Crystal Orientation I

A snapshot of the longitudinal, x, displacement found by the numerical and atomistic simulations for the NWs is shown in figure 7.7. Numerical calculations based on SCB replicate the major features of the displacement field predicted by atomistic simulations. A similar behavior to what was predicted previously in Si NWs with symmetrical cross-sections [Park and Klein, 2008a] is observed. Si NWs expand in the longitudinal direction due to the surface stress, while the associated uniaxial tensile strain gradually decreases from 0.28% to 0.17% with the AR increasing from 1 to 3.

Table 7.2: Summary of NW dimensions and crystal orientations.



Crystal Orientation *I*			Crystal Orientation *II*		
x	y	z	x	y	z
[100]	[001]	[010]	[110]	[001]	$[\bar{1}10]$
NW Dimensions			*NW Dimensions*		
L (nm)	***b (nm)***	***a (nm)***	***L (nm)***	***b (nm)***	***a (nm)***
120	8	8	120	8.4	8.4
120	16	8	120	16.3	8.4
120	24	8	120	24.4	8.4

The z- and y-displacements for relaxed Si NWs are shown in figure 7.8 and figure 7.9, respectively. Results exhibit a twist deformation at the free end in the case of the rectangular cross-section, while such deformation is negligible with the square cross-section (AR = 1). The maximum twist angle (with AR = 3) is about 5° increasing from 0.003° with AR = 1. This type of deformation can be linked to the shear stress on the {100} free surface in y- and z-directions. Surface atoms in mirror planes such as (010) and $(0\bar{1}0)$ in z-direction impose shear stresses with reverse directions. Same phenomenon is observed for (001) and $(00\bar{1})$ planes in y-direction as well. Such surface stresses provide the torsional load twisting the free end.

A direct outcome of the torsional deformation is the change in mechanical stiffness. Twist rate coefficient, defined as the ratio of the twist angle to the length, directly contributes to the governing equation of motion [Banerjee, 2001]. Influence of such twist deformation on the free vibration of cantilevers was investigated previously indicating a significant effect on the resonance frequency and mode shapes [Banerjee, 2001]. Twist deformation in NWs with helical morphologies are linked to

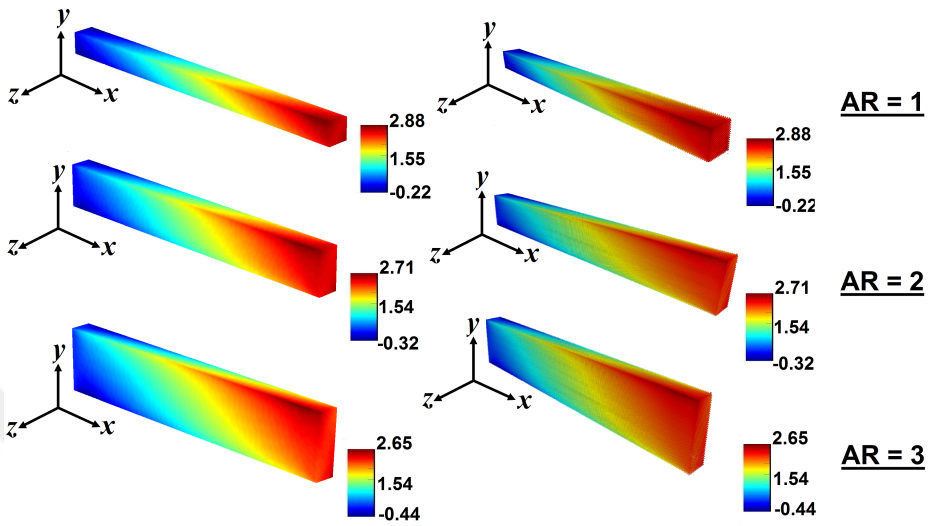


Figure 7.7: x-displacement of Si NWs with crystal orientation I obtained through numerical (left) and atomistic (right) methods (in $\mathring{A}$).

anisotropic surface stresses [Wang et al., 2008]. The torsional deformation reported in this study is induced by the surface energy, as it exhibits different deformation kinematics. Surface stress effect in Si NWs with $< 100 >$ crystal orientation was predicted previously [Park and Klein, 2008a]. Here, for the first time, atomic surface stress state is incorporated with geometrical parameters in a continuum system to predict Si NW mechanical behavior. Significant twist deformation is depicted for relaxed Si NWs with $< 100 >$ crystal orientation and rectangular cross-sections. Although the effect of surface stress on flexural rigidity is found to be negligible for relaxed Si NWs with square cross-sections [Park, 2008], the effect of AR on flexural stiffness of Si NWs with $< 100 >$ crystal direction necessitates further investigations.

7.6.2 Crystal Orientaion II

A snapshot of the longitudinal, x, displacement found by SCB-based and atomistic simulations for the relaxed Si NWs is shown in figure 7.10. Once again SCB predicts a displacement profile similar to that of the atomistic calculations. Results exhibit an expansion along the longitudinal direction with a gradient in the thickness, y,

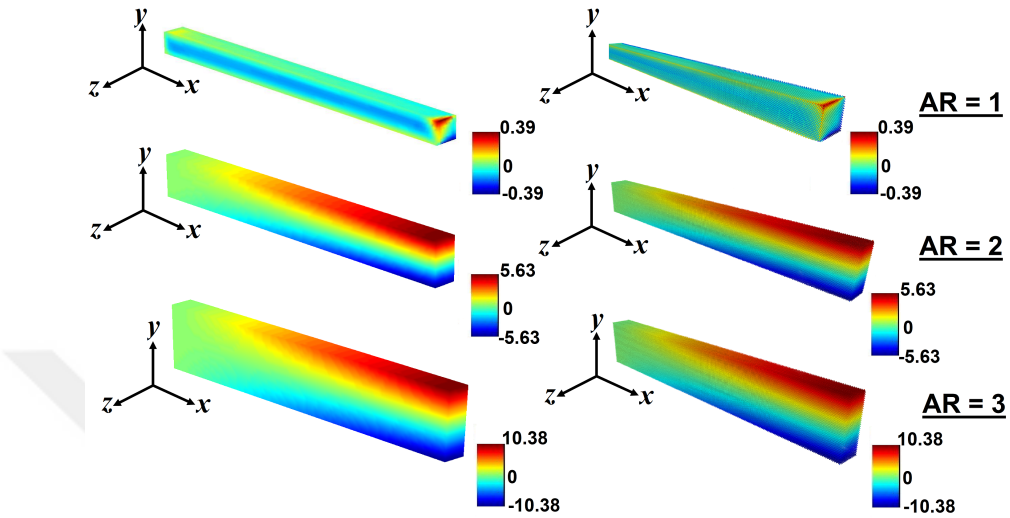


Figure 7.8: z-displacement of Si NWs with crystal orientation I obtained through numerical (left) and atomistic (right) methods (in $\mathring{A}$).

direction. An average expansion of about 2.4% is observed in the case of the square cross-section.

Results exhibit insignificant deformation in z-direction (figure 7.11), while displacement in y-direction (figure 7.12) indicates bending at the free end of the Si NW. The extent of this bending is reduced with increasing AR due to the increase of stiffness in y-direction. Similar to the torsional deformation encountered in crystal orientation I, the reason behind such bending with crystal orientation II can be traced back to the surface stress configuration. Surface atoms in (110) plane have one dangling bond in $(\bar{1}10)$ plane (figure 7.3) with an opposite y-index for atoms in group A and B. On the other side, surface atoms in group A and B displace with respect to atoms located one layer into the bulk in opposite directions. Such atomic arrangement on the top surface induces a normal surface stress in y-direction, σ_{yy}, on both FCC group (figure 7.6). This surface stress provides a normal load on $\{110\}$ surfaces in $< 100 >$ direction bending the free end of the Si NW.

Bending deformation has a direct influence on the flexural rigidity of the beam. Although longitudinal relaxation of the Si NW cantilever with crystal orientation I

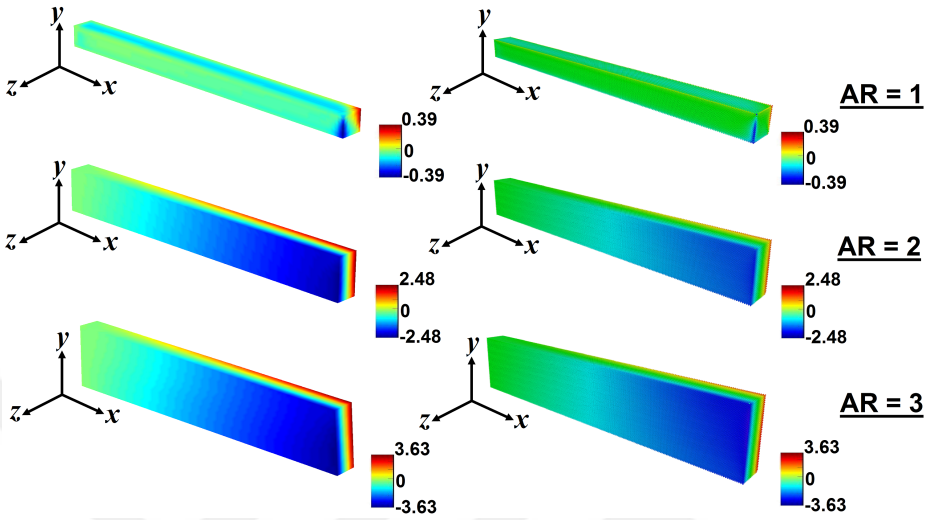


Figure 7.9: y-displacement of Si NWs with crystal orientation I obtained through numerical (left) and atomistic (right) methods (in $\mathring{A}$).

has a negligible effect on the resonance frequency in the flexural mode [Park, 2008], the contribution of bending deformation in the equation of motion of a relaxed Si NW necessitates further investigations. Surface stress in this work is calculated for {110} plane by the virial theorem representing stress components in $< 100 >$ crystal direction (figure 7.6). Bending deformation is predicted for relaxed Si NWs with crystal orientation *II*. The presented approach is utilized to study mechanical behavior of Si NWs in $< 110 >$ crystal direction, for the first time, indicating orientation dependence of surface stress. These observations can be used as a guideline for the interpretation of the surface stress effect on mechanical behavior of Si NWs as reported in previous experimental studies [Sadeghian et al., 2009, Li et al., 2003].

Case studies presented in this section provide an atomic-level explanation of the significant influence of the crystal orientation on the mechanical behavior of the Si NW. Twist and bending deformation induced by surface stress have different effects on the Si NW stiffness. These results indicate the effect of crystal direction and geometry on the mechanical behavior. We believe the observations regarding torsional and bending deformations as a direct outcome of the surface stress relaxation provide

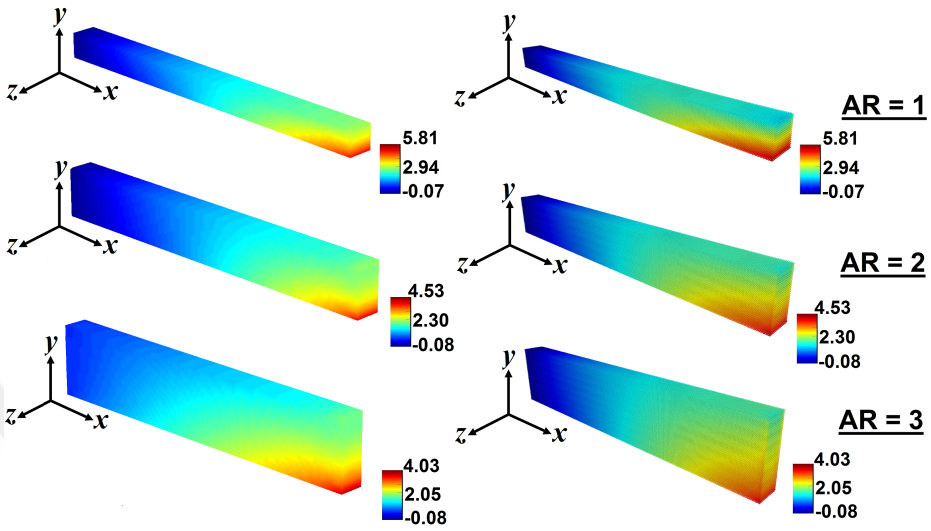


Figure 7.10: x-displacement of Si NWs with crystal orientation *II* obtained through numerical (left) and atomistic (right) methods (in $\mathring{A}$).

an important guideline for future experimental studies, as they represent a means of direct measurement of the surface stress state. Furthermore, surface-stress-related mechanical behavior can also play an important role in the performance of NEMS, an issue of practical concern. In this regard the operation of an electromechanical switch in the form of a Si NW with crystal orientation *I* is simulated in the next section.

7.6.3 Surface Stress Effect on the Operation of an Electromechanical Switch

A frequently utilized NEMS design consists of a suspended Si NW with a nearby electrostatic gate operating in dynamic or static regime [Arkan et al., 2011]. The electrostatic field between the Si NW and the gate has a remarkable effect on the performance of the NEMS [Ekinci and Roukes, 2005]. In addition to previously reported effects of downscaling on the resonant properties [Li et al., 2003] and flexural rigidity [Sadeghian et al., 2009] of NWs, anti-symmetric deformation in a relaxed Si NW — as reported in this work — is also expected to have a significant effect on the operational performance of this NEMS platform. Deformation upon relaxation of the Si NW would cause a deviation — sometimes to a significant degree — from design

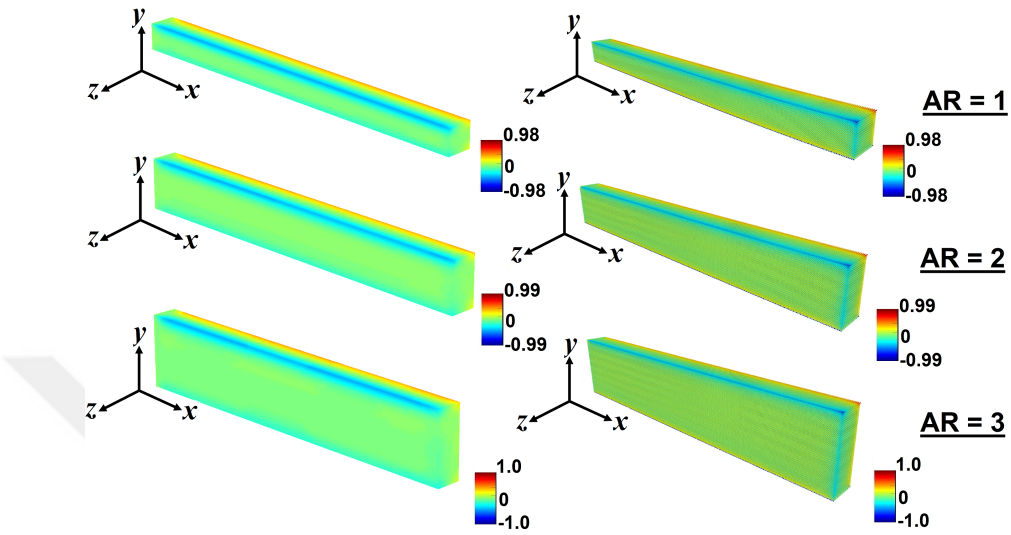


Figure 7.11: z-displacement of Si NWs with crystal orientation *II* obtained through numerical (left) and atomistic (right) methods (in $\mathring{A}$).

parameters. This would in turn induce changes in the electrostatic force. The second reason is modification of the mechanical stiffness by strain energy. The gated Si NW configuration depicted in figure 7.13 can be considered as a parallel plate capacitor with a uniform electrostatic field. The structure consists of a Si NW cantilever and an electrostatic gate. In contrast to the conventional approach, the surface effect can now be incorporated in the formulation as proposed in this work. Here, we assume a uniform electrostatic field in z-direction, where the relation between electrostatic force, f_0, and the gap, g, can be expressed as

$$f_0 \propto \frac{1}{g^2} \tag{7.18}$$

An electrode with a gap, g, of 10 nm is placed parallel to a Si NW with crystal orientation *I*. Surface stress is captured for the Si NW based on the SCB approach. Deformation imposed by the surface stress is utilized in the calculation of the change in g. Electrostatic force for the relaxed Si NW (f_{SCB}) is normalized with the nominal electrostatic force for an undeformed Si NW (f_0). The resulting normalized electrostatic force is shown in figure 7.14. The plots depict the distribution of the electro-

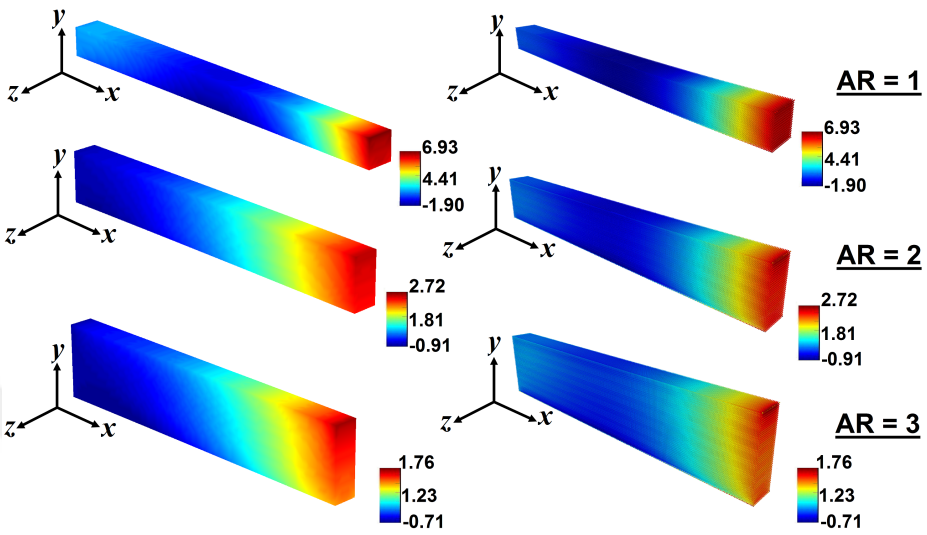


Figure 7.12: y-displacement of Si NWs with crystal orientation *II* obtained through numerical (left) and atomistic (right) methods (in $\mathring{A}$).

static force on the xy surface of the Si NW opposing the electrode. Near the fixed end (left boundary) no relaxation can take place and hence, resulting electrostatic force does not differ from the nominal force. However, results exhibit a gradient in the electrostatic force towards the free end, a direct outcome of the torsional deformation. A deviation as significant as 50% is observed in the case of AR = 3.

Downscaling of Si NWs to sub-50-nm has introduced many applications in mass detection at the molecular scale [Gil-Santos et al., 2010] with fundamental and technological challenges in NEMS optimization [Ekinci and Roukes, 2005]. The significant effect of surface stress on the electrostatic force as presented in this work can be considered as one such fundamental challenge in device design. For instance, operation of NEMS relays is defined based on an interaction between electrostatic and mechanical forces. [Loh and Espinosa, 2012]. A similar principle in dynamic mode is used for Si NW resonators [Ekinci and Roukes, 2005]. Therefore surface stress has a direct influence on the pull-in voltage and frequency response of NEMS relays and resonators, respectively. These effects can be linked to the change in the electrostatic force as well as the mechanical stiffness. Electrostatic field has influence on the mechanical

behavior of the NWs. This effect is traced back to the modification of surface stress in electric field [Park et al., 2011]. Hence, incorporation of electric field into the strain energy calculation can capture surface stress effect in electrostatic field for NEMS applications in further studies.

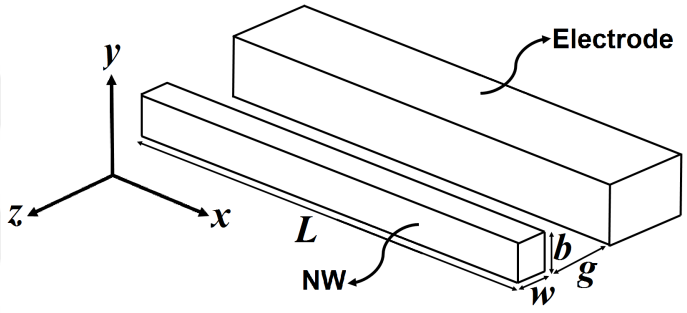


Figure 7.13: Si NW near an electrostatic gate and associated dimensions.

The approach introduced in this work is based on obtaining Si surface stress profile in atomic benchmark and transferring it into the continuum system via SCB for the Si NW configuration. This concept introduces a promising pathway for simulating the electromechanical behavior of Si NWs. Although relaxed surface stress is found to have a negligible effect on the resonance frequency of Si NWs with a square cross-section [Park, 2008], significant deformation in the transverse direction for rectangular cross-sections as presented in this study gives rise to the need for a further investigation. A benchmarking study among the available mechanistic models can introduce a guideline for selecting the optimum tool in resonance frequency calculations [Esfahani et al., 2016b]. Similar high-AR cross-sections are reported for Si NWs integrated with modern electronic devices through the top-down fabrication process [Wollschläger et al., 2016, Esfahani et al., 2017, Yilmaz et al., 2017]. Although the surface stress is calculated here for a defect-free crystal at 0 K, crystal imperfections and thermomechanical behavior at finite temperatures can be taken into account by non-local quasi-continuum [Tadmor et al., 1996b] and thermo-coupled SCB [Esfahani et al., 2016a] approaches, respectively.

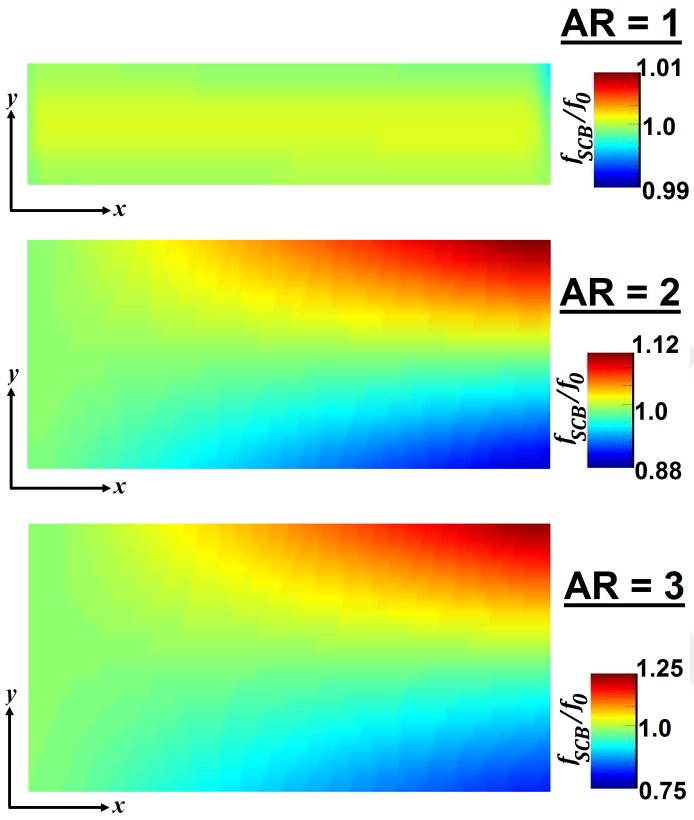


Figure 7.14: Normalized electrostatic force on Si NW *xy* surface with crystal orientation *I*.

7.7 Conclusion

Size and crystal orientation dependence of Si NW surface stress is studied through a new approach based on the transfer of the stress concept from an initial surface analysis at the atomic scale to the continuum framework via multiscale modeling. Surface stress analysis is carried out for {100} and {110} surfaces based on the virial theorem. This surface stress obtained within an atomistic system is then transferred to continuum through the SCB theory. Si NWs with fixed-free boundary conditions are studied, where the free end allows stress relaxation. The associated deformation profile is calculated for Si NWs with their long axes aligned along the crystal orientations of $< 100 >$ and $< 110 >$. The outcome of this chater is summarized below.

Atomistic system on surface:

- Surface atoms on (100) plane are located on the (011) plane, while the corresponding atoms defining the mirror $(\bar{1}00)$ surface are on the $(0\bar{1}1)$ plane. Such perpendicular configuration for surface bonding on mirror $\{100\}$ surfaces imposes shear stresses in opposite directions resembling torsion in a continuum system.

- Atoms on the $\{110\}$ surface in both FCC groups form three bonds as opposed to four in the bulk. Atoms in group A on the free surface displace with respect to the atoms in group B located one layer into the bulk in $< \bar{1}11 >$ direction, while the displacement of atoms in group B on the free surface with respect to the atoms in group A located one layer into the bulk takes place in $< \bar{1}1\bar{1} >$ direction. Such displacement in surface atoms generate a normal stress in $< 100 >$ direction resembling bending in continuum definition.

Continuum system:

- Si NW in $< 100 >$ direction: Shear stresses with opposite sense on mirror 100 surfaces generate torsional load twisting the free end of the $< 100 >$ Si NW. A twist deformation of 5° is observed at the free end in the case of the rectangular cross-section with AR = 3, while such deformation is negligible in the square cross-section.

- Si NW in $< 110 >$ direction: Atomic arrangement on the top surface induces a normal surface stress in $< 100 >$ crystal direction on both FCC groups, A and B. Displacement of atoms on $\{110\}$ surface lead to the bending at the free end.

Finally, to highlight the importance of the deformation induced by surface stresses, a case study is carried out for the operation of an electromechanical switch in the form of a Si NW. A primary calculation on the electrostatic force as a result of the change in Si NW-electrode gap exhibits a 50% variation along the thickness in a relaxed $< 100 >$ Si NW with AR = 3.

The presented approach transfers Si surface stress in atomic benchmark to the continuum platform to analyze surface stress effects on the mechanical behavior of Si NWs. Obtained results and observations provide a promising path for predicting the mechanical behavior of Si NWs for future experimental studies. Furthermore, the observation on Si NWs with $< 110 >$ crystal direction can shed light on the existing controversy between computational [Park, 2008] and experimental [Sadeghian et al., 2009, Li et al., 2003] studies on the reduction of modulus of elastic with reduced size. Finally, electrostatic field [Park et al., 2011], temperature [Esfahani et al., 2016a] and crystal defects [Tadmor et al., 1996b] are further parameters that would change surface stress state, and hence, they need to be addressed in detail.

Chapter 8

REMARKS

The use of Si NWs in modern electronic devices necessitates an engineering pathway based on the simultaneous development of technology and simulation tools. This study addressed both components:

- The experimental study provides a new technology for the integration of Si NWs with new-generation, higher-order architectures, such as MEMS.

- The numerical work introduces a guideline for the incorporation of the scale effect in the modeling of the mechanical behavior of Si NWs with implications in design and implementation for future engineering applications.

In the experimental platform, a new technology for the integration of Si NWs with 3D devices is presented based on IC-compatible processes including high-resolution lithography and etching. This technology is utilized to introduce new-generation PZR sensors by the batch-compatible integration of Si NWs with MEMS within the same SOI device layer, thereby addressing the drawbacks of available techniques. As potential applications of this technique a pilot study exhibiting Si NW electromechanical resonators on thick SOI is demonstrated. Associated technological advantages compared to bottom-up or thin-SOI-based manufacturing are highlighted. Further applications of this technology can be considered for physical sensors such as accelerometers and other inertial measurement devices and pressure sensors, where Si NW serves as a nanoscale mechanical gauge embedded within a microscale component to detect minute displacements.

Although the presented technology is based on top-down semiconductor manufacturing, surface topography related to RIE and process temperatures involved, for example, in LTO coating remain as the major challenges to be tackled for CMOS in-

tegration. The step height involved in oxide encapsulated surface protrusion formed after the shallow etch step is on the order of 800-900 nm. Such surface topography poses significant difficulties for the subsequent high-resolution lithography in CMOS process. Furthermore, LTO coating carried out at 450 °C has to be taken into consideration for the diffusion of metal layers.

In addition to the development of the aforementioned integration technology, a simulation study is carried out with the main motivation of the quantification of the effect of the surface stress on the mechanical behavior of NWs. First, a guideline to select the optimum engineering tool for the frequency response modeling of NW resonators is presented through a benchmarking study among major analytical and numerical approaches. In this respect, computational limits associated with available methods to analyze thermomechanical behavior of NWs with extreme surface-to-volume ratio is addressed by implementing a temperature-dependent interatomic potential into the SCB theory for fcc crystals, called TSCB. Finally, the contrasting experimental and computational reports in the literature on the size dependence of Si NW mechanical behavior is investigated by a comprehensive study on crystal orientation and geometrical parameters on surface stress for the diamond cubic crystal.

TSCB method can similarly be applied to the thermomechanical analysis of Si NWs replacing alternative approaches with a very high computational cost. For this purpose, pair potential in TSCB needs to be modified to many-body potential for the estimation of temperature-dependent strain energy in Si crystal. Definition of internal degree of freedom at finite temperature is the main challenge for transition of TSCB from fcc crystal to diamond crystal structures.

Scale effects for fabricated Si NWs in this study having CD in the order of 100-nm are negligible, while significance of size-dependent behavior in Si NWs is observed for CD less than 30-nm. Therefore the proposed numerical guideline for mechanical modeling cannot be employed for the presented experimental studies. Downscaling integrated Si NWs to sub-30 nm along with the development of TSCB for diamond crystal structure can merge the presented numerical and experimental pathways for

the future use of Si NWs in modern electronic devices.

BIBLIOGRAPHY

[Allain et al., 2012a] Allain, P., Bosseboeuf, A., Parrain, F., Maaroufi, S., Coste, P., and Walther, A. (2012a). Large range mems motion detection using integrated piezo-resistive silicon nanowire. In *Micro Electro Mechanical Systems (MEMS), 2012 IEEE 25th International Conference on*, pages 1320–1323. IEEE.

[Allain et al., 2012b] Allain, P., Le Roux, X., Parrain, F., and Bosseboeuf, A. (2012b). Large initial compressive stress in top-down fabricated silicon nanowires evidenced by static buckling. *Journal of Micromechanics and Microengineering*, 23(1):015014.

[Allain et al., 2013] Allain, P. E., Parrain, F., Bosseboeuf, A., Maaroufi, S., Coste, P., and Walther, A. (2013). Large-range mems motion detection with subangström noise level using an integrated piezoresistive silicon nanowire. *Journal of Microelectromechanical Systems*, 22(3):716–722.

[Appell, 2002] Appell, D. (2002). Nanotechnology: Wired for success. *Nature*, 419(6907):553–555.

[Arellano et al., 2008] Arellano, N., Quevy, E., Provine, J., Maboudian, R., and Howe, R. (2008). Silicon nanowire coupled micro-resonators. In *Micro Electro Mechanical Systems, 2008. MEMS 2008. IEEE 21st International Conference on*, pages 721–724. IEEE.

[Arkan et al., 2011] Arkan, E. F., Sacchetto, D., Yildiz, I., Leblebici, Y., and Alaca, B. E. (2011). Monolithic integration of si nanowires with metallic electrodes: Nems resonator and switch applications. *Journal of Micromechanics and Microengineering*, 21(12):125018.

[Arlett et al., 2011] Arlett, J., Myers, E., and Roukes, M. (2011). Comparative advantages of mechanical biosensors. *Nature nanotechnology*, 6(4):203–215.

[Bandyopadhyay and Sen, 2011] Bandyopadhyay, D. and Sen, J. (2011). Internet of things: Applications and challenges in technology and standardization. *Wireless Personal Communications*, 58(1):49–69.

[Banerjee, 2001] Banerjee, J. (2001). Free vibration analysis of a twisted beam using the dynamic stiffness method. *International Journal of Solids and Structures*, 38(38):6703–6722.

[Barlian et al., 2009] Barlian, A. A., Park, W.-T., Mallon, J. R., Rastegar, A. J., and Pruitt, B. L. (2009). Review: Semiconductor piezoresistance for microsystems. *Proceedings of the IEEE*, 97(3):513–552.

[Bartsch et al., 2011] Bartsch, S., Grogg, D., Lovera, A., Tsamados, D., and Ionescu, A. (2011). Very high frequency double-ended tuning fork nano-mechanical finfet resonator. In *Solid-State Sensors, Actuators and Microsystems Conference (TRANSDUCERS), 2011 16th International*, pages 938–941. IEEE.

[Baski et al., 1997] Baski, A., Erwin, S., and Whitman, L. (1997). The structure of silicon surfaces from (001) to (111). *Surface Science*, 392(1-3):69–85.

[Bathe, 2006] Bathe, K.-J. (2006). *Finite element procedures*. Klaus-Jurgen Bathe.

[Bobba et al., 2012] Bobba, S., De Marchi, M., Leblebici, Y., and De Micheli, G. (2012). Physical synthesis onto a sea-of-tiles with double-gate silicon nanowire transistors. In *Proceedings of the 49th Annual Design Automation Conference*, pages 42–47. ACM.

[Bolten et al., 2011] Bolten, J., Wahlbrink, T., Schmidt, M., Gottlob, H. D., and Kurz, H. (2011). Implementation of electron beam grey scale lithography and

proximity effect correction for silicon nanowire device fabrication. *Microelectronic Engineering*, 88(8):1910–1912.

[Branício and Rino, 2000] Branício, P. S. and Rino, J.-P. (2000). Large deformation and amorphization of ni nanowires under uniaxial strain: a molecular dynamics study. *Physical Review B*, 62(24):16950.

[Cammarata, 1994] Cammarata, R. C. (1994). Surface and interface stress effects in thin films. *Progress in surface science*, 46(1):1–38.

[Cao and Chen, 2008] Cao, G. and Chen, X. (2008). Size dependence and orientation dependence of elastic properties of zno nanofilms. *International journal of solids and structures*, 45(6):1730–1753.

[Carrara et al., 2012] Carrara, S., Sacchetto, D., Doucey, M.-A., Baj-Rossi, C., De Micheli, G., and Leblebici, Y. (2012). Memristive-biosensors: A new detection method by using nanofabricated memristors. *Sensors and Actuators B: Chemical*, 171:449–457.

[Chaste et al., 2012] Chaste, J., Eichler, A., Moser, J., Ceballos, G., Rurali, R., and Bachtold, A. (2012). A nanomechanical mass sensor with yoctogram resolution. *Nature nanotechnology*, 7(5):301–304.

[Chen and Miao, 2007] Chen, B. and Miao, J. (2007). Influence of deep rie tolerances on comb-drive actuator performance. *Journal of Physics D: Applied Physics*, 40(4):970.

[Chen et al., 2006] Chen, C., Shi, Y., Zhang, Y., Zhu, J., and Yan, Y. (2006). Size dependence of youngs modulus in zno nanowires. *Physical review letters*, 96(7):075505.

[Chen et al., 2002] Chen, K.-S., Ayón, A. A., Zhang, X., and Spearing, S. M. (2002). Effect of process parameters on the surface morphology and mechanical perfor-

mance of silicon structures after deep reactive ion etching (drie). *Journal of Microelectromechanical Systems*, 11(3):264–275.

[Chen, 2006] Chen, Y. (2006). Local stress and heat flux in atomistic systems involving three-body forces. *The Journal of chemical physics*, 124(5):054113.

[Chiao and Lin, 2004] Chiao, M. and Lin, L. (2004). Post-packaging frequency tuning of microresonators by pulsed laser deposition. *Journal of Micromechanics and Microengineering*, 14(12):1742.

[Choudhury, 2010] Choudhury, D. (2010). 3d integration technologies for emerging microsystems. In *Microwave Symposium Digest (MTT), 2010 IEEE MTT-S International*, pages 1–4. IEEE.

[Cleland and Roukes, 1996] Cleland, A. and Roukes, M. (1996). Fabrication of high frequency nanometer scale mechanical resonators from bulk si crystals. *Applied Physics Letters*, 69(18):2653–2655.

[Cowper, 1966] Cowper, G. (1966). The shear coefficient in timoshenkos beam theory. *Journal of applied mechanics*, 33(2):335–340.

[Craighead, 2000] Craighead, H. G. (2000). Nanoelectromechanical systems. *Science*, 290(5496):1532–1535.

[Cuenot et al., 2004] Cuenot, S., Frétigny, C., Demoustier-Champagne, S., and Nysten, B. (2004). Surface tension effect on the mechanical properties of nanomaterials measured by atomic force microscopy. *Physical Review B*, 69(16):165410.

[Cui et al., 2000] Cui, Y., Duan, X., Hu, J., and Lieber, C. M. (2000). Doping and electrical transport in silicon nanowires. *The Journal of Physical Chemistry B*, 104(22):5213–5216.

[Cui and Lieber, 2001] Cui, Y. and Lieber, C. M. (2001). Functional nanoscale electronic devices assembled using silicon nanowire building blocks. *science*, 291(5505):851–853.

[Dadgour and Banerjee, 2009] Dadgour, H. F. and Banerjee, K. (2009). Hybrid nems–cmos integrated circuits: a novel strategy for energy-efficient designs. *IET computers & digital techniques*, 3(6):593–608.

[Dao et al., 2010] Dao, D. V., Nakamura, K., Bui, T. T., and Sugiyama, S. (2010). Micro/nano-mechanical sensors and actuators based on soi-mems technology. *Advances in Natural Sciences: Nanoscience and Nanotechnology*, 1(1):013001.

[Davis et al., 2005] Davis, W. R., Wilson, J., Mick, S., Xu, J., Hua, H., Mineo, C., Sule, A. M., Steer, M., and Franzon, P. D. (2005). Demystifying 3d ics: The pros and cons of going vertical. *IEEE Design & Test of Computers*, 22(6):498–510.

[De Marchi et al., 2014] De Marchi, M., Zhang, J., Frache, S., Sacchetto, D., Gaillardon, P.-E., Leblebici, Y., and De Micheli, G. (2014). Configurable logic gates using polarity-controlled silicon nanowire gate-all-around fets. *IEEE Electron Device Letters*, 35(8):880–882.

[Delley and Steigmeier, 1995] Delley, B. and Steigmeier, E. (1995). Size dependence of band gaps in silicon nanostructures. *Applied physics letters*, 67(16):2370–2372.

[Diao et al., 2003] Diao, J., Gall, K., and Dunn, M. L. (2003). Surface-stress-induced phase transformation in metal nanowires. *Nature materials*, 2(10):656–660.

[Duc et al., 2007] Duc, T. C., Creemer, J., and Sarro, P. M. (2007). Piezoresistive cantilever beam for force sensing in two dimensions. *IEEE sensors journal*, 7(1):96–104.

[Dupuy et al., 2005] Dupuy, L. M., Tadmor, E. B., Miller, R. E., and Phillips, R. (2005). Finite-temperature quasicontinuum: Molecular dynamics without all the atoms. *Physical Review Letters*, 95(6):060202.

[Durrani et al., 2013] Durrani, Z., Jones, M., Kaestner, M., Hofer, M., Guliyev, E., Ahmad, A., Ivanov, T., Zoellner, J.-P., and Rangelow, I. W. (2013). Scanning probe lithography approach for beyond cmos devices. In *SPIE Advanced Lithography*, pages 868017–868017. International Society for Optics and Photonics.

[Ekinci and Roukes, 2005] Ekinci, K. and Roukes, M. (2005). Nanoelectromechanical systems. *Review of scientific instruments*, 76(6):061101.

[Eom et al., 2011] Eom, K., Park, H. S., Yoon, D. S., and Kwon, T. (2011). Nanomechanical resonators and their applications in biological/chemical detection: nanomechanics principles. *Physics Reports*, 503(4):115–163.

[Erdem Alaca, 2009] Erdem Alaca, B. (2009). Integration of one-dimensional nanostructures with microsystems: an overview. *International Materials Reviews*, 54(5):245–282.

[Esfahani et al., 2017] Esfahani, M. N., Leblebici, Y., and Alaca, B. E. (2017). A monolithic approach to downscaling silicon piezoresistive sensors. *Journal of Microelectromechanical Systems*.

[Esfahani et al., 2016a] Esfahani, M. N., Sonne, M. R., Hattel, J. H., and Alaca, B. E. (2016a). Thermo-coupled surface cauchy–born theory: An engineering finite element approach to modeling of nanowire thermomechanical response. *Mechanics of Materials*, 94:46–52.

[Esfahani et al., 2016b] Esfahani, M. N., Yilmaz, M., Sonne, M., Hattel, J., and Alaca, B. (2016b). Selecting the optimum engineering model for the frequency response of fcc nanowire resonators. *Applied Mathematical Modelling*.

[Ettelt et al., 2014] Ettelt, D., Rey, P., Jourdan, G., Walther, A., Robert, P., and Delamare, J. (2014). 3d magnetic field sensor concept for use in inertial measurement units (imus). *Journal of Microelectromechanical Systems*, 23(2):324–333.

[Fedder et al., 2008] Fedder, G. K., Howe, R. T., Liu, T.-J. K., and Quevy, E. P. (2008). Technologies for cofabricating mems and electronics. *Proceedings of the IEEE*, 96(2):306–322.

[Feng et al., 2007] Feng, X., He, R., Yang, P., and Roukes, M. (2007). Very high frequency silicon nanowire electromechanical resonators. *Nano Letters*, 7(7):1953–1959.

[Foiles et al., 1986] Foiles, S., Baskes, M., and Daw, M. (1986). Embedded-atom-method functions for the fcc metals cu, ag, au, ni, pd, pt, and their alloys. *Physical Review B*, 33(12):7983.

[Gil-Santos et al., 2010] Gil-Santos, E., Ramos, D., Martínez, J., Fernández-Regúlez, M., García, R., San Paulo, Á., Calleja, M., and Tamayo, J. (2010). Nanomechanical mass sensing and stiffness spectrometry based on two-dimensional vibrations of resonant nanowires. *Nature nanotechnology*, 5(9):641–645.

[Gordon et al., 2009] Gordon, M. J., Baron, T., Dhalluin, F., Gentile, P., and Ferret, P. (2009). Size effects in mechanical deformation and fracture of cantilevered silicon nanowires. *Nano letters*, 9(2):525–529.

[Guianvarc'h et al., 2013] Guianvarc'h, C., Verdot, T., Czarny, J., Redon, E., Ege, K., Guyader, J.-L., Walther, A., and Robert, P. (2013). New planar nano-gauge detection microphone: Analytical and numerical acoustic modeling. In *Proceedings of Meetings on Acoustics*, volume 19, page 030040. Acoustical Society of America.

[Hanay et al., 2012] Hanay, M., Kelber, S., Naik, A., Chi, D., Hentz, S., Bullard, E.,

Colinet, E., Duraffourg, L., and Roukes, M. (2012). Single-protein nanomechanical mass spectrometry in real time. *Nature nanotechnology*, 7(9):602–608.

[He and Lilley, 2008a] He, J. and Lilley, C. M. (2008a). Surface effect on the elastic behavior of static bending nanowires. *Nano Letters*, 8(7):1798–1802.

[He and Lilley, 2008b] He, J. and Lilley, C. M. (2008b). Surface stress effect on bending resonance of nanowires with different boundary conditions. *Applied physics letters*, 93(26):263108.

[He et al., 2008] He, R., Feng, X., Roukes, M., and Yang, P. (2008). Self-transducing silicon nanowire electromechanical systems at room temperature. *Nano Letters*, 8(6):1756–1761.

[He et al., 2005] He, R., Gao, D., Fan, R., Hochbaum, A. I., Carraro, C., Maboudian, R., and Yang, P. (2005). Si nanowire bridges in microtrenches: Integration of growth into device fabrication. *Advanced Materials*, 17(17):2098–2102.

[He and Yang, 2006] He, R. and Yang, P. (2006). Giant piezoresistance effect in silicon nanowires. *Nature nanotechnology*, 1(1):42–46.

[Heyliger and Reddy, 1988] Heyliger, P. and Reddy, J. (1988). A higher order beam finite element for bending and vibration problems. *Journal of sound and vibration*, 126(2):309–326.

[Hochbaum et al., 2008] Hochbaum, A. I., Chen, R., Delgado, R. D., Liang, W., Garnett, E. C., Najarian, M., Majumdar, A., and Yang, P. (2008). Enhanced thermoelectric performance of rough silicon nanowires. *Nature*, 451(7175):163–167.

[Hoffmann et al., 2006] Hoffmann, S., Utke, I., Moser, B., Michler, J., Christiansen, S. H., Schmidt, V., Senz, S., Werner, P., Gösele, U., and Ballif, C. (2006). Measurement of the bending strength of vapor- liquid- solid grown silicon nanowires. *Nano letters*, 6(4):622–625.

[Holmes et al., 2001] Holmes, J. D., Ziegler, K. J., Doty, R. C., Pell, L. E., Johnston, K. P., and Korgel, B. A. (2001). Highly luminescent silicon nanocrystals with discrete optical transitions. *Journal of the American Chemical Society*, 123(16):3743–3748.

[Hughes et al., 1977] Hughes, T. J., Taylor, R. L., and Kanoknukulchai, W. (1977). A simple and efficient finite element for plate bending. *International Journal for Numerical Methods in Engineering*, 11(10):1529–1543.

[Husain et al., 2003] Husain, A., Hone, J., Postma, H. W. C., Huang, X., Drake, T., Barbic, M., Scherer, A., and Roukes, M. (2003). Nanowire-based very-high-frequency electromechanical resonator. *Applied Physics Letters*, 83(6):1240–1242.

[Hutchinson, 2001] Hutchinson, J. (2001). Shear coefficients for timoshenko beam theory. *Journal of Applied Mechanics*, 68(1):87–92.

[Jamaa et al., 2011] Jamaa, M. H. B., Cerofolini, G., De Micheli, G., and Leblebici, Y. (2011). Polysilicon nanowire transistors and arrays fabricated with the multispacer technique. *IEEE Transactions on Nanotechnology*, 10(4):891–899.

[Jiang et al., 2005] Jiang, H., Huang, Y., and Hwang, K. (2005). A finite-temperature continuum theory based on interatomic potentials. *Journal of engineering materials and technology*, 127(4):408–416.

[Jing et al., 2006] Jing, G., Duan, H., Sun, X., Zhang, Z., Xu, J., Li, Y., Wang, J., and Yu, D. (2006). Surface effects on elastic properties of silver nanowires: contact atomic-force microscopy. *Physical Review B*, 73(23):235409.

[Jun et al., 2006] Jun, S. C., Huang, X., Manolidis, M., Zorman, C., Mehregany, M., and Hone, J. (2006). Electrothermal tuning of al–sic nanomechanical resonators. *Nanotechnology*, 17(5):1506.

[Kaestner et al., 2013] Kaestner, M., Hofer, M., and Rangelow, I. W. (2013). Nanolithography by scanning probes on calixarene molecular glass resist using mix-and-match lithography. *Journal of Micro/Nanolithography, MEMS, and MOEMS*, 12(3):031111–031111.

[Kaneko, 1975] Kaneko, T. (1975). On timoshenko's correction for shear in vibrating beams. *Journal of Physics D: Applied Physics*, 8(16):1927.

[Kang and Cai, 2010] Kang, K. and Cai, W. (2010). Size and temperature effects on the fracture mechanisms of silicon nanowires: Molecular dynamics simulations. *International Journal of Plasticity*, 26(9):1387–1401.

[Kang, 2012] Kang, T.-K. (2012). The piezoresistive effect in n-type junctionless silicon nanowire transistors. *Nanotechnology*, 23(47):475203.

[Kant and Gupta, 1988] Kant, T. and Gupta, A. (1988). A finite element model for a higher-order shear-deformable beam theory. *Journal of sound and vibration*, 125(2):193–202.

[Kizuka et al., 2005] Kizuka, T., Takatani, Y., Asaka, K., and Yoshizaki, R. (2005). Measurements of the atomistic mechanics of single crystalline silicon wires of nanometer width. *Physical review B*, 72(3):035333.

[Koumela et al., 2011] Koumela, A., Mercier, D., Dupré, C., Jourdan, G., Marcoux, C., Ollier, E., Purcell, S., and Duraffourg, L. (2011). Piezoresistance of top-down suspended si nanowires. *Nanotechnology*, 22(39):395701.

[Kozinsky et al., 2006] Kozinsky, I., Postma, H. C., Bargatin, I., and Roukes, M. (2006). Tuning nonlinearity, dynamic range, and frequency of nanomechanical resonators. *Applied Physics Letters*, 88(25):253101.

[Lau, 2014] Lau, J. H. (2014). Overview and outlook of three-dimensional integrated circuit packaging, three-dimensional si integration, and three-dimensional integrated circuit integration. *Journal of Electronic Packaging*, 136(4):040801.

[Lee et al., 2008] Lee, K.-N., Jung, S.-W., Shin, K.-S., Kim, W.-H., Lee, M.-H., and Seong, W.-K. (2008). Fabrication of suspended silicon nanowire arrays. *Small*, 4(5):642–648.

[Legtenberg et al., 1996] Legtenberg, R., Groeneveld, A., and Elwenspoek, M. (1996). Comb-drive actuators for large displacements. *Journal of Micromechanics and microengineering*, 6(3):320.

[Li and Lee, 2011] Li, B. and Lee, C. (2011). Nems diaphragm sensors integrated with triple-nano-ring resonator. *Sensors and Actuators A: Physical*, 172(1):61–68.

[Li et al., 2003] Li, X., Ono, T., Wang, Y., and Esashi, M. (2003). Ultrathin single-crystalline-silicon cantilever resonators: fabrication technology and significant specimen size effect on youngs modulus. *Applied Physics Letters*, 83(15):3081–3083.

[Liu et al., 2005] Liu, C. C., Ganusov, I., Burtscher, M., and Tiwari, S. (2005). Bridging the processor-memory performance gap with 3d ic technology. *IEEE Design & Test of Computers*, 22(6):556–564.

[Liu et al., 2009] Liu, X., Katehi, L. P., Chappell, W. J., and Peroulis, D. (2009). A 3.4–6.2 ghz continuously tunable electrostatic mems resonator with quality factor of 460–530. In *Microwave Symposium Digest, 2009. MTT'09. IEEE MTT-S International*, pages 1149–1152. IEEE.

[Liu and Li, 2007] Liu, X. and Li, S. (2007). Nonequilibrium multiscale computational model. *The Journal of chemical physics*, 126(12):124105.

[Loh and Espinosa, 2012] Loh, O. Y. and Espinosa, H. D. (2012). Nanoelectromechanical contact switches. *Nature nanotechnology*, 7(5):283–295.

[Lou et al., 2012] Lou, L., Zhang, S., Park, W.-T., Tsai, J., Kwong, D.-L., and Lee, C. (2012). Optimization of nems pressure sensors with a multilayered diaphragm using silicon nanowires as piezoresistive sensing elements. *Journal of Micromechanics and Microengineering*, 22(5):055012.

[Lu and Lieber, 2007] Lu, W. and Lieber, C. M. (2007). Nanoelectronics from the bottom up. *Nature materials*, 6(11):841–850.

[Ma et al., 2003] Ma, D., Lee, C., Au, F., Tong, S., and Lee, S. (2003). Small-diameter silicon nanowire surfaces. *Science*, 299(5614):1874–1877.

[Marago et al., 2008] Marago, O., Jones, P., Bonaccorso, F., Scardaci, V., Gucciardi, P., Rozhin, A., and Ferrari, A. (2008). Femtonewton force sensing with optically trapped nanotubes. *Nano letters*, 8(10):3211–3216.

[Miller and Shenoy, 2000] Miller, R. E. and Shenoy, V. B. (2000). Size-dependent elastic properties of nanosized structural elements. *Nanotechnology*, 11(3):139.

[Morris et al., 2005] Morris, C. J., Stauth, S. A., and Parviz, B. A. (2005). Self-assembly for microscale and nanoscale packaging: Steps toward self-packaging. *IEEE Transactions on Advanced Packaging*, 28(4):600–611.

[Naik et al., 2009] Naik, A., Hanay, M., Hiebert, W., Feng, X., and Roukes, M. (2009). Towards single-molecule nanomechanical mass spectrometry. *Nature nanotechnology*, 4(7):445–450.

[Najmzadeh et al., 2009] Najmzadeh, M., Bouvet, D., Dobrosz, P., Olsen, S., and Ionescu, A. M. (2009). Investigation of oxidation-induced strain in a top-down si nanowire platform. *Microelectronic Engineering*, 86(7):1961–1964.

[Neuzil et al., 2010] Neuzil, P., Wong, C. C., and Reboud, J. (2010). Electrically controlled giant piezoresistance in silicon nanowires. *Nano letters*, 10(4):1248–1252.

[Nosé, 1984] Nosé, S. (1984). A molecular dynamics method for simulations in the canonical ensemble. *Molecular physics*, 52(2):255–268.

[Oh et al., 2014] Oh, J. Y., Park, J.-T., Jang, H.-J., Cho, W.-J., and Islam, M. S. (2014). 3d-transistor array based on horizontally suspended silicon nano-bridges grown via a bottom-up technique. *Advanced Materials*, 26(12):1929–1934.

[Olsson and Park, 2012] Olsson, P. A. and Park, H. S. (2012). On the importance of surface elastic contributions to the flexural rigidity of nanowires. *Journal of the Mechanics and Physics of Solids*, 60(12):2064–2083.

[Olsson et al., 2010] Olsson, P. A., Park, H. S., and Lidström, P. C. (2010). The influence of shearing and rotary inertia on the resonant properties of gold nanowires. *Journal of applied physics*, 108(10):104312.

[Overton Jr and Gaffney, 1955] Overton Jr, W. and Gaffney, J. (1955). Temperature variation of the elastic constants of cubic elements. i. copper. *Physical Review*, 98(4):969.

[Park, 2008] Park, H. S. (2008). Surface stress effects on the resonant properties of silicon nanowires. *Journal of Applied Physics*, 103(12):123504.

[Park et al., 2011] Park, H. S., Devel, M., and Wang, Z. (2011). A new multiscale formulation for the electromechanical behavior of nanomaterials. *Computer methods in applied mechanics and Engineering*, 200(29):2447–2457.

[Park et al., 2005] Park, H. S., Gall, K., and Zimmerman, J. A. (2005). Shape memory and pseudoelasticity in metal nanowires. *Physical Review Letters*, 95(25):255504.

[Park and Klein, 2007] Park, H. S. and Klein, P. A. (2007). Surface cauchy-born analysis of surface stress effects on metallic nanowires. *Physical Review B*, 75(8):085408.

[Park and Klein, 2008a] Park, H. S. and Klein, P. A. (2008a). A surface cauchy-born model for silicon nanostructures. *Computer methods in applied mechanics and engineering*, 197(41):3249–3260.

[Park and Klein, 2008b] Park, H. S. and Klein, P. A. (2008b). Surface stress effects on the resonant properties of metal nanowires: the importance of finite deformation kinematics and the impact of the residual surface stress. *Journal of the Mechanics and Physics of Solids*, 56(11):3144–3166.

[Park et al., 2006] Park, H. S., Klein, P. A., and Wagner, G. J. (2006). A surface cauchy-born model for nanoscale materials. *International Journal for Numerical Methods in Engineering*, 68(10):1072–1095.

[Patolsky and Lieber, 2005] Patolsky, F. and Lieber, C. M. (2005). Nanowire nanosensors. *Materials today*, 8(4):20–28.

[Plimpton, 1995] Plimpton, S. (1995). Fast parallel algorithms for short-range molecular dynamics. *Journal of computational physics*, 117(1):1–19.

[Ponomareva et al., 2006] Ponomareva, I., Menon, M., Richter, E., and Andriotis, A. N. (2006). Structural stability, electronic properties, and quantum conductivity of small-diameter silicon nanowires. *Physical Review B*, 74(12):125311.

[Priolo et al., 2014] Priolo, F., Gregorkiewicz, T., Galli, M., and Krauss, T. F. (2014). Silicon nanostructures for photonics and photovoltaics. *Nature nanotechnology*, 9(1):19–32.

[Rangelow and Hudek, 1995] Rangelow, I. and Hudek, P. (1995). Mems fabrication by lithography and reactive ion etching (lirie). *Microelectronic engineering*, 27(1-4):471–474.

[Rangelow, 2001] Rangelow, I. W. (2001). Dry etching-based silicon micro-machining for mems. *Vacuum*, 62(2):279–291.

[Rangelow, 2003] Rangelow, I. W. (2003). Critical tasks in high aspect ratio silicon dry etching for microelectromechanical systems. *Journal of Vacuum Science & Technology A: Vacuum, Surfaces, and Films*, 21(4):1550–1562.

[Read et al., 1992] Read, A., Needs, R., Nash, K., Canham, L., Calcott, P., and Qteish, A. (1992). First-principles calculations of the electronic properties of silicon quantum wires. *Physical review letters*, 69(8):1232.

[Reddy et al., 1997] Reddy, J., Wang, C., and Lee, K. (1997). Relationships between bending solutions of classical and shear deformation beam theories. *International Journal of Solids and Structures*, 34(26):3373–3384.

[Renard, 2000] Renard, S. (2000). Industrial mems on soi. *Journal of Micromechanics and Microengineering*, 10(2):245.

[Robert et al., 2009] Robert, P., Nguyen, V., Hentz, S., Duraffourg, L., Jourdan, G., Arcamone, J., and Harrisson, S. (2009). M&nems: A new approach for ultra-low cost 3d inertial sensor. In *Sensors, 2009 IEEE*, pages 963–966. IEEE.

[Roukes, 2001] Roukes, M. (2001). Nanoelectromechanical systems face the future. *Phys. World*, 14(2):25–31.

[Rudd and Lee, 2008] Rudd, R. E. and Lee, B. (2008). Mechanics of silicon nanowires: size-dependent elasticity from first principles. *Molecular Simulation*, 34(1):1–8.

[Sacchetto et al., 2009] Sacchetto, D., Ben-Jamaa, M. H., De Micheli, G., and Leblebici, Y. (2009). Fabrication and characterization of vertically stacked gate-all-around si nanowire fet arrays. In *Solid State Device Research Conference, 2009. ESSDERC'09. Proceedings of the European*, pages 245–248. IEEE.

[Sacchetto et al., 2011] Sacchetto, D., De Micheli, G., and Leblebici, Y. (2011). Ambipolar si nanowire field effect transistors for low current and temperature sens-

ing. In *Solid-State Sensors, Actuators and Microsystems Conference (TRANSDUCERS), 2011 16th International*, pages 2562–2565. IEEE.

[Sacchetto et al., 2012] Sacchetto, D., De Micheli, G., and Leblebici, Y. (2012). Multiterminal memristive nanowire devices for logic and memory applications: A review. *Proceedings of the IEEE*, 100(6):2008–2020.

[Sadeghian et al., 2009] Sadeghian, H., Yang, C., Goosen, J., Van Der Drift, E., Bossche, A., French, P., and Van Keulen, F. (2009). Characterizing size-dependent effective elastic modulus of silicon nanocantilevers using electrostatic pull-in instability. *Applied Physics Letters*, 94(22):221903.

[Sadek et al., 2010] Sadek, A. S., Karabalin, R. B., Du, J., Roukes, M. L., Koch, C., and Masmanidis, S. C. (2010). Wiring nanoscale biosensors with piezoelectric nanomechanical resonators. *Nano letters*, 10(5):1769–1773.

[Sage et al., 2015] Sage, E., Brenac, A., Alava, T., Morel, R., Dupré, C., Hanay, M. S., Roukes, M. L., Duraffourg, L., Masselon, C., and Hentz, S. (2015). Neutral particle mass spectrometry with nanomechanical systems. *Nature communications*, 6.

[Sander and Ibach, 1991] Sander, D. and Ibach, H. (1991). Experimental determination of adsorbate-induced surface stress: Oxygen on si (111) and si (100). *Physical Review B*, 43(5):4263.

[Sansa et al., 2014] Sansa, M., Fernández-Regúlez, M., Llobet, J., San Paulo, Á., and Pérez-Murano, F. (2014). High-sensitivity linear piezoresistive transduction for nanomechanical beam resonators. *Nature communications*, 5.

[Sansa et al., 2012] Sansa, M., Fernández-Regúlez, M., San Paulo, Á., and Pérez-Murano, F. (2012). Electrical transduction in nanomechanical resonators based

on doubly clamped bottom-up silicon nanowires. *Applied Physics Letters*, 101(24):243115.

[Sanz-Navarro et al., 2004] Sanz-Navarro, C., Kenny, S., and Smith, R. (2004). Atomistic simulations of structural transformations of silicon surfaces under nanoindentation. *Nanotechnology*, 15(5):692.

[Schlier and Farnsworth, 1959] Schlier, R. and Farnsworth, H. (1959). Structure and adsorption characteristics of clean surfaces of germanium and silicon. *The Journal of Chemical Physics*, 30(4):917–926.

[Shaw et al., 1993] Shaw, K. A., Zhang, Z. L., and MacDonald, N. C. (1993). Scream i: A single mask, single-crystal silicon process for microelectromechanical structures. In *Micro Electro Mechanical Systems, 1993, MEMS'93, Proceedings An Investigation of Micro Structures, Sensors, Actuators, Machines and Systems. IEEE.*, pages 155–160. IEEE.

[Shaw et al., 1994] Shaw, K. A., Zhang, Z. L., and MacDonald, N. C. (1994). Scream i: a single mask, single-crystal silicon, reactive ion etching process for microelectromechanical structures. *Sensors and Actuators A: Physical*, 40(1):63–70.

[Shenoy, 2005] Shenoy, V. B. (2005). Atomistic calculations of elastic properties of metallic fcc crystal surfaces. *Physical Review B*, 71(9):094104.

[Singh, 2015] Singh, R. (2015). Eds semiconductor manufacturing committee report. *IEEE ELECTRON DEVICES SOCIETY NEWSLETTER*, (22-4):13–14.

[Sohn et al., 2010] Sohn, Y.-S., Park, J., Yoon, G., Song, J., Jee, S.-W., Lee, J.-H., Na, S., Kwon, T., and Eom, K. (2010). Mechanical properties of silicon nanowires. *Nanoscale research letters*, 5(1):211.

[Song et al., 2011] Song, F., Huang, G., Park, H., and Liu, X. (2011). A continuum model for the mechanical behavior of nanowires including surface and

surface-induced initial stresses. *International Journal of Solids and Structures*, 48(14):2154–2163.

[Soon et al., 2010] Soon, B. W., Neuzil, P., Wong, C. C., Reboud, J., Feng, H. H., and Lee, C. (2010). Ultrasensitive nanowire pressure sensor makes its debut. *Procedia Engineering*, 5:1127–1130.

[Stern et al., 2007] Stern, E., Klemic, J. F., Routenberg, D. A., Wyrembak, P. N., Turner-Evans, D. B., Hamilton, A. D., LaVan, D. A., Fahmy, T. M., and Reed, M. A. (2007). Label-free immunodetection with cmos-compatible semiconducting nanowires. *Nature*, 445(7127):519–522.

[Subramaniyan and Sun, 2008] Subramaniyan, A. K. and Sun, C. (2008). Engineering molecular mechanics: an efficient static high temperature molecular simulation technique. *Nanotechnology*, 19(28):285706.

[Subramaniyan and Sun, 2010] Subramaniyan, A. K. and Sun, C. (2010). Temperature dependent effective embedded atom method potential for steady state high temperature applications. *Journal of Computational and Theoretical Nanoscience*, 7(1):176–181.

[Tabib-Azar et al., 2005] Tabib-Azar, M., Nassirou, M., Wang, R., Sharma, S., Kamins, T., Islam, M. S., and Williams, R. S. (2005). Mechanical properties of self-welded silicon nanobridges. *Applied Physics Letters*, 87(11):113102.

[Tadmor et al., 1996a] Tadmor, E., Phillips, R., and Ortiz, M. (1996a). Mixed atomistic and continuum models of deformation in solids. *Langmuir*, 12(19):4529–4534.

[Tadmor et al., 1996b] Tadmor, E. B., Ortiz, M., and Phillips, R. (1996b). Quasicontinuum analysis of defects in solids. *Philosophical magazine A*, 73(6):1529–1563.

[Tang et al., 2006] Tang, Z., Zhao, H., Li, G., and Aluru, N. (2006). Finite-temperature quasicontinuum method for multiscale analysis of silicon nanostructures. *Physical Review B*, 74(6):064110.

[Tasdemir et al., 2015] Tasdemir, Z., Peric, O., Sacchetto, D., Fantner, G. E., Leblebici, Y., and Alaca, B. E. (2015). Monolithic fabrication of silicon nanowires bridging thick silicon structures. *Nanotechnology Express, IEEE*, 1:2–5.

[Tasdemir et al., 2016] Tasdemir, Z., Wollschläger, N., Österle, W., Leblebici, Y., and Alaca, B. E. (2016). A deep etching mechanism for trench-bridging silicon nanowires. *Nanotechnology*, 27(9):095303.

[Tersoff, 1989] Tersoff, J. (1989). Modeling solid-state chemistry: Interatomic potentials for multicomponent systems. *Physical Review B*, 39(8):5566.

[Thompson and Parthasarathy, 2006] Thompson, S. E. and Parthasarathy, S. (2006). Moore's law: the future of si microelectronics. *Materials today*, 9(6):20–25.

[Truitt et al., 2007] Truitt, P. A., Hertzberg, J. B., Huang, C., Ekinci, K. L., and Schwab, K. C. (2007). Efficient and sensitive capacitive readout of nanomechanical resonator arrays. *Nano letters*, 7(1):120–126.

[Tsuchiya et al., 2016] Tsuchiya, T., Hemmi, T., Suzuki, J.-y., Hirai, Y., and Tabata, O. (2016). Tensile fracture of integrated single-crystal silicon nanowire using mems electrostatic testing device. *Procedia Structural Integrity*, 2:1405–1412.

[Tufte and Stelzer, 1963] Tufte, O. and Stelzer, E. (1963). Piezoresistive properties of silicon diffused layers. *Journal of Applied Physics*, 34(2):313–318.

[Verbridge et al., 2007] Verbridge, S. S., Shapiro, D. F., Craighead, H. G., and Parpia, J. M. (2007). Macroscopic tuning of nanomechanics: substrate bending for reversible control of frequency and quality factor of nanostring resonators. *Nano Letters*, 7(6):1728–1735.

[Vyvoda et al., 1998] Vyvoda, M., Lee, H., Malyshev, M., Klemens, F., Cerullo, M., Donnelly, V., Graves, D., Kornblit, A., and Lee, J. (1998). Effects of plasma conditions on the shapes of features etched in cl2 and hbr plasmas. i. bulk crystalline silicon etching. *Journal of Vacuum Science & Technology A*, 16(6):3247–3258.

[Waldrop, 2016] Waldrop, M. (2016). More than moore. *Nature*, 530(7589):114.

[Walther et al., 2012] Walther, A., Savoye, M., Jourdan, G., Renaux, P., Souchon, F., Robert, P., Le Blanc, C., Delorme, N., Gigan, O., and Lejuste, C. (2012). 3-axis gyroscope with si nanogage piezo-resistive detection. In *Micro Electro Mechanical Systems (MEMS), 2012 IEEE 25th International Conference on*, pages 480–483. IEEE.

[Wang et al., 2006] Wang, C., Tan, V., and Zhang, Y. (2006). Timoshenko beam model for vibration analysis of multi-walled carbon nanotubes. *Journal of Sound and Vibration*, 294(4):1060–1072.

[Wang and Li, 2007] Wang, G. and Li, X. (2007).). size dependency of the elastic modulus of zno nanowires: Surface stress effect. *Applied Physics Letters*, 91(23):231912.

[Wang and Feng, 2007] Wang, G.-F. and Feng, X.-Q. (2007). Effects of surface elasticity and residual surface tension on the natural frequency of microbeams. *Applied physics letters*, 90(23):231904.

[Wang and Feng, 2009] Wang, G.-F. and Feng, X.-Q. (2009). Surface effects on buckling of nanowires under uniaxial compression. *Applied physics letters*, 94(14):141913.

[Wang et al., 2008] Wang, J.-S., Feng, X.-Q., Wang, G.-F., and Yu, S.-W. (2008). Twisting of nanowires induced by anisotropic surface stresses. *Applied Physics Letters*, 92(19):191901.

[Wang and Herron, 1991] Wang, Y. and Herron, N. (1991). Nanometer-sized semiconductor clusters: materials synthesis, quantum size effects, and photophysical properties. *The Journal of Physical Chemistry*, 95(2):525–532.

[Wang et al., 2013] Wang, Y., Wang, T., Da, P., Xu, M., Wu, H., and Zheng, G. (2013). Silicon nanowires for biosensing, energy storage, and conversion. *Advanced Materials*, 25(37):5177–5195.

[Weaver Jr et al., 1990] Weaver Jr, W., Timoshenko, S. P., and Young, D. H. (1990). *Vibration problems in engineering*. John Wiley & Sons.

[Wollschläger et al., 2016] Wollschläger, N., Tasdemir, Z., Häusler, I., Leblebici, Y., Österle, W., and Alaca, B. E. (2016). Determination of the elastic behavior of silicon nanowires within a scanning electron microscope. *Journal of Nanomaterials*, 2016:36.

[Wu et al., 2006] Wu, C.-H., Zorman, C. A., and Mehregany, M. (2006). Fabrication and testing of bulk micromachined silicon carbide piezoresistive pressure sensors for high temperature applications. *IEEE sensors Journal*, 6(2):316–324.

[Xiao and Yang, 2006] Xiao, S. and Yang, W. (2006). Temperature-related cauchy–born rule for multiscale modeling of crystalline solids. *Computational Materials Science*, 37(3):374–379.

[Xu and Zhu, 2012] Xu, F. and Zhu, Y. (2012). Highly conductive and stretchable silver nanowire conductors. *Advanced Materials*, 24(37):5117–5122.

[Yan et al., 2009] Yan, R., Gargas, D., and Yang, P. (2009). Nanowire photonics. *Nature Photonics*, 3(10):569–576.

[Yang et al., 2006] Yang, Y., Callegari, C., Feng, X., Ekinci, K., and Roukes, M. (2006). Zeptogram-scale nanomechanical mass sensing. *Nano letters*, 6(4):583–586.

[Yao and Zhu, 2015] Yao, S. and Zhu, Y. (2015). Nanomaterial-enabled stretchable conductors: Strategies, materials and devices. *Advanced Materials*, 27(9):1480–1511.

[Yilmaz et al., 2017] Yilmaz, M., Kilinc, Y., Nadar, G., Tasdemir, Z., Wollschläger, N., Österle, W., Leblebici, Y., and Alaca, B. E. (2017). Top-down technique for scaling to nano in silicon mems. *Journal of Vacuum Science & Technology B, Nanotechnology and Microelectronics: Materials, Processing, Measurement, and Phenomena*, 35(2):022001.

[Yun and Park, 2008] Yun, G. and Park, H. S. (2008). A multiscale, finite deformation formulation for surface stress effects on the coupled thermomechanical behavior of nanomaterials. *Computer Methods in Applied Mechanics and Engineering*, 197(41):3337–3350.

[Yun and Park, 2009] Yun, G. and Park, H. S. (2009). Surface stress effects on the bending properties of fcc metal nanowires. *Physical Review B*, 79(19):195421.

[Zhang et al., 2016a] Zhang, A., Zheng, G., and Lieber, C. (2016a). *Nanowires: Building Blocks for Nanoscience and Nanotechnology*. Springer.

[Zhang et al., 2016b] Zhang, H., Tersoff, J., Xu, S., Chen, H., Zhang, Q., Zhang, K., Yang, Y., Lee, C.-S., Tu, K.-N., Li, J., et al. (2016b). Approaching the ideal elastic strain limit in silicon nanowires. *Science Advances*, 2(8):e1501382.

[Zhang et al., 2012] Zhang, S., Lou, L., and Lee, C. (2012). Piezoresistive silicon nanowire based nanoelectromechanical system cantilever air flow sensor. *Applied Physics Letters*, 100(2):023111.

[Zhang et al., 2011] Zhang, Y., Liu, X., Ru, C., Zhang, Y. L., Dong, L., and Sun, Y. (2011). Piezoresistivity characterization of synthetic silicon nanowires using a mems device. *Journal of Microelectromechanical Systems*, 20(4):959–967.

[Zhao and Yakobson, 2003] Zhao, Y. and Yakobson, B. I. (2003). What is the ground-state structure of the thinnest si nanowires? *Physical review letters*, 91(3):035501.

[Zhu et al., 2009] Zhu, Y., Xu, F., Qin, Q., Fung, W. Y., and Lu, W. (2009). Mechanical properties of vapor- liquid- solid synthesized silicon nanowires. *Nano letters*, 9(11):3934–3939.

[Zimmerman et al., 2004] Zimmerman, J. A., WebbIII, E. B., Hoyt, J., Jones, R. E., Klein, P., and Bammann, D. J. (2004). Calculation of stress in atomistic simulation. *Modelling and simulation in materials science and engineering*, 12(4):S319.

APPENDIX

Description

This work aims to fabricate a single suspended Si nanowire over deep etch trench by using top-down micro/nano fabrication techniques. Nanowire is attached to a MEMS comb drive actuator shuttle. Both nanowire and actuator shuttle are released.

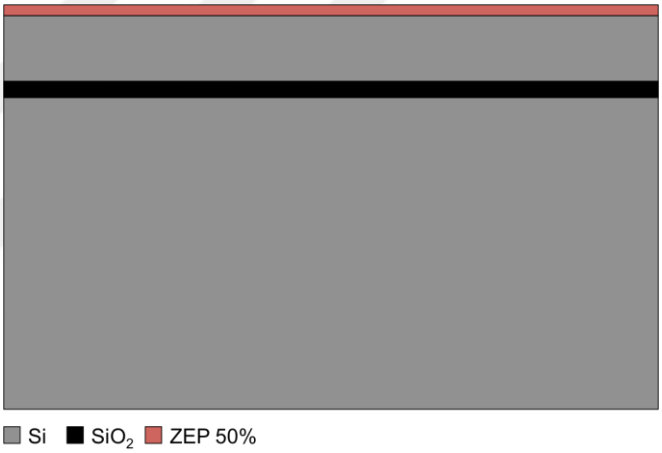
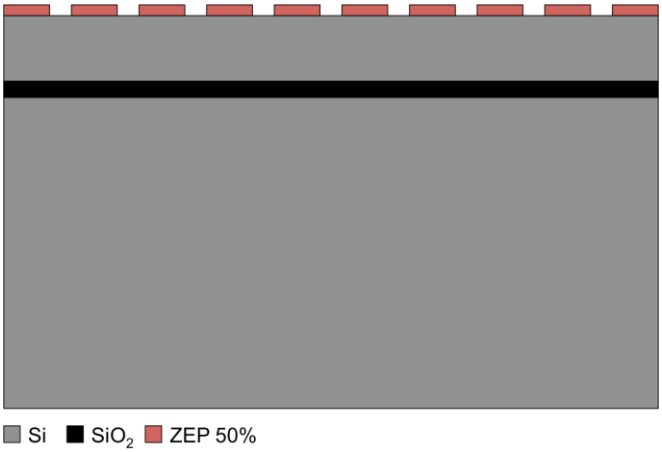
Technologies

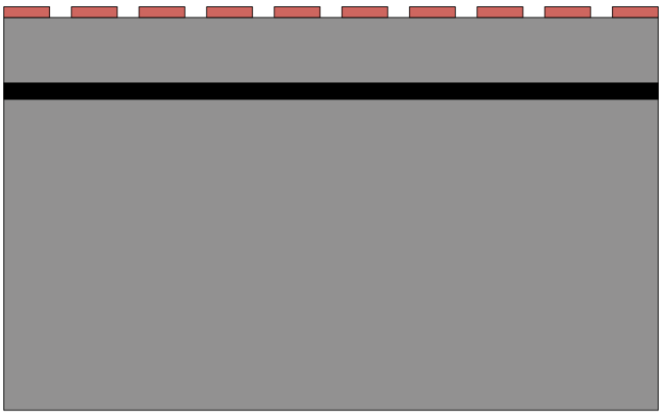
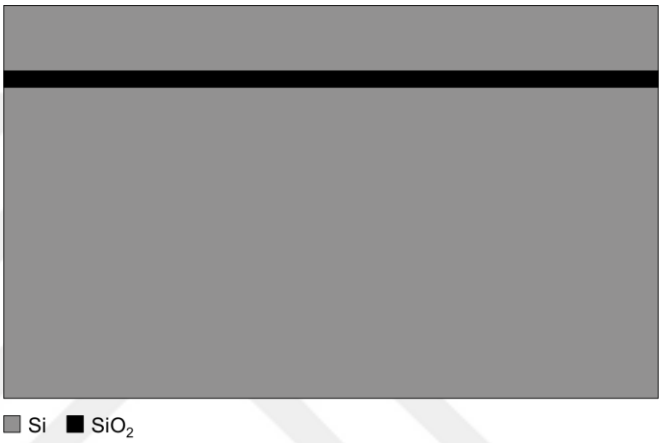
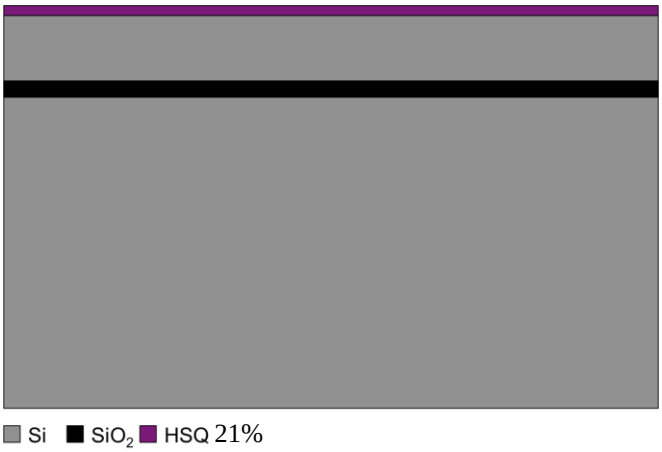
- e-beam Lithography
- Silicon Thin Film Etching
- Evaporative Metal Coating (Lift-off Purposes)
- LPCVD LTO Coating
- Directional Silicon Oxide Etching
- DRIE
- HF Vapour Release

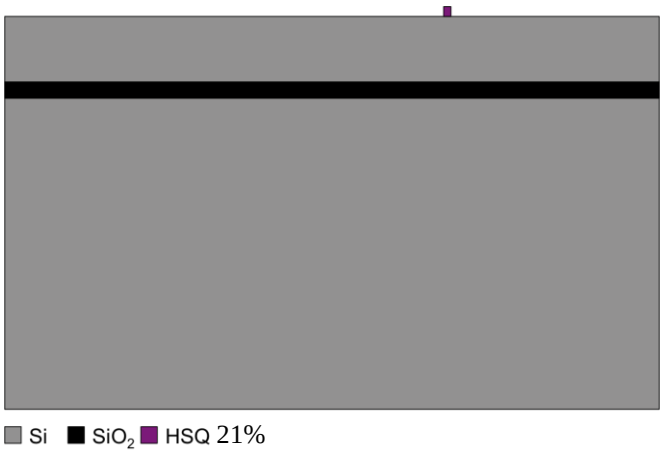
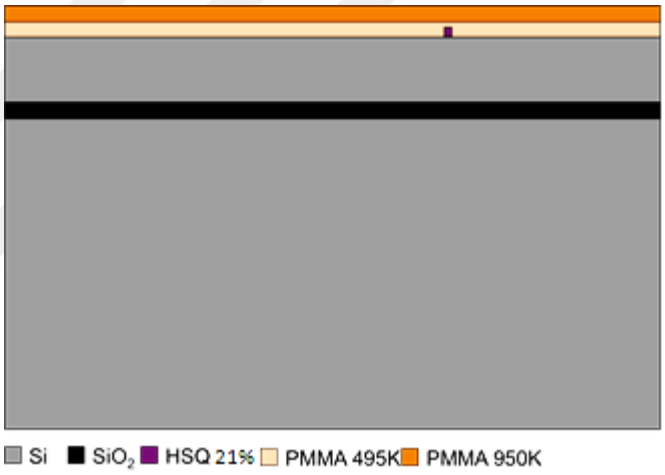
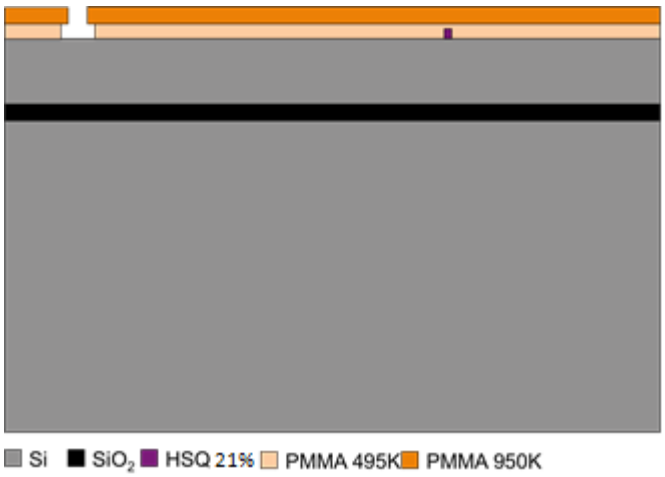
Substrate Type

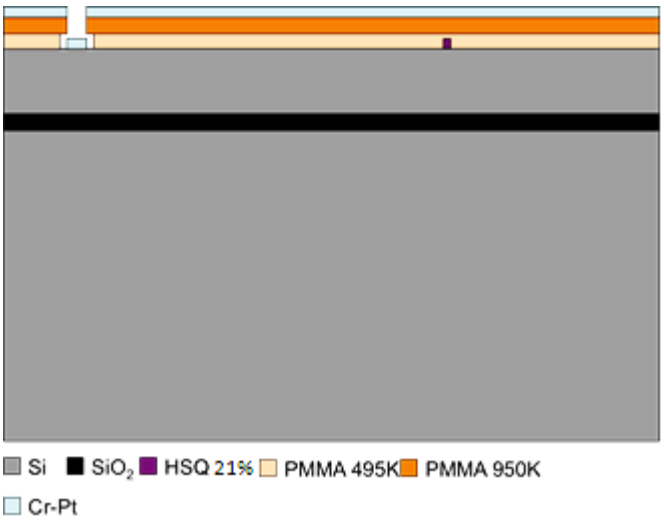
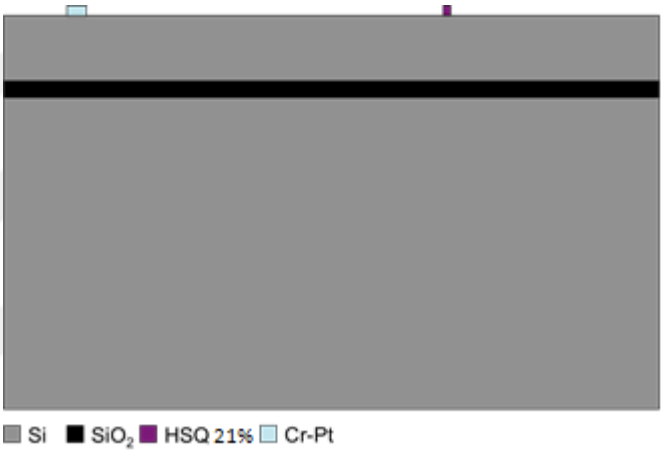
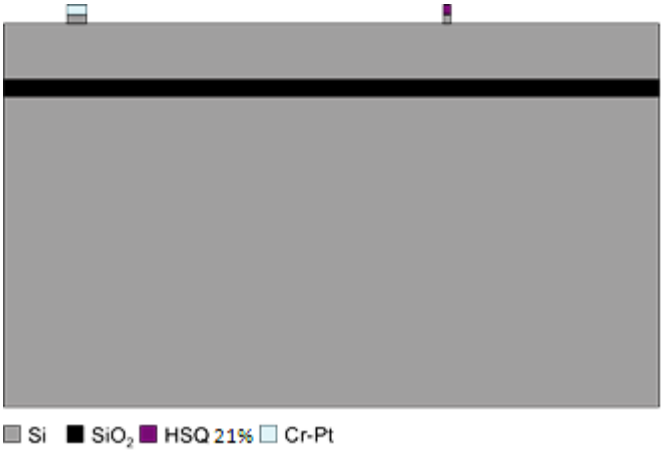
- Silicon $< 100 >$, ϕ100 mm, Test Wafer, 525 μm thick, p-type, 0.1-100 $\Omega.cm$ (CMI Test Wafer)
- SOI Prime Silicon Wafer $< 100 >$, p-type, ϕ100 mm Device Thickness: 10 ± 1 μm, Handle Thickness: 345 ± 1 μm, BOX Thickness: $1 \pm 5\%$ μm Device Resistance: 1-10 $\Omega.cm$
- SOI Prime Silicon Wafer $< 100 >$,n-type, ϕ100 mm Device Thickness: 10 ± 1 μm, Handle Thickness: 500 ± 1 μm, BOX Thickness: $2 \pm 5\%$ μm Device Resistance: 1-10 $\Omega.cm$

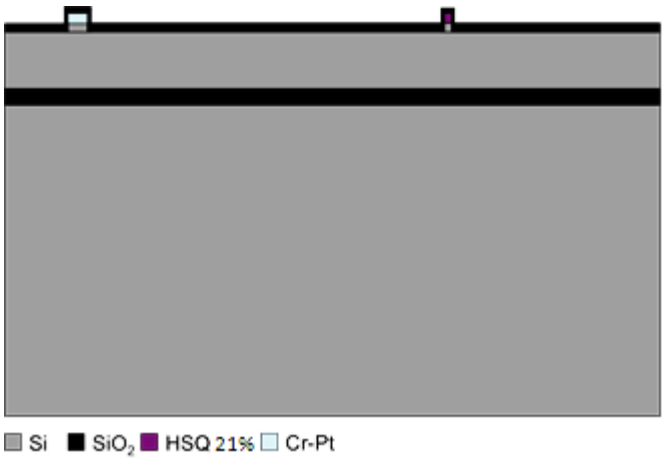
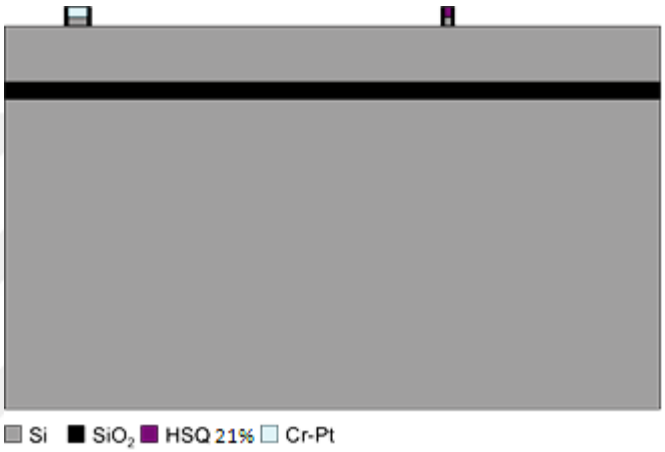
* Device layer resistance for SOI wafers will be doped to less than 0.01 $\Omega.cm$ prior to further processing.

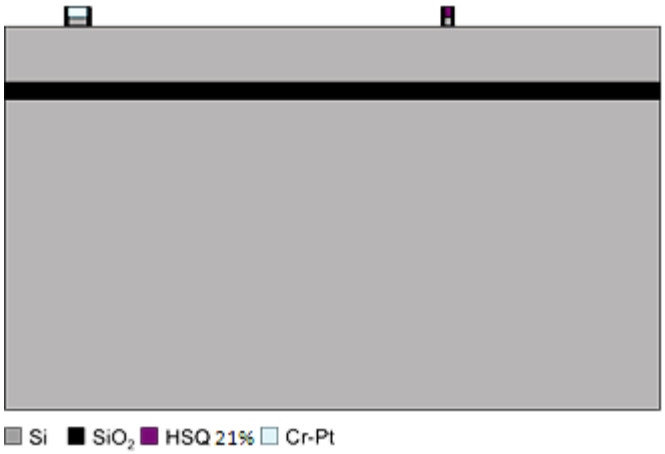
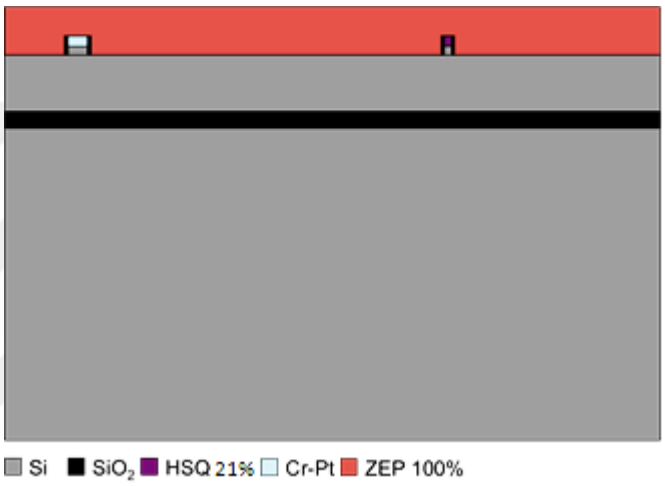
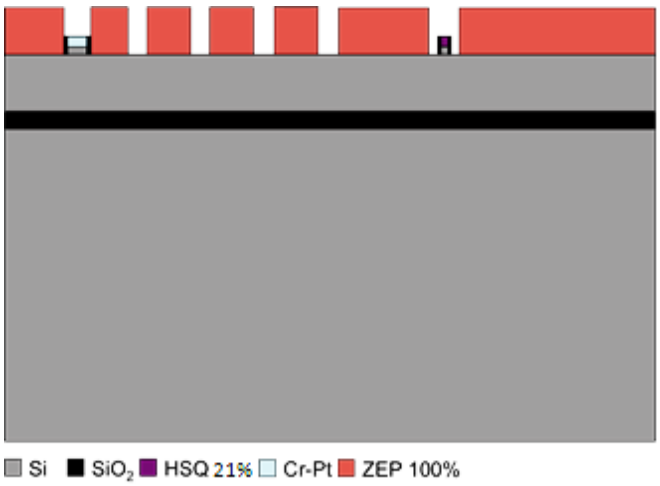
Step	Process description	Cross-section after process
0.0.	***Starting Wafer*** • Process is developed for SOI wafer configurations	 (On SOI wafers Device Layer Resistivity should be around 0.01 Ohm.cm)
0.1.	***Surface Activation – ZEP 50% Coating*** • 5 minutes 600W Oxygen Plasma • 2000 rpm ZEP 50% spin coating • 5 minutes 180 °C stabilization bake	
0.2.	***E-beam Patterning – ZEP 50% Development*** • 100 nm fracture grid size • 150 nA beam current • 225 $\mu C/cm^2$ dose • 1 minutes 45 seconds development with Amyl-Acetate • 40 seconds rinsing with 90:10 MiBK:IPA Solution	

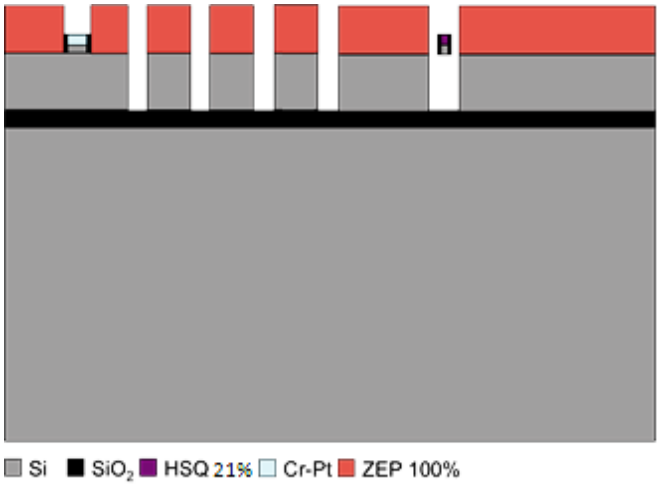
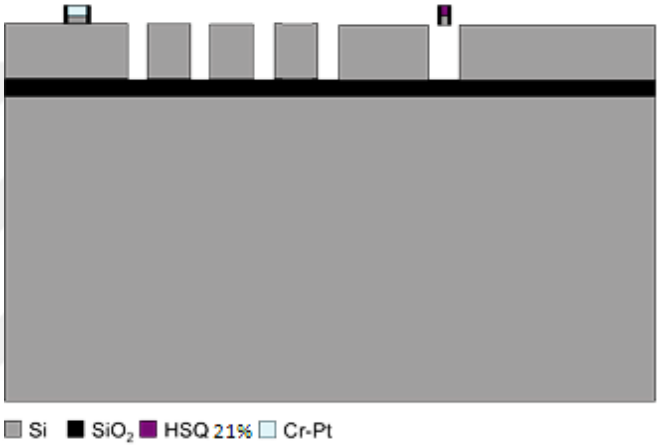
0.3.	***Alignment Pattern Etching **** • 2 µm etch • Recipe: SOI_Acc + • Selectivity: 75 : 1 (PR) 150:1 (SiO_2) • Etch Rate: 3–4.5 µm/min (depends on design) • Time: 30 seconds	 ** Pattern etching is not showed in the schematics because it is a preparation step*
0.4.	***ZEP 50% Removal*** • 600 W Oxygen Plasma for 5 minutes	
1.1.	***Surface Activation – HSQ 21% Coating*** • 5 minutes 600W Oxygen Plasma • ~600 nm HSQ thickness • Due to the HSQ stabilization problems patterning must be completed right after coating	

1.2.	***E-beam Patterning – HSQ 21% Development*** Nanowire stack patterning • 5000 μC/cm^2 • 5 nm fracture grid size • 5 nA beam current • 2 minutes TMAH 25% development • Overflow bath water rinsing until the resistivity back to normal	
2.1.	***Surface Activation – PMMA 495K/ PMMA 950K Coating*** • 5 minutes 600W Oxygen Plasma • Bottom layer: PMMA 495K A8 • Top layer: PMMA 950K A4 • PMMA 495K Thickness: 400 nm • 5 minutes 180 °C stabilization bake • 6000 rpm PMMA 495K Spin Coating • PMMA 950K Thickness: 160 nm • 6000 rpm PMMA 950K Spin Coating • 5 minutes 180 °C stabilization bake	
2.2.	***E-beam Patterning – PMMA / PMMA Development*** Metal Stack Patterning • 50 nm fracture grid size • 150 nA beam current • 1200 μC/cm^2 dose • 1 minute 1:3 MiBK:IPA solution development • 1 minute IPA rinsing	

2.3	***Cr – Pt Evaporator Coating*** • Lift-Off purposes • Lab 600H • Recipe No: 251 – HRN • Deposition Rate: 24 nm / min • 5 nm Cr • 50 nm Pt	
2.4.	***Lift-Off*** • 24 hours of Acetone Bath • 10 seconds sonication (If required)	
3.1.	***Si Thin Film Etching*** • STS Multiplex ICP • Process Name: Sub_Si • HSQ Etch Rate: 20 nm / 15 seconds • Etch Rate: 65 nm / 15 seconds • Desired depth: 200 nm • Time of Etch: 45 seconds	

3.2.	***LPCVD LTO Coating*** • Desired Thickness: 80-100 nm LTO	
3.3.	***Directional Oxide Etch*** • SPTS APS Dielectric Etcher • Recipe: SiO_2/PR - 1/1 • Etch Rate : WetOX 230 nm / min (CMI Value) • Time: 50 seconds	
4.1.	***AZ 92xx Coating – Wafer Dicing **** • AZ 92xx 2 μm coating	 ** Dicing Steps is conducted for starting to work on chip scale, so there is no change in the individual chips*

4.2.	***AZ 92xx Removal*** • 5 minutes of Remover 1165 (Shipley) • 10 minutes of overflow bath water rinsing	
5.1.	***Surface Activation – ZEP 100% Coating*** • 5 minutes 180 °C hot plate (no oxygen plasma due to parylene-C) • 2000 rpm ZEP 100% spin coating • 5 minutes 180 °C stabilization bake	
5.2.	***E-beam Patterning – ZEP 100% Development*** • 50 nm fracture grid size • 150 nA beam current • 225 $\mu C/cm^2$ dose • 1 minutes 45 seconds development with Amyl-Acetate • 40 seconds rinsing with 90:10 MiBK:IPA Solution	

5.3.	***DRIE (Bosch Process)*** • 10 µm etch (until BOX Layer) • Recipe: SOI_Acc + • Selectivity: 75 : 1 (PR) 150 : 1 (SiO_2) • Etch Rate: 3–4.5 µm/min (CMI Value) • 13 etch steps (or till BOX layer is reached – etch steps should be applied in different runs)	
5.4.	***ZEP 100% Removal*** • Low power, short duration oxygen plasma	
5.5.	***HF Vapor Release*** • IDONUS HF-VPE • 3 – 4 hours of HF Vapor Releasing	